CHALMERS
UNIVERSITY OF TECHNOLOGY

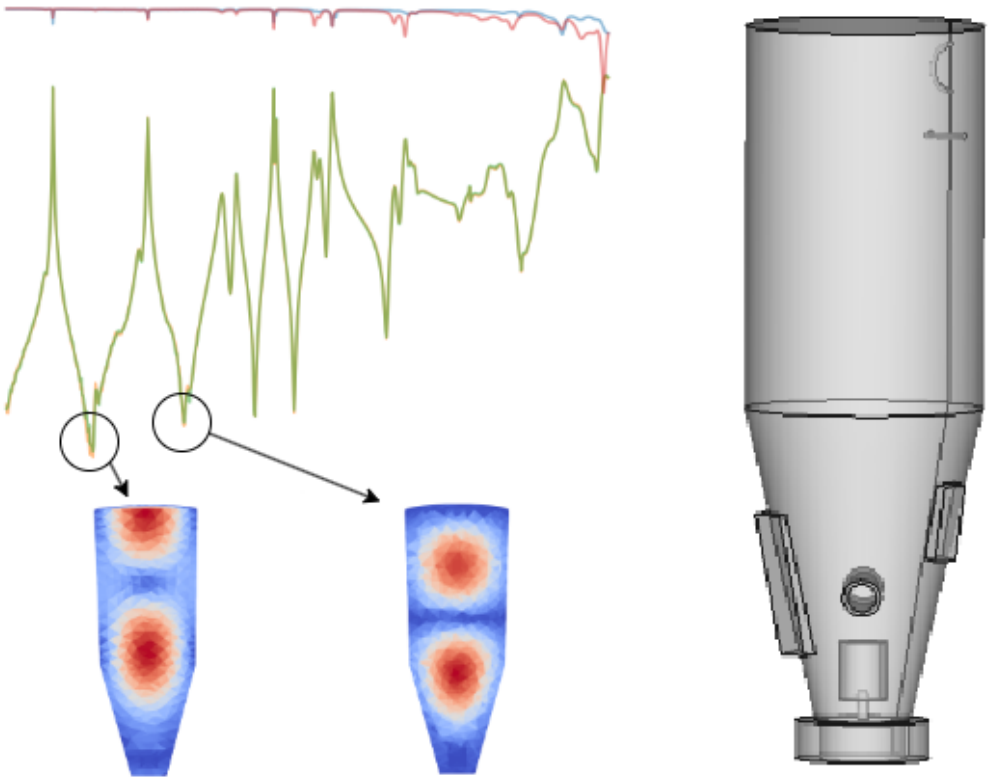

Applications of microwaves in pharmaceutical processes

Development of a monitor for fluid bed- & continuous flow processes, an electroporation protocol, and a device for characterisation of chemical samples.

Master's thesis in Biomedical Engineering

Robin Nilsson

DEPARTMENT OF ELECTRICAL ENGINEERING

CHALMERS UNIVERSITY OF TECHNOLOGY
Gothenburg, Sweden 2024
www.chalmers.se

Master's thesis 2024

Applications of microwaves in pharmaceutical processes

Development of a monitor for fluid bed- & continuous flow processes, an electroporation protocol, and a device for characterisation of chemical samples.

Robin Nilsson

CHALMERS
UNIVERSITY OF TECHNOLOGY

Department of Electrical Engineering
Division of Biomedical Engineering
Chalmers University of Technology
Gothenburg, Sweden 2024

Department of Oral Product Development (OPD)
AstraZeneca, Gothenburg
Gothenburg, Sweden 2024

Applications of microwaves in pharmaceutical processes
Development of a monitor for fluid bed- & continuous flow processes, an electroporation protocol, and a device for characterisation of chemical samples. Robin Nilsson

Supervisors:	Gustaf Hulthe	Astra Zeneca
	Mats Josefson	Astra Zeneca
	Helena Rodilla	Department of Microtechnology and Nanoscience
Examiner:	Hana Dobsicek Trefna	Department of Electrical Engineering

Master's Thesis 2024
Department of Electrical Engineering
Division of Biomedical Engineering
Chalmers University of Technology
SE-412 96 Gothenburg
Telephone +46 31 772 1000

Cover: Microwave monitoring of a fluidised bed.

Typeset in LaTeX
Printed by Chalmers Reproservice
Gothenburg, Sweden 2024

Abstract

Microwaves, electromagnetic waves within the frequency range of 0.3-300 GHz, have been subject to many studies and research within the pharmaceutical industry. The attractiveness of microwaves typically lies in their non-invasive, non-destructive nature while local areas within samples may still be accessed or studied. From processes in early development phases to late processes in production, records of devices exploiting these characteristics of microwaves can be found dating back half a century. Still, research investigating new possibilities utilising microwaves continuously emerges, suggesting the overall usability is still much unexplored. The current thesis aims to investigate in-early-phase research of microwaves that may be useful for various purposes in the pharmaceutical industry but have yet to find wide recognition. The study will not be limited to literature research, but in contrast, will implement aspiring research using available tools and discuss the implementations from a practical viewpoint. Improvements in each case will be provided and to some degree implemented. Specifically, four cases are presented where two cases attempt to develop a monitor for two different industrial processes: continuous flow through a pipe (case I) and batch sample particle coating in a fluid bed dryer (case II). In case III the attempt is instead to develop an electroporation device to open cell membranes to accelerate drug discovery, and finally, in case IV we attempt to develop a method for characterising samples in an easy-to-use, non-destructive way.

Access to a vector network analyser (VNA) and a software-defined radio (SDR) was given, where a framework for using the VNA was developed in the open-source programming language Python. To analyse the retrieved data, extensions to normal regression methods (ordinary least square, principal component regression, and partial least square regression) dealing with so-called *improper* complex signals were derived and used, where the *widely linear* transform was utilised. The free, open-source multiphysics software ElmerFEM (with complementing software) was investigated and used to attain numerical results, were previous research relied on commercial tools such as COMSOL or HFSS.

The results of the thesis suggest that the current implementation of a monitor for the fluid bed (case II) leaves much to be desired, as the used antennas are greatly affected by process environmental changes which produce undesired deviations in measurements. The origin of the problem lies in that the antennas need to be placed inside the fluid bed process. In contrast, in case I the antennas can be placed slightly outside of the process and are as such protected against the flow and environmental changes enabling easier analysis of the data. Nevertheless, the potential of both implementations was observed. For both cases III and IV, the developed theoretical frameworks suggest great potential for quick, easy-to-use processes that may accelerate research within the corresponding fields. Unfortunately, experiments were concluded early, and the practical benefits are still mostly unexplored.

In conclusion, the potential of microwaves in the pharmaceutical industry was considered and found in all four studied cases. Still, much is left to discover, and

improvements are of the essence before the projects can be considered in real processes. The potential of using the same methods as the ones derived in the thesis for several other projects is noted, and as such the current thesis may lay as a foundation for subsequent research.

Keywords: Microwaves, fluid bed dryer, continuous flow chemistry, electroporation, cavity resonator, microstrip resonator, process monitor, complex signal processing, improper signals, widely linear transformation.

Acknowledgements

From start to finish, there have been many people involved for various reasons which have contributed to the final product of this thesis. And in my most sincere way, I direct my thankfulness to all.

As such, I would first and foremost like to express my thanks to my supervisors in AstraZeneca, Gustaf and Mats as they have had considerable effect on the thesis directions and choice of implementations. Gustaf Hulthe with his keen sight for practical implementation and development of hardware and Mats Josefson expertise in computers and data analysis has been the ultimate combination for the thesis and my time staying here. They have both a great sense of mentorship and pedagogy. Similarly, my examiner Hana Dobsicek Trefna and my supervisor Helena Rodilla with both their expertise in the studied area have had a big impact on the thesis and realisations of the project, while only meeting on a few occasions. Both have been extremely kind and helpful, and now after the thesis I regret not borrowing their expertise more than I did.

Several other people in AstraZeneca have also had a great impact on the general direction of the thesis, for instance by providing discussions on possible researched processes and projects that have been previously conducted on the site. As such I would like to express my thanks to Lubomir Gradinarsky, who provided data and insight on previous attempts on the fluid bed, and later Anders Holmgren who provided even more insight on the previous fluid bed projects. It was thanks to the conversations I had with them that the largest project, the fluid bed (Case II) was considered realistically. Subsequently, the methods developed for the continuous flow (case I) was also based on the ideas that were originally developed for the fluid bed. The conversation with Anders also led me to Mats Johansson, who very kindly gave me an introduction to the fluid bed and helped me set up Spiritus (the fluid bed used in the thesis), as well as perform initial experiments. I would also like to express my thanks to Johan Hjärtsam who provided me with sample granules and for intel on how to design some of my experiments. In the case of the fluid bed, the team of CBRE helped in fixing Spiritus so it could be operated, and the experiments could not be conducted without them, and have my sincere gratitude.

For case III, I would like to direct my thanks to Hagvall Sepideh and Susanna Abrahamsen for considering the electroporation project, and the initial meeting where important specifications of electroporation were discussed. I apologise for the early conclusion of the project but hope that my work may be a start for someone else.

Special thanks to Johan Forsgard of AstraZeneca and my older brother Eddie Nilsson for helping me 3D print materials and different construct, which helped me greatly in the early days of the thesis when I developed my preliminary ideas for the T-resonator (case IV).

For the modelling, the team behind Elmer has helped a lot in regard to hints and

explanations of the software, but also by updating and patching the software when there was a need for it. Without their help, there wouldn't be any numerical results except the analytical, in which they have my gratitude.

Thank you to all the people who have read and provided insight and improvements to the report, in which the only so far not mentioned is my dear mother, Annette Nilsson. Equivalently, I thank my dear father Roy Nilson for helping with various ideas I had at the beginning, which he supported with the precise cutting of various objects.
Lastly, a thank you to my partner Helene Rodelius who helped me in the midst of confusion and supported me from behind the scenes.

Robin Nilsson, Gothenburg, 6/ 2024

List of Acronyms

Below is the list of acronyms that have been used throughout this thesis listed in alphabetical order:

VNA	Vector Network Analyser
SDR	Software Defined Radio
TM	Tranverse magnetic
TE	Tramnverse electric
TEM	Tranverse electromagnetic
MUT	Material under test
OLS	Ordinary least squares
PCR	Principal component regression
PLS	partial least squares

Nomenclature

Below is the nomenclature of indices, sets, parameters, and variables that have been used throughout this thesis. More may be introduced for the specific projects, but will carefully be explained.

Indices

i,j	Indices for various sets

Sets

$\mathbb{R}/\mathbb{C}$	real/complex set

Variables

$\vec{E}$	electric field (V/m)
$\vec{H}$	magnetic field (A/m)
$\vec{B}$	magnetic flux density (Wb/m^2)
$\vec{D}$	electric flux density (C/m^2)
$\vec{M}$	magnetic current density (V/m^2)
$\vec{J}$	electric current density (A/m^2)
$Z, \underline{Z}$	complex vectors
Z^r, Z^i, Z_{Re}	real vectors
X (with underscores)	spectrum
Y	similar as Θ (see parameters)
$\Gamma, \underline{\Gamma}, \Gamma_{Re}$	covariance
C	pseudo-covariance

Z_0	characteristic impedance

Parameters

$\epsilon, \epsilon_0, \epsilon_r, \epsilon'_r, \epsilon''_r, \epsilon_{eff}$	permittivity of various kinds
$\mu, \mu_0, \mu_r, \mu'_r, \mu''_r$	permeability of various kinds
ρ	electric charge density
f	frequency
ω	angular frequency
$tan\ \delta$	tangent loss
$S11, S12, S21, S22$	scatter parameters
Θ, β	parameters to estimate
ε	white noise, possibly complex
V_{cyl}, V_s	volumes cylinder, volume sample

Contents

List of Figures

List of Tables

1
Introduction

1.1 Introduction

Within the pharmaceutical industry, microwaves, electromagnetic waves within the 0.3-300GHz frequency range, have since long been an interesting case of study for a wide range of different applications. Records of using microwaves for process optimisation in pharmaceutical processes may be found in early development phases to late production phases (1–4). The attractiveness of microwaves typically lies in their non-ionising nature, in which the photon energy it provides to a system is inadequate to release electrons from atoms as compared to e.g. X-rays (1). The provided energy can instead result in the heating of radiated materials, which can be utilised in specific heating of, for instance, continuous flows (1; 2). While well established, emerging research utilising these characteristics of microwaves suggests that the full capabilities of microwaves may still be unexplored (5–9).

The present thesis aims at exploring possibilities of using microwaves in a pharmaceutical setting. As the application area is wide, the study was limited to a few special cases. Specifically, the thesis investigated possibilities in the development of a process analytical technology (PAT) tool for monitoring two different pharmaceutical processes (case I and II), construction of a microwave electroporation protocol (case III), and characterisation of pharmaceutical drugs molecular properties (case IV). The thesis was made from both a theoretical and practical standpoint. The strengths and weaknesses of previous implementations found in the literature were examined, both theoretically and practically, and improvements were suggested and implemented. Additionally, open-source software tools were considered in order to improve accessibility, flexibility, and ability to reproduce results in academic or project start-up situations when funding for commercial software may be limited.

1.2 Aim

The overall aim of the report was to investigate a few cases of practical implementation of microwaves in pharmaceutical processes, following a theoretical base. Limitations in current research will be discussed, and possible improvements are both suggested and attempted. Access to a vector network analyser (VNA) and two types of software-defined radios (SDR) was given and was used to excite and measure microwaves of specified frequency and power. The two first cases were deemed

more practically implementable and were thus progressed further while the others were concluded early. A description of the four different cases (labeled Case I - IV) studied in this report will be provided in section 1.3.

For Case I and II, the aim was to develop a process monitor tool from theory to practical implementation based on the work conducted by Johan Nohlert (5) and Livia Cerullo (6). Limitations, strength and possible improvements for both cases will be discussed, as well as attempt at revising and improving previous accomplishments. As such, an aim is to provide and improve

- a theoretical framework setting up the problems,
- numerical simulations of the given systems,
- practical implementation and acquisition of data describing the systems, and
- a data analysis framework for the acquired data.

The derivation of analytical regression methods for the data analysis framework will be of importance, which is partly explained in chapter 3. For case III, we will attempt at developing a microwave device for electroporation of cells, where Schmidt et al. (7) and Ahortor et al. (8) have partially been influential. In Case IV the problem of characterisation of molecular and pharmaceutical particle (e.g., drugs) properties using a so-called T-resonator is considered. The idea is to explore capabilities of resonators as complements to current tools, in characterising specific properties of molecules and particles, such as porosity. For case III and IV, the projects were concluded prematurely after some initial experiments and idea suggestions due to time limitations. Possible progress directions utilising the same equipment as provided in this thesis will be discussed.

Another aim of the project was to exploit free open-source software and common objects typically easy to attain, to a reasonable degree. The ambition is to construct an easily reproducible project, utilising available tools independent of external limitations. As much previous work was accomplished by using commercialised software, we thus explore and re-implement their research using alternative free open-source software.

1.3 Studied cases in the thesis

Four cases are presented and will be referred to as; **Case I: Particle flow in pipe**, **Case II: Fluidized bed**, **Case III: Electroporation of cells**, and finally **case IV: Characterisation of chemical sample properties**. A short description accompanied with the general method used is provided here and is extended in corresponding chapters (4 - 7).

Case I: Particle flow in pipe
The case studies microwave microscopy as a means to monitor a continuous flow

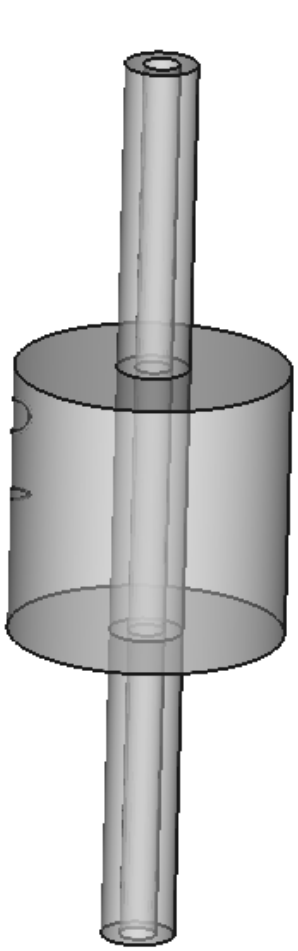

(a) Case I: Plastic pipe through the middle of a metal cylinder with two antennas connected on the left side of the walls.

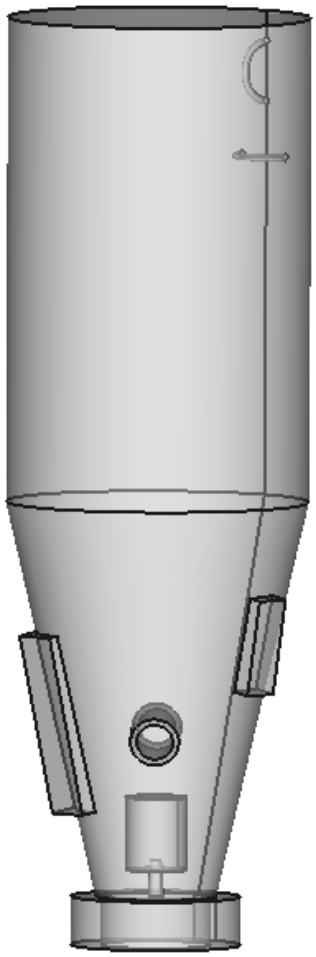

(b) Case II: A fluidized bed dryer with nozzle and Wurster tube (bottom), two windows (rectangles), one inlet hole (tube at the side of the wall), and two antennas connected to the upper-right wall.

Figure 1.1: Illustrative CAD models of the two cases, a) Case I, and b) Case II. Both models have two antennas attached, one horizontal, and one vertical aligned. Models were created using the FreeCAD CAD program.

of particles through a pipe. The overall aim is to characterise the properties of the particles (such as density and humidity) by first determining the electrical properties (permittivity) of the particles. Thereafter, the physical properties may be calculated by relating the permittivity to the corresponding property, or by means of statistical regression analysis. To accomplish this, a so-called *microwave cavity resonator* was constructed and fastened around the pipe where the particles flow and studied. In figure 1.1a) an illustrative model is shown of the system. The particles pass through a pipe in the middle of a metallic cylinder (cavity resonator) and are measured by the two antennas located at the left wall of the cylinder.

Case II: Fluidized bed dryer
The main objective of case II is essentially the same as for case I, but the system to monitor is now a so-called fluidised bed where the particles are studied in batches over longer sequences of time. The same principles may be used for case I, in which the fluid bed is considered as the cavity resonator, and the permittivity is calculated to later determine physical properties. The essential difference between case I and II is the effect the fluid bed process parameters have on the measurements, whereas such pre-processing of the data is required before determining particle properties.

In figure 1.1b) an illustrative model of the fluid bed is shown. There, particles in the fluid bed are contained inside the metallic walls and extracted by dissembling parts of the walls after conducting experiments. During experiments, heated air flows in from the bottom of the cylinder, subsequently elevating the particles while they are sprayed with a substance (e.g., water or ethanol), which effectively coats the particles while drying due to the hot air.

Case III: Electroporation of cells
Electroporation refers to the process of the effect an electromagnetic field has on cells. Specifically, if a sufficiently strong electromagnetic field is applied to a cellular body, a pore (or hole) is formed in the cell membrane (shell). If the electromagnetic field is too strong, the pore will be large and the cell will burst, effectively killing the cell. Commonly, this is referred to as irreversible electroporation. If instead the strength is controlled at sufficient low intensity, the cell will not burst and after treatment, it may reverse to its original state. This is referred to as reversible electroporation. In either case, electroporation occurs in milliseconds and is a rapid process. Reversible electroporation may be of special interest to cellular biologists, as it can assist diffusion and osmosis transfers (i.e., transfection) across the cell membrane. Irreversible electroporation could instead be used to kill specific areas of cells, such as tumours. Again the cavity resonator is considered for reversible electroporation in case III.

Case IV: Characterisation of Particle properties using a T-resonator
Particle properties, for instance, porosity, humidity, and dielectric properties are of great interest both in early pharmaceutical processes, but also in later. In early processes, knowing the properties of particles under test may assist in developing hypotheses or explaining attained results from other experiments. Later, it can be utilised as a quality analysis tool. The microwave *T-resonator* has been successfully

used for determining dielectric properties of materials in other industries, and could possibly be applicable for our purposes. As in cases I and II, we can then either derive a relation between the particle properties and the dielectric properties or by means of inferential statistical methodologies.

1.4 Layout of the report

Due to multiple cases/projects, where some fundamental theories coincide, the layout of the thesis will not follow the standard protocols (e.g., introduction-theory-method-results-discussion). The thesis will be divided into several chapters, where each case will be presented in an independent chapter (chapters 4 - 6) with corresponding applicable theory. Each such chapter will thus describe the process, the problem, previous and influential projects, methodology, results, and finally a discussion of the studied case. As several fundamental theories coincide within the projects, we dedicate one chapter of theory (chapter 2) covering common frameworks between the cases. Not all theories will be applicable for all cases though, and for clarity, the cases with respective associated applicable theories are described here:

- Section 2.1 provides general information about microwaves and is applicable to all cases.
- Section 2.2 provides a description of the so-called *microwave cavity resonator*, which is used for Case I - III.
- Section 2.4 provides fundamental theories of complex signal processing and regression analysis, used in Cases I and II.

Additionally, as Case I - II will be using a similar data analysis framework we will dedicate the reasoning and derivation of relevant theories to its own chapter, chapter 3. We note that this chapter should be considered as a result of the current thesis, as previous such derivations have not been provided to the author's best knowledge.

The thesis will conclude with a general discussion of the projects, and some remarks on other possibilities using microwaves in the pharmaceutical industry.

2

Theory

The current chapter aims to provide the fundamental theoretical frameworks which this thesis builds upon. Each later chapter which considers one of the four cases will provide additional theory corresponding to the specific case.

A special important concept to memorise is the so-called *microwave cavity resonator*, as it will be used by three of four projects in this thesis, and could likewise be used for the last project. A good way to visualise a cavity resonator is to imagine a microwave oven, as it essentially is the same.

We will divide the current chapter into essentially three parts: 1) *Fundamentals of microwaves*, which will provide some background on microwaves and how they are affected by materials. 2) *Microwave cavities*, how they principally work but also how they will be implemented in the thesis. 3) *Complex signal processing and regression methodology*, as it will be used in cases I, II, and IV.

2.1 Fundamentals of microwaves

Microwaves, which are a type of electromagnetic wave limited to 0.3 - 300 GHz frequencies, or 1 m - 1 mm wavelength, consist of both an electric and magnetic field, as explained by Maxwell's equations (10),

$$\vec{\nabla} \times \vec{E} = -\frac{\partial \vec{B}}{\partial t} - \vec{M}, \quad \vec{\nabla} \cdot \vec{D} = \rho \tag{2.1}$$

$$\vec{\nabla} \times \vec{H} = \frac{\partial \vec{D}}{\partial t} + \vec{J}, \quad \vec{\nabla} \cdot \vec{B} = 0 \tag{2.2}$$

$$\vec{D} = \epsilon \vec{E}, \quad \vec{J} = \sigma \vec{E}, \quad \vec{B} = \mu \vec{H}. \tag{2.3}$$

Here $\vec{E}$ is the electric field (V/m), $\vec{D}$ the electric flux density $(Coul/m^2)$, $\vec{H}$ the magnetic field (A/m), $\vec{B}$ the magnetic flux density (Wb/m^2), J the electrical current density (A/m^2), $\vec{M}$ the magnetic current density (V/m^2) and ρ the electric charge density (C/m^3). ϵ and μ are the permittivity and permeability, respectively. Generally, ϵ and μ can both be considered as complex and dependent on the angular

frequency $\omega = 2\pi f$ (f is the frequency). Typically, we assume that our vector fields ($\vec{E}, \vec{B}$ etc.) are time-harmonic, i.e. $\vec{A}(\vec{x}, t) = \vec{A}(\vec{x})e^{j\omega t}$ for $\vec{A} = \vec{E}, \vec{H}, \vec{M}, \vec{J}$ which provides several simplifications which we discover later.(10)

When an external electric field is applied to a media of *polar molecules*, the dipole moments of the molecules tend to align themselves in the same direction as the electric field, effectively polarising the molecules (10). In other words, the molecules rotate to align with the field, but since the field varies the molecules continue to rotate instead of going back to the original state. Therefore, microwave spectroscopy often also is referred to as rotational spectroscopy. During rotation - due to friction caused by the inertia of charged molecules - energy loss occurs and typically results in the heating of the material. (10)

This phenomenon is often modelled using so-called complex permittivity, and relates to Maxwell's equations through,

$$\epsilon = \epsilon_0 \epsilon_r, \quad \epsilon_r = \epsilon_r' - j\epsilon_r'', \quad j = \sqrt{-1} \tag{2.4}$$

where ϵ_r is the **relative permittivity** or **dielectric constant** of the material and $\epsilon_r', \epsilon_r''$ is the real and imaginary part of the relative permittivity, respectively. $\epsilon_0 = 8.854 \times 10^{-12} F/m$ is the permittivity in vacuum. Here, ϵ_r' describes how polarisable a material is while ϵ_r'' describes the phase shift between the polarisation and the electromagnetic field (10). A usual representation found in literature is also the **loss tangent**,

$$tan\ \delta = \frac{\epsilon_r''}{\epsilon_r'} \tag{2.5}$$

and measures the power loss in the media. The permittivity is typically dependent on the frequency, and a way to extend current formulations is by the *Debye relaxation* equation found in (10).

Similarly, a material can be described by how its ability to *magnetisation* is, which typically is measured with the property **permeability** (with $\mu, \mu_0, \mu_r = \mu_r' - j\mu_r''$ similar as above). In the current thesis, we assume $\mu_r = 1$ and may thus be neglected.

A direct effect of the permittivity and permeability of a material on microwaves is its effect on the propagating wave. The wavelength (or equal velocity), is then related to the frequency by (10),

$$\lambda = \frac{v}{f} = \frac{c}{\sqrt{\mu_r \epsilon_r}} \frac{1}{f} \tag{2.6}$$

where c is the speed of light.

2.1.1 Microwave resonance

For case I, II, and IV the overall specific aim is to accurately and effectively determine the permittivity of samples and subsequently use it to determine other properties.

As such we wish to utilise and develop methods that are sensitive to changes in the material of the samples. A common approach is to use microwave resonance in which the system is constructed to optimally operate on specific frequencies, and deviations/perturbations occur if properties in the material change. The recorded perturbation is then used to determine the permittivity of the sample under test.

There are several different types of microwave resonance constructs, and in this report, two were chosen for further study: microstrip resonators and cavity resonators. Both have been well studied in the literature (see (10) for a general introduction and discussion) and several variations have already been developed for various purposes (8; 9; 36; 57). In the subsequent section, we provide an introduction to the cavity resonator, while the microstrip T-resonator will be introduced in chapter 7.

2.2 Microwave cavities

A cavity, in the electromagnetic sense, is a closed chamber with well-conducting walls such that the microwaves are contained within the chamber. For the ideal theoretical case, the inner material of the cavity is source-free ($\vec{J} = \vec{M} = \vec{0}, \sigma = \rho = 0$), isotropic ($\epsilon, \mu$ scalars) and homogeneous (ϵ, μ constant). For the surface of the cavity, we assume well-conducting walls, and thus $\hat{n} \times \vec{E} = \hat{n} \times \vec{H} = 0$ and hence $\hat{n} \times \vec{\nabla} \times \vec{H} = \hat{n} \times \vec{\nabla} \times \vec{E} = 0$ were $\hat{n}$ is the normal of the surface. We can then easily derive the Helmholtz version of the equations,

$$\begin{aligned} \nabla^2 \vec{E} + w^2 \epsilon \mu \vec{E} &= 0 \\ \nabla^2 \vec{H} + w^2 \epsilon \mu \vec{H} &= 0. \end{aligned} \tag{2.7}$$

In appendix A.1 a detailed derivation can be found. With slightly more derivations, the Helmholtz equations give an interesting form of the equations, namely they provide an eigenvalue problem with eigenvalues ω and eigenvectors $\vec{E}$ and $\vec{H}$. In such cases, we aim to find eigenvectors H_m, E_m, and eigenvalues w_m that solve 2.7, and we note that there are almost infinitely many such solutions. Another way to describe the eigen solutions, which possibly are more common, is by denoting that the fields experience *resonance*. Consequently, we find both high electric energy dense areas, as well as high magnetic energy dense areas when the cavity is at resonance.

Note! Henceforth, we will use the designation *eigen solution(s)* and *resonant* interchangeably to describe the eigenvectors ($\vec{E}_m$ and $\vec{H}_m$) of Helmholtz equations outlined above, and thus refer to the electromagnetic fields (example in figure 2.1). Similarly, *eigenfrequency(ies)* and *resonant frequency* will be used to describe the angular frequency w_m. The only contradiction of this is in chapter 3, where we will use eigen solutions to derive data analysis methods.

For a given eigenvalue, w_m, a cylinder cavity may look like the one shown in figure 2.1a), where the high electric density areas are shown to the left, and corresponding magnetic fields to the right. We note that if a specific area is dense in electric energy,

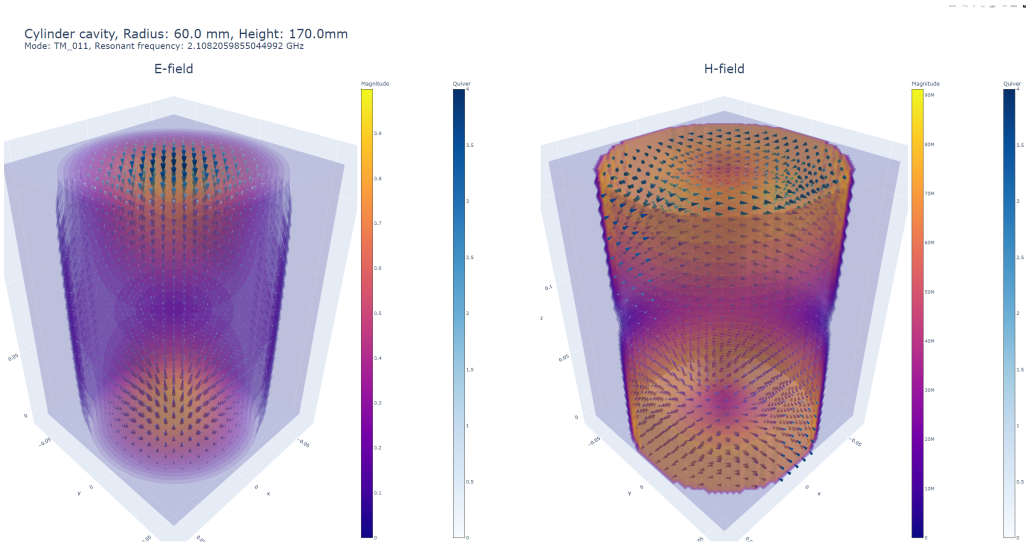

(a) Simulated cylinder cavity $\vec{E}$ and $\vec{H}$ fields with theoretical eigenvalue $w_m = 2.1GHz$. Here TM_{011} is shown.

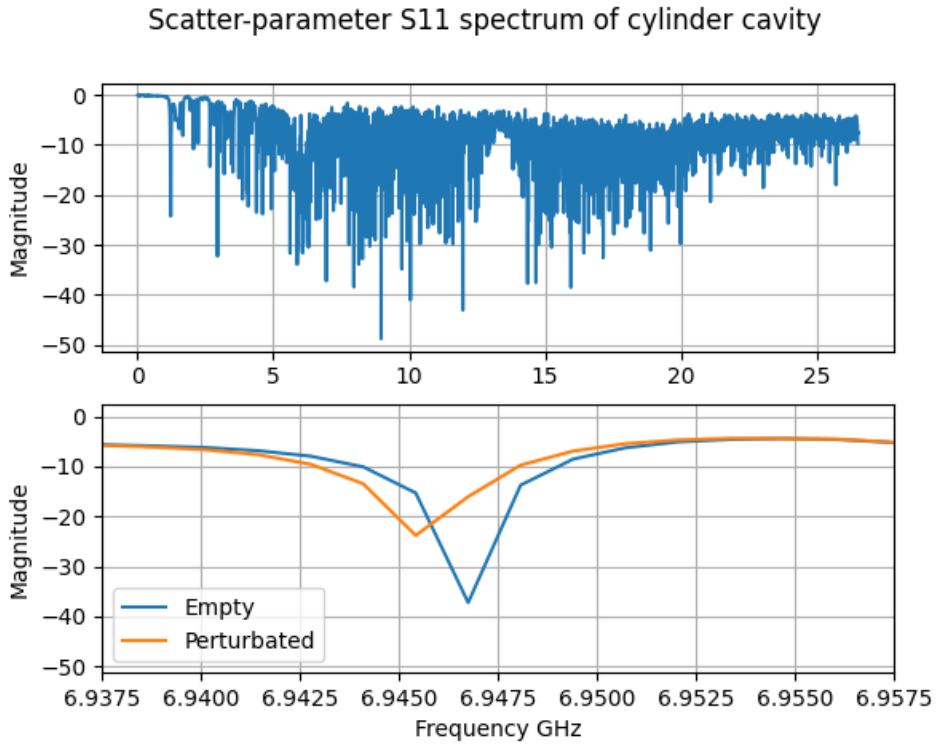

(b) Spectrum of a real cylinder with same height and radius as simulated. Upper: Full spectrum. Lower: spectrum around the resonant frequency given in fig (a) from empty cylinder (blue) and cylinder with introduced dielectric inside (orange).

Figure 2.1: Example of a microwave cavity, (a) simulated fields, and (b) spectrum from a real cavity.

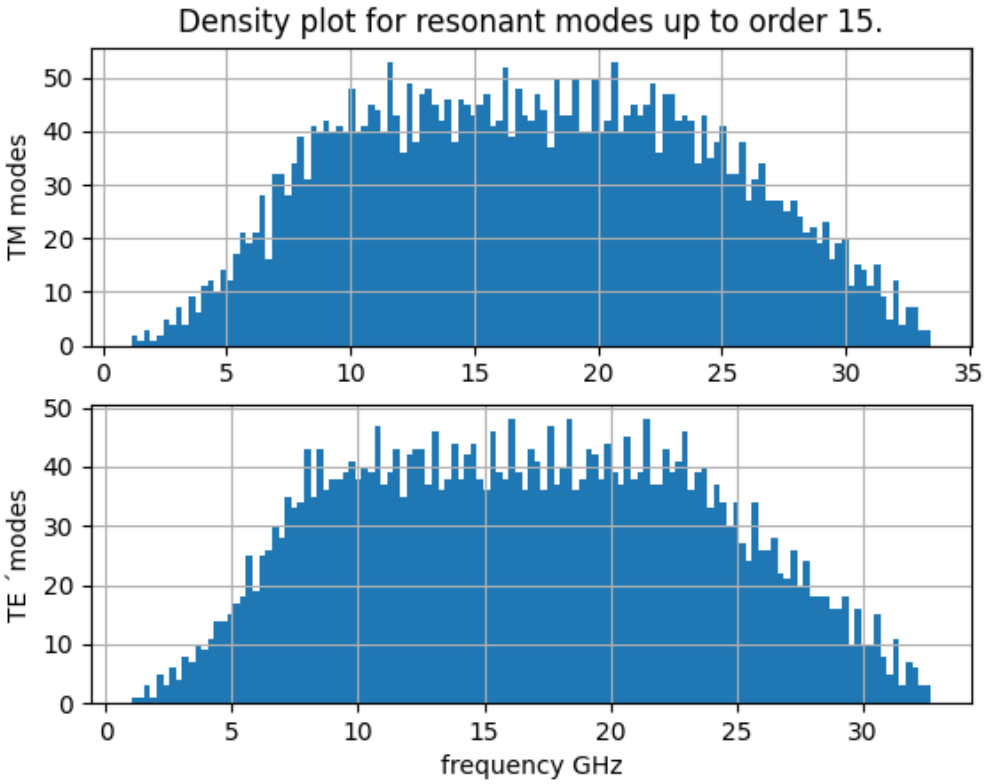

Figure 2.2: Histogram of the first 7440 resonant frequencies of the cavity cylinder in figure 2.1. Here TM and TE modes are separated.

it is not magnetic energy dense, and vice versa. This will prove to be an important fact in the construction of the antennas later. For simple shape cavities, such as cylinders and cuboids, the solutions may be derived analytically and the resonant frequency equations take on a specific form usually described by three parameters denoted by m, n, and p. The analytical solutions of a cylinder can be found in appendix C.

Additionally, by inspecting Maxwell's equations 2.1, we may note that either $H_z = E_Z = 0$, or only one is zero, and the other must be non-zero. This leads to the so-called *Transverse Electric (TE)* mode ($E_z = 0$, $H_z \neq 0$), *Transverse Magnetic (TM)* mode ($H_z = 0$, $E_z \neq 0$) or the *Transverse electromagnetic (TEM)* modes ($H_z = E_Z = 0$). Thus, for cylinders or cuboids, the typical way to refer to such eigensolutions is to combine the mode with m, n, and p to get TM_{mnp} or TE_{mnp}. While for other more complex cavities, the notion of m, n and p is non-existent, but may still obtain 'look-alike' solutions and are referenced as either TM_{mnp} or TE_{mnp} modes anyway (e.g., see (5)).

In 2.1 b) a measured spectrum (S_{11}) of a cylinder with the dimensions close to the cylinder in figure 2.1 a) can be found. We note that the measured resonant frequency (lower image: "Empty") for the analytical solution in 2.1 a) was found to

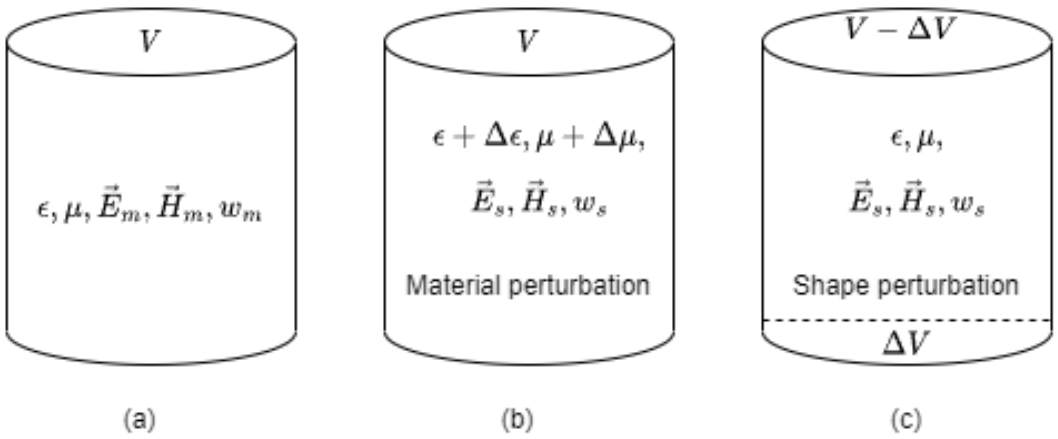

Figure 2.3: Perturbations of the cavity. In (a) the empty cavity is shown, in (b) the cavity with added material and in (c) changes in the cavity shape.

be around 6.95 as compared to the theoretical value 6.94 GHz, corresponding to the mode TM_{432}.

In figure 2.2 the histogram of approximately the 7500 first resonant frequencies for the cylinder in figure 2.1 is shown. The plot gives detailed information about the complexity of the system for different frequency ranges and will provide theoretical and practical importance in the data analysis section. In general, we note that the density of resonant frequencies is lower for lower-frequency areas, and increases as the frequency increases, up to a certain point. For cylinders and shapes resembling cylinders, in general, the histogram will be similar only shifting in frequency e.g., where the slope starts. In a range where the density is low the resonant frequencies are well separated and easier to analyse, as compared to high-density areas where there may even exist overlapping resonant frequencies. As a direct consequence, in most published work, their research is typically limited to only include low-frequency areas where the resonant frequencies are well separated and easier to analyse, as well as to compare to physical interpretations.

2.2.1 Perturbations of resonant cavity

Typically, there are two considered perturbations within a resonant cavity (10), shape and material perturbations. An illustration based on (10) is shown in figure 2.3, and the equations describing the shift in resonant frequency by these perturba-

tions are,

$$\begin{aligned}
\frac{w - w_m}{w_m} &= \frac{\int_V \Delta\epsilon \vec{E}_m^* \cdot \vec{E}_s + \Delta\mu \vec{H}_m^* \cdot \vec{H}_s dv}{\int_V \epsilon \vec{E}_0^* \cdot \vec{E}_s + \mu \vec{H}_0^* \cdot \vec{H}_s dv} \\
&\overset{\Delta\epsilon,\Delta\mu \text{ small}}{\approx} \frac{\int_V \Delta\epsilon |\vec{E}_m^*|^2 + \Delta\mu |\vec{H}_m^*|^2 dv}{\int_V \epsilon |\vec{E}_m^*|^2 + \mu |\vec{H}_m^*|^2 dv}, \quad \text{material perturbation,} \\
\frac{w - w_m}{w_m} &= \frac{1}{\omega_m} \frac{-j \int_{\Delta\Gamma} \vec{E}_m^* \times \vec{H}_s d\gamma}{\int_V \epsilon \vec{E}_m^* \cdot \vec{E}_s + \mu \vec{H}_m^* \cdot \vec{H}_s dv} \\
&\overset{\Delta V \text{ small}}{\approx} \frac{\int_{\Delta V} \mu |\vec{H}_m^*|^2 - \epsilon |\vec{E}_m^*|^2 dv}{\int_V \epsilon |\vec{E}_m^*|^2 + \mu |\vec{H}_m^*|^2 dv}, \quad \text{shape perturbation.}
\end{aligned} \tag{2.8}$$

In equation 2.8 we have assumed Γ to be the surface of the volume V, and for the shape perturbation $\Delta\Gamma$ the 'removed' surface of the 'removed' volume ΔV of V. We have made two assumptions; the homogeneity of the inner material remains after introducing a new material in the material perturbation, and second that we have added a volume to the inner part of the cavity, and not removed it. Nevertheless, they provide important insight into how the system works, where for instance the shape perturbation method could be utilised to accommodate for added screws. While not stated, an important assumption of these equations is that the resonant frequencies are well separated. Thus for the example cylinder in figure 2.1, the above equations lose the validity around $> 5GHz$ as seen in the histogram in figure 2.2.

The equations in 2.8 tells foremost one important piece of information, namely that each eigenfrequency is affected by the whole cavity fields. While this may not come as a surprise, it affects for instance positional estimations procedures greatly. Figure 2.1a) illustrates this perfectly, as it has two electric energy-dense areas and an introduction of dielectric material in any of these would result in more or less the same change in spectrum. As a direct result of this, several resonant frequencies must be used in combination to understand the process, while more resonant frequencies require more complex data analysis methods.

2.2.2 Excitation antenna and field-measurement probes

We present here a truncated explanation of the coupling probe used in the thesis and provide a more in-depth explanation and reasoning in appendix D. In short, we have essentially two choices of antennas that we can use for our purposes, either a so-called E-probe or a so-called H-probe. Of course, other versions exist (11; 12), but they are either unfit for the processes or require reformulation of several theories which would be time-consuming. The E-probe is a straight antenna directly pointing into the cavity and measures changes in the electric field (thus the 'E'). The H-probe is instead bent and short-circuited into the walls of the cavity and measures changes in the magnetic field (thus the 'H'). Optimal places to put the E-probe would thus be in an electric energy-dense area, and vice versa for the H-probe. As we intend to measure the changes in electric energy-dense areas, it is undesired to put an antenna there as it may affect the process, which is especially true for the fluid bed. Similarly, in the case of the fluid bed we are restricted to putting the antennas along the side

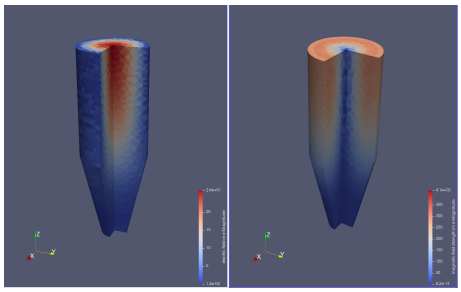

(a) TM_{010} found at 0.93GHz.

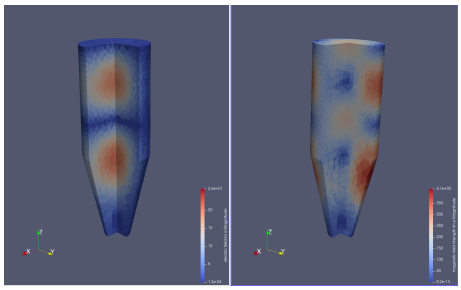

(b) TE_{112} found at 0.90GHz.

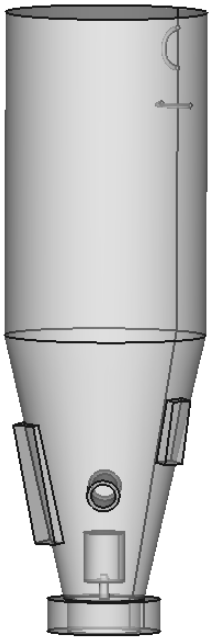

(c) Cad model, antennas at top right.

Figure 2.4: Antenna construction in the fluid bed dryer. Left images (a and b) shows electric (left) and magnetic (right) fields for two different modes. The right image (c) is a CAD model of the fluid bed dryer. The Elmer software was used for the numerical results in the left images.

walls, and as such to measure frequencies similar to the TM_{011} mode (see figure 2.2), the E-probe would need to be very long. Thus, the H-probe seems to be a better fit. Since the H-probe is short-circuited to the walls, we also provide the mechanism with protection towards static voltages which may occur due to triboelectric charging of granules (5).

For the monitoring cases, cases I and II, we will make one last addition: two H-probes connected to the walls will be used. One will be rotated with its face normally directed horizontally, and as such it will measure TE modes, while the other will be rotated vertically and measure TM modes. This is illustrated for the fluid bed in figure 2.4, where the upper antenna measures TM modes, and the lower measures TE modes. For TM_{010}, the upper antenna is placed in the upper-top right where the magnetic field is the strongest, rotated with its face normally vertically aligned, and the dielectric object passing through the top-middle of the fluid bed (where the electric field is the strongest) is ideally measured. Similar reasoning applies to the lower antenna, where if we wish to couple to the TE_{112} mode it should be placed slightly lower than the upper antenna, and may ideally measure from two regions in the middle of the fluid bed.

2.3 Vector network analyser and software-defined radios

To excite microwaves, the antennas will be coupled to either a vector network analyser (VNA; Keysight P5005A USB VNA, 26.5 GHz) or a software-defined radio (SDR; national instruments USRP N320, 6 GHz). While an SDR may be viewed as a radio, sending information with a set frequency and amplitude (13), the VNA works a bit differently where it sweeps over a wide range of frequencies and measures the response by either transmittance or reflection. The VNA is thus ideal for analysing *linear* electrical systems, where finding specific frequencies (such as resonance frequencies) is the objective (14). In the current thesis, a two-port VNA (ports 1 and 2) was used, and thus there is a total of four different combinations of measurement parameters; S11 and S22 which measure reflection in the system of port 1 respectively 2. S12 and S21 which measures transmittance of the ports from port 1 to port 2 (S12), and vice versa from port 2 to 1 (S21). S11, S22, S12, and S22 are commonly labelled as *scattering parameters* and sometimes jointly as *snp* values, while the 4×4-matrix with elements S_{ij} is commonly referred to as the *scattering matrix* (14).

For clarity, in all forthcoming texts, we denote a *spectrum*, which may include one or more scatter parameters, as a measurement of the VNA containing multiple frequencies. Typically, we will use X to represent several spectrum samples by the VNA. We note that a spectrum is a complex vector containing both amplitude and phase of the data, and processing of such should be in accordance to *complex signal processing*. The equations relating the scattering parameters to a cavity resonator are outlined in appendix B.

2.4 Complex signal processing and regression methodologies

In this section, relevant data analysis and statistics will be provided. In particular, complex signal theory will be covered including complex Gaussian distributions and assumptions that simplify analysis greatly, and how to deal with cases where such assumptions are invalid.

For the complex signals, we will assume that the sent signals, Z, is a complex-valued vector transferred through a system of unknown characteristics, but which add complex Gaussian noise. As such it is of interest to study a complex-valued random vector sampled from a complex Gaussian distribution. We will note that complex normal vectors are in general more difficult to deal with than real-valued random vectors, mainly due to the so-called characteristic *impropriety* of the data. We will provide a simple test for checking the impropriety of the data, and present a transformation typically used to treat improper data, commonly called the *widely linear transform*. Assuming the system is linear, we will describe extensions of normal linear regression which accommodates complex-valued vectors and helps to

approximate the systems.

2.4.1 Complex random vectors

Formally, let $Z = [Z_i]_{i=1,2,...,n}$ be a complex random vector of n independent complex random variables on a probability space $(\Omega, \mathscr{F}, P)$, such that $Z : \Omega \to \mathbb{C}^n$, and $[Real(Z_i), Imag(Z_i)]_{i=1,2,...,n}$ is a real random vector on $(\Omega, \mathscr{F}, P)$.

For a complex random vector, we define the complex expectation, covariance, and pseudo-covariance as

$$\mu = E[Z] = [E[Z_i]]_{i=1,2,..,n}, \quad \text{expectation} \tag{2.9}$$
$$\Gamma = Cov[Z, Z] = E[(Z-\mu)(Z-\mu)^H] \quad \text{covariance} \tag{2.10}$$
$$C = Cov[Z, Z^*] = E[(Z-\mu)(Z-\mu)^T] \quad \text{pseudo-covariance.} \tag{2.11}$$

Here $E[Z_i] = E[Real(Z_i)] + jE[Imag(Z_i)]$, $(.)^*$ denotes conjugate, and $(.)^H = (.)^{*T}$ denotes the Hermitian transpose. An important property of Γ is that it is Hermitian, i.e., $K_{ZZ}^H = K_{ZZ}$, and positive semi-definite, i.e., $a^H \Gamma a = 0 \ \ \forall a \in \mathbb{C}^n$. The pseudo-covariance C is simply symmetric, i.e., $C^T = C$.

An important concept for complex vectors is if the vector is so-called circular symmetric or proper, as this simplifies analysis greatly.

Definition 2.4.1 (Circular-Symmetric) *A zero-mean (or undefined mean) complex random vector Z is called circular-symmetric if the distribution of Z and $e^{j\phi}Z$ is the same for any $\phi \in [-\pi, \pi)$.*

By definition of covariance for $e^{j\phi}Z$, we have $cov[e^{j\phi}Z, e^{j\phi}Z] = E[e^{j\phi}Ze^{-j\phi}ZZ^H] = E[ZZ^H] = cov[Z, Z]$, but for pseudo-covariance, $cov[e^{j\phi}Z, e^{-j\phi}Z^*] = E[e^{j\phi}Ze^{j\phi}ZZ^T] = e^{j2\phi}E[ZZ^T] = e^{j2\phi}cov[Z, Z^*]$. Thus for Z to be circular-symmetric, $C = 0$. Properness of a complex random vector has a similar definition, with the addition that the variance of all random variables of Z, Z_i, $i = 1, 2, ..., n$ is defined (i.e., $Z_i < \infty$).

It is easy to derive that if a complex vector is circular-symmetric or proper, it means that the real and complex values are uncorrelated (15), and their covariances are equal (due to $C = 0$).

2.4.2 Complex multivariate Gaussian distribution

A typical case of study in signal processing is the Complex Gaussian (normal) distribution. In this case we say that Z is a complex Gaussian random vector if $Z_{Re} = (Z^{rT}, Z^{iT})^T := (Real(Z)^T, Imag(Z)^T)^T$ is a random Gaussian vector, and we write $Z \sim CN(\mu, \Gamma, C)$.

The pdf of a complex Gaussian distribution is

$$f(z) = \frac{1}{\pi^n \sqrt{\det(\Gamma)\det(P)}} \exp\left\{ -\frac{1}{2} \left((z-\mu)^H, \quad (z-\mu)^\intercal \right) \begin{pmatrix} \Gamma & C \\ \overline{C} & \overline{\Gamma} \end{pmatrix}^{-1} \begin{pmatrix} z-\mu \\ \overline{z}-\overline{\mu} \end{pmatrix} \right\} \tag{2.12}$$

where $P = \overline{\Gamma} - C^H \Gamma^{-1} C$. The important property of the Complex Gaussian distribution is that it is completely described by its expected value, covariance, and pseudo-covariance. Here it will be evident why a circular-symmetric complex vector is an interesting case of study in which $Z \sim CN(0, \Gamma, 0)$. Z can thus be completely described by the covariance matrix and helps analysis as only the covariance matrix needs to be studied.

In the slightly more general form, when $Z \sim CN(0, \Gamma, C)$, the covariance of the so-called augmented form of z, $\underline{Z} = [Z^T, \ Z^H]^T$, called the augmented covariance matrix, $\mathbb{E}[\underline{Z}\ \underline{Z}^H]$, instead completely explains the data (16). Writing the augmented covariance matrix out, we get

$$\begin{aligned} \underline{\Gamma} = \mathbb{E}[\underline{Z}\ \underline{Z}^H] &= \mathbb{E} \begin{bmatrix} Z \\ Z^* \end{bmatrix} [Z^H, \quad Z^T] \\ &= \begin{bmatrix} E[ZZ^H] & E[ZZ^T] \\ E[Z^*Z^H] & E[Z^*Z^T] \end{bmatrix} \\ &= \begin{bmatrix} E[ZZ^H] & E[ZZ^T] \\ E[ZZ^T]^* & E[ZZ^H]^* \end{bmatrix} \\ &= \begin{bmatrix} \Gamma & C \\ C^* & \Gamma^* \end{bmatrix} \in \mathbb{C}^{2N \times 2N} \end{aligned}$$

which proves that the augmented covariance matrix contains the complete information of the system. Similarly, we have the real-valued covariance

$$\begin{aligned} \Gamma_{Re} = E[Z_{Re} Z_{Re}^T] &= \frac{1}{2} \begin{bmatrix} Real(\Gamma + C) & Imag(-\Gamma + C) \\ Imag(\Gamma + C) & Real(\Gamma - C) \end{bmatrix} \\ &= \frac{1}{2} \left(\begin{bmatrix} Real(\Gamma) & -Imag(\Gamma) \\ Imag(\Gamma) & Real(\Gamma) \end{bmatrix} + \begin{bmatrix} Real(C) & Imag(C) \\ Imag(C) & -Real(C) \end{bmatrix} \right) \in \mathbb{R}^{2N \times 2N}. \end{aligned}$$

and thus also contain all information to describe Z. The advantage of using the *real composite covariance matrix*, Γ_{Re}, instead of the augmented covariance matrix $E[Z_{Re} Z_{Re}^T]$, is that arithmetic operations are faster using real numbers as compared to complex.

2.4.3 Statistical tests for impropriety

Many different statistical tests have been derived to check for impropriety or if the circular-symmetric assumptions hold (17; 18) of a signal X. Essentially, most boil down to the simple observation that the proper signals maximise the entropy of the

signal:

$$\begin{aligned} H_{improper} &= \frac{1}{2} log[(\pi e)^{2n} det(\underline{\Gamma})] \\ &= \underbrace{log[(\pi e)^{2n} det(\Gamma)]}_{H_{proper}} - I(X; X^*) \end{aligned} \tag{2.13}$$

where $H_{improper}$ is the entropy and $I(X; X^*) \geq 0$ is the *mutual information* between X and X^*. Here we can estimate $I(X; X^*)$ without loss of information by (17)

$$\begin{aligned} I(X; X^*) &= \frac{1}{2} log(1 + \rho_1), \\ \rho_1 &= 1 - \frac{det\ \underline{\Gamma}}{det^2\ \Gamma}. \end{aligned} \tag{2.14}$$

It is evident that $H_{imporper}$ is maximised when ρ_1 is zero.

2.4.4 Complex signal processing and system estimation by regression

Informally, we assume a signal X is sent over a system f and retrieved as the response Y where noise in the system may occur. Formally, assume we have an independent variable $X \in \Omega \subset \mathbb{C}^n$ and a dependent variable $Y \in \Omega_Y \subset \mathbb{C}^m$, such that X and Y are known, and that the map

$$f : \Omega \to \Omega_Y : Y = f(X\ ;\ \theta) + \varepsilon \tag{2.15}$$

is unknown. Similarly ϵ here represents a random noise such that $\varepsilon \sim CN(0, \Gamma_\theta, C_\theta)$ for some Γ_θ, C_θ. θ is a set of scalar parameters generally unknown and to be estimated for a given assumed map f. The problem is then to find the true f and β such that equation 2.15 holds. Of course, finding the true solution is nearly impossible, and different methodologies to estimate f have been developed, typically by assuming a certain form of f. As such, if we note the assumed form of f by $\hat{f}$, we estimate θ with $\hat{\theta}$ by regressing X to Y: $Y = \hat{f}(X\ ;\ \hat{\theta})$.

2.4.4.1 Linear systems

Let us first present the real case, and in the next section extend the theory to the complex space. Thus, we assume a linear relationship between the now real vectors X and Y, and the aim is to estimate[1] β with $\hat{\beta}$:

$$\begin{aligned} &min||Y - \hat{Y}||_2^2, \quad \hat{Y} = X\hat{\beta}, \quad \text{and} \\ &Y = X\beta + \varepsilon \ \text{ with } X \text{ and } Y \text{ known.} \end{aligned} \tag{2.16}$$

Linear regression models, such as ordinary least squares (OLS), principal component regression (PCR), or partial least squares (PLS) regression in these cases are then

[1] The equations used are of the least-square notation, but others also exist. For instance see (17).

often subject to study, as the underlying process is mathematically fully understood. In each of the mentioned methods, the covariance or cross-covariance matrix is fundamentally what is studied. In chapter 3 implementation of these is discussed for complex signals.

Extension from linear to non-linear versions, i.e. by using kernels, as well as iterative versions will be discussed in appendix E. An iterative extension may be needed if either the data is sampled continuously, or if the size is too large to handle at once.

2.4.4.2 Extension into the complex space

As we noted before, the covariance of an improper signal does not explain the data completely, and this fact is what essentially separates the versions below. Let us begin with the simpler case; let us assume the error, ε in 2.15 to be circular-symmetric complex normally distributed such that $\varepsilon \sim CN(0, \Gamma, 0)$. This case is almost analogous to the real space regression analysis, except when using transpose, $(.)^T$, the Hermitian transpose, $(.)^H$, should be used instead. Thus, rewriting existing regression methods to a corresponding circular-symmetric version is typically straightforward.

As mentioned previously, in the improper case where $\varepsilon \sim CN(0, \Gamma, C),\ C \neq 0$, we need to extend the analysis methodology to accommodate the pseudo-covariance. In this case, we utilise the results from section 2.4.2, and note that both the augmented contain Γ and C. Using the augmented form of $\underline{X} = [X^T, X^H]^T$, we extend equation 2.16 as,

$$\begin{aligned} Y &= X\beta_0 + X^*\beta_1 + \varepsilon \\ <=> \underline{Y} &= \underline{X}\ \underline{\beta} + \underline{\varepsilon} \end{aligned} \tag{2.17}$$

and attempts at approximating both β_0 and β_1. The common name of this extension is the *widely linear transform*, as it tries to solve the linear problem both in X and X^*. The lower equation in 2.17 is the augmented form of the widely linear transform, and we should quickly note here that $\underline{\beta} \neq [\beta_0, \beta_1]$ which is a common mistake, but rather

$$\underline{\beta} = \begin{bmatrix} \beta_0 & \beta_1 \\ \beta_1^* & \beta_0^* \end{bmatrix}.$$

The lower part of $\underline{\beta}$ may seem redundant, as it essentially is only the conjugate of the upper part, but for instance, gives a square form of $\underline{\beta}$ if β is square itself, which can provide simplifications in various analysis steps. Another important matrix in widely linear transformations is the so-called *linear transformation matrix*, or *real-to-complex* matrix which can be used to transform the augmented vector to the real composite vector. If we let I_m be the $m \times m$ identity matrix were m is the number of variables in X, the linear transformation matrix of X is then

$$T_m = \begin{bmatrix} I_m & -jI_m \\ I_m & jI_m \end{bmatrix}$$

and with $X_{re} = [Real(X)^T, Imag(X)^T]^T$, it can be used as

$$2X_{Re}^T = \underline{X}^T T_m \tag{2.18}$$

$$\underline{X}^T = X_{Re}^T T_m^H. \tag{2.19}$$

The next chapter will derive both circular-symmetric and widely linear versions of the regression methods OLS, PCR, and PLS applying the above-mentioned techniques.

3

Data analysis for cases I, II, and IV

We will dedicate this chapter to explaining the data analysis developed and used for cases I, II, and IV which relates perturbations to properties. For case III such analysis is not explicitly required.

3.1 Construction of the problem

In Cases I, II, and IV we wish to utilise perturbations in microwave resonant devices to accurately determine the dielectric properties of materials under test (MUT). As such, a simple way to view each recorded spectrum (scatter parameter), S_{np}, is as the spectrum recorded in its initial state without any material present, S_{np}^0, added to the perturbations, $dS_{np}^{Perturbation}$. Depending on the construction used, we may later extend the theory and analysis of $dS_{np}^{Perturbation}$ to determine the effect the MUT(s) have on the measurements and subsequently the present dielectric property. Common between the analysis methods is that several resonant frequencies will be observed in conjunction.

Case I:
Assuming there is no external disturbances, the only difference is a result of the change of dielectric materials flowing through the pipe. As such, we may view the measured spectrum as

$$S_{np} = S_{np}^0 + dS_{np}^{MUT(s)} + \varepsilon \tag{3.1}$$

where $\varepsilon \sim CN(0, \Gamma, C)$ is complex-valued Gaussian noise and $dS_{np}^{MUT(s)} = dS_{np}^{Perturbations}$. The changes by the material(s) under test, $dS_{np}^{MUT(s)}$, alter depending on the position of MUT(s) and different material properties such as humidity, porosity, and the substance molecular structure. Due to positional relevance, fast sampling of the spectrum is desired (5). During sampling, we may not know where a MUT is located; if it is at the top of the cylinder cavity, in the middle, or at the bottom; we may neither determine geometrical transformation or the quantity of MUT(s). Thus, previous attempts adopting the Maxwell-Garnett mixing model to estimate permittivity may fall short as the sampling process would retrieve inconsistent samples for same-valued MUT(s). The proposed method of the thesis is instead to

use inferential statistics such as regression and correlation of a number of experiments of known properties. In section 3.2 a relation between permittivity - where Maxwell-Garnett formula may be adopted - and desired substance properties is provided while in section 3.3 derivation of complex-valued linear regression methods is instead offered.

Finally, a way to simplify the above analysis is based on assuming sufficient separation between the resonant frequencies, in which we may write the scatter parameters as a series of poles (5)

$$S_{np}(w) = \sum_m \frac{\alpha_m}{w - w_m}.$$

In the close proximity of one of the poles, the equation simplifies to only one part of the sum in which it is possible to rewrite and simplify the expression as a Möbius Transform. This may assist analysis as we can apply common transformations to simplify the complex-valued analysis (5).

Case II:
In case II, airflow, temperature, etc. effects measurements in a non-trivial way, thus the addition of an environmental variable is required;

$$S_{np} = S^0_{np} + dS^{Environment}_{np} + dS^{MUT(s)}_{np} + \varepsilon. \tag{3.2}$$

While $dS^{Environment}_{np}$ could be used to certify correct mechanical configurations, it is inherently undesired. We thus seek to either mitigate or estimate the environmental effect such that we are left with a similar problem as in case I. Mitigation can only be accomplished by physical changes to the antenna and system, and may only partially mitigate $dS^{Environment}_{np}$. Instead, we seek ways to properly estimate it. Again, we accomplish this by considering inferential statistics by first removing MUT(s) (i.e. $dS^{MUT(s)}_{np} = 0$) and studying the system parameters separately, to later use the known parameters to estimate the $dS^{Environment}_{np}$. As such, let $S'_{np} = S_{np}|_{dS^{MUT(s)}_{np}=0}$ while Θ and $\Theta' = \Theta|_{dS^{MUT(s)}_{np}=0}$ be known specified mechanical parameters (such as temperature or airflow). In essence, the following simple steps enable subsequent steps to be of the same characteristics as for case I.

1. measuring dS^0_{np}, dS'_{np} separately,
2. estimate $B:\ B\Theta' = S'_{np}$, and
3. estimating $dS^{Environment}_{np} = B\Theta - S^0_{np}$.

Here, we use the developed regression methods in section 3.3 as a means to estimate B.

Case IV:
In case IV we will only consider one substance, and as opposed to case I and II the resonant frequencies are simply manifolds of the natural frequency. Thus it may serve as a means to calculate mean changes in the frequency shifts. Yet again

MUT properties may either be determined using the methods of section 3.2 or by statistical inference.

3.2 Physical interpretation of $dS_{np}^{MUT(s)}$

If S_{np} and $dS_{np}^{MUT(s)}$ can be successfully separated from dX_E, the next step is to derive a physical interpretation of the acquired data. Ultimately, we will consider two different cases; full continuous flow (continuous arrival of samples) and partial impulse flow (stochastic arrival of samples) which may be used depending on the situation. The first mentioned is useful if the sample occupies the whole sample holder, and the cavity is a cylinder. Thus, depending on how an experiment is performed it may be useful for case I. The second solutions are more general and can be used for both case I and II.

3.2.1 Full continuous flow

Dielectric properties inside the pipe can be calculated for the fundamental frequency mode, TM010, by (19)

$$\epsilon' = 1 + 0.539\frac{V_{cyl}(f_0 - f_{sample})}{V_{sample}f_0}$$
$$\epsilon'' = 0.269\frac{V_{cyl}}{V_s}(\frac{1}{Q_{sample}} - \frac{1}{Q_0}).$$

Here V_{cyl} is the resonant cavity's volume, V_{sample} the volume of the sample (+ holder, in this case, the pipe), f_0 is TM010 resonant frequency, f_{sample} the measured resonant frequency after the sample is introduced. This formula is valid when the sample volume is relatively small to the cavity volume, and the sample material is approximately homogeneous. Thus, using a small pipe and considering a full-flow scenario where the material in the pipe should be consistent, this model could e.g., possibly detect undesired samples inside the pipe.

3.2.2 Stochastic flow

Here we propose a similar, but slightly extended methodology as the one provided by Nohlert (5) and Lvivia (6), in which the Maxwell-Garnett mixing formula combined with the Debye formula was used for different regions within the cavity. For each eigenfrequency w_m, equation 2.8 (material perturbation) may be approximated by (6)

$$\frac{w - w_m}{w_m} \approx \frac{\int_V \Delta\epsilon|\vec{E}_m^*|^2 dv}{\int_V 2\epsilon'|\vec{E}_m^*|^2 dv}. \tag{3.3}$$

An additional, but often quite wrong, assumption would be a homogeneous material over the cavity, and as such,

$$\frac{w - w_m}{w_m} \approx \frac{\Delta\epsilon}{2\epsilon}. \tag{3.4}$$

While wrong, it provides an easy way to analyse the data in relation to the physics. Instead, a good approximation of the integrals can be accomplished by proper modelling and numerical results of the system. Another possible way to accommodate for the last approximation could be to regress values of w and w_m to ϵ for some known values of ϵ and measured values of w and w_m. We note here that by the Maxwell-Wagner effect, we can approximate ϵ by the effective permittivity, in which the Maxwell-Garnett mixing formula or Debye's formula can be used, similar to what Nohlert (5) and Lvivia (6) accomplished.

Both these versions may adapt extensions or be reformulated to better relate to the sought physical properties. For instance, in (20) equations of resonant cavity dielectric measurements were extended to accommodate for both impurities and porosity. E.g. for the *fractional porosity*, P, we have,

$$\epsilon'_r = \epsilon'_{eff}\left(1 - \frac{3P(\epsilon'_{eff} - 1)}{2\epsilon'_{eff} + 1 - P + P\epsilon'_{eff}}\right) \tag{3.5}$$

$$tan\delta = (1 - P)tan\delta_0 + AP\left(\frac{P}{1 - P}\right)^{2/3} \tag{3.6}$$

where $tan\delta$ is as eq. 2.5, and δ_0 and A are fitted towards relevant data. Several more of these derivations may be found in the literature for other characteristics, such as humidity (21), but as a first step only an implementation of porosity was attempted.

3.3 Derivation of complex linear regression models

In this section, we will provide details on the OLS, PCR, and PLS regression methods used later in the report. Thus, we attempt at solving the linear systems,

$$Y = XB \qquad \text{circular-symmetric} \tag{3.7}$$

$$Y = XB_1 + X^*B_2 \qquad \text{widely linear} \tag{3.8}$$

were $Y \in \mathbb{C}^{N\times p}$ and $X \in \mathbb{C}^{N\times m}$ are assumed complex. For each case the real, circular-symmetric, and widely linear versions are provided. In the derivations singular value decomposition (SVD) or eigenvalue decomposition (EVD) of the covariance matrix will be used and may be reviewed in e.g. (17).

Several articles have suggested widely linear re-formulations of standard data processing methods, for either theoretical or practical use. In the current thesis, we especially recognize (17; 22; 23), where (22) especially developed kernel-based statistical complex component analysis methods, such as Linear Discriminant Analysis (LDA), Canonical Correlation Analysis (CCA), Locality Preserving Projections (LPP) and Principal Component Analysis (PCA) in its corresponding widely linear

re-formulation. In the current thesis, we are more interested in regression-based algorithms, but the algorithms can be reused to derive results and formulate them to their corresponding regression version. In article (23), widely linear complex partial least squares (WL-CPLS) regression was derived, which can be directly used. The article though contains several mistakes in the widely linear formulation, and some parts need to be re-derived. The book *Statistical Signal Processing of Complex-Valued data* by Peter J.S. and Louis L.S (17) contains plenty of proper, well derived statistical analysis which can be utilised in practical applications or as building blocks of new algorithms. In the current case, Ordinary Least Squares (OLS), Principal Component Regression (PCR), and Partial Least Squares (PLS) will be derived and evaluated for the current problem.

To measure the quality of predictions, we will use the Goodness of Prediction metric *Predictive power*, or Q2, defined by

$$Q2 = 1 - \frac{\sum |x_{real} - x_{pred}|}{\sum |x_{pred} - \overline{x}_{pred}|}. \tag{3.9}$$

3.3.1 Ordinary least square (OLS)

Solving 3.7 using OLS in the real case, we simply multiply each side with X^T and the inverse of the covariance matrix, $(X^T X)^{-1}$, to get the approximation,

$$B = (X^T X)^{-1} X^T Y. \tag{3.10}$$

Essentially, it is the cross-covariance between X and Y, times the inverse of the covariance of X.

3.3.1.1 Circular-Symmetric OLS

The circular-symmetric version is analogous to the real version, where the only difference lies in the cross-covariance and the covariance which uses the Hermitian transpose instead of the normal transpose. We get the approximation,

$$B = (X^H X)^{-1} X^H Y. \tag{3.11}$$

3.3.1.2 Widely Linear OLS

We note that,

$$Y = XB_1 + X^* B_2 = [X, X^*] \begin{bmatrix} B_1 \\ B_2 \end{bmatrix} = \underline{X} \begin{bmatrix} B_1 \\ B_2 \end{bmatrix}$$

and thus

$$\underline{Y} = \underline{X} \begin{bmatrix} B_1 & B_1^* \\ B_2 & B_2^* \end{bmatrix} = \underline{XB}.$$

We regress as before and retrieve the approximation,

$$\underline{B} = (\underline{X}^H \underline{X})^{-1} \underline{XY}, \tag{3.12}$$

and extract B_1 and B_2 from the matrix above.

3.3.2 Principal component analysis regression (PCR)

We will use either the SVD or EVD versions of the PCA for the PCR derivation. The idea of PCR is to project X into a subspace of the original data that still explains most of the variance of the data, before regressing it to Y. We use SVD to decompose X as,

$$X = U\Sigma V^T$$

and let $T = U\Sigma$ to get $X = TV^T$. Here Σ is a diagonal matrix with descending values, thus the first columns describe the variance more so than the latter. By truncating T and V by only keeping a subset of the first columns we essentially project the original data to a lower subspace, and get

$$X_{truncated} = T_{truncated}V_{truncated}^T.$$

Let $\tilde{X} = X_{truncated}$ and we get B from the OLS approximation from eq. 3.10,

$$B = (\tilde{X}^T\tilde{X})^{-1}\tilde{X}^TY. \tag{3.13}$$

3.3.2.1 Circular-Symmetric PCR

The circular-symmetric version yet again only deviates from the real case by the substitution of Hermitian transpose instead of the normal transpose. By definition of the SVD, we have

$$X = U\Sigma V^H$$

and by truncating as we did in the real case, we use the OLS approximation from eq. 3.11,

$$B = (\tilde{X}^H\tilde{X})^{-1}\tilde{X}^HY. \tag{3.14}$$

3.3.2.2 Widely Linear PCR

We first note that from the SVD above, we get in the augmented form,

$$\begin{aligned}\underline{X} &= [X,\ X^*] = [U\Sigma V^H,\ U^*\Sigma^*V^T] \\ &= [U\Sigma, (U\Sigma)^*]\begin{bmatrix} V^H & 0 \\ 0 & V^T \end{bmatrix} \\ &= [T, T^*]\begin{bmatrix} V^H & 0 \\ 0 & V^T \end{bmatrix} = \underline{T}\begin{bmatrix} V & 0 \\ 0 & V^* \end{bmatrix}^H.\end{aligned}$$

Due to the non-uniqueness of the SVD, this is not necessarily equal to what the SVD applied directly to the augmented vector will provide. Thus, we reformulate from the SVD to the EVD, first noting that the augmented covariance matrix can be written as,

$$\underline{\Gamma} = \underline{X}^H\underline{X} = (X_{Re}T_m^H)^HX_{Re}T_m^H = T_mX_{Re}^TX_{Re}T_m^H = T_m\Gamma_{Re}T_m^H \tag{3.15}$$

where T_m is defined as in eq. 2.18. Following the standard eigenvalue decomposition procedure, we minimize the Rayleigh quotient (eq. E.1 in complex form) to find the eigenvectors V_{Re}. Thus, we wish to find the critical points of $V_{Re}^T \Gamma_{Re} V_{Re}$ subject to the constraint $V_{Re}^T V_{Re} = I$. We retrieve $\underline{V}$ from V_{Re} using eq. 3.15 in the the EVD (i.e. $\underline{V} = \frac{1}{2} T_m V_{Re} T_m^H$), noting that $\underline{V}$ is of the form

$$\underline{V} = \begin{bmatrix} V_1 & V_2^* \\ V_2 & V_1^* \end{bmatrix} \tag{3.16}$$

and project into the latent space by the widely linear transform,

$$T = XV_1 + X^* V_2,$$

and truncate both T, V_1 and V_2 and get $\tilde{T}$, $\tilde{V}_1$ and $\tilde{V}_2$. We note that V_1 and V_2 are orthogonal matrices, to both themselves and each other, enforcing the composite augmented matrix $\underline{V}$ also to be orthogonal. With $\underline{\tilde{V}}^H = \underline{\tilde{V}}^{-1}$, we thus get

$$\underline{\tilde{X}} = \underline{\tilde{T}} \underline{\tilde{V}}^H \tag{3.17}$$

in which we perform the widely linear OLS approximation eq. 3.12 with $\tilde{X}$ to retrieve B_1 and B_2.

3.3.3 Partial least squares (PLS) regression

The principle of PLS regression is almost the same as for PCR, although both X and Y is decomposed *jointly*. Following the same reasoning which leads to the kernel eigenvalue problem in eq. E.3, we use the EVD to find eigenvectors, T, which is the critical points of

$$T^T X X^T Y Y^T T$$

subject to $T^T T = I$. The eigenvectors, T, is a descriptor for both X and Y, and we can approximate the loading matrices P and C for X respectively Y using,

$$P = X^T T$$
$$C = Y^T T.$$

Both T, P and C is then truncated as with T and V before, to finally get $\tilde{T}$, $\tilde{P}$ and $\tilde{C}$ and the approximations,

$$\tilde{X} = \tilde{T} \tilde{P}^T \tag{3.18}$$
$$\tilde{Y} = \tilde{T} \tilde{C}^T \tag{3.19}$$
$$\tag{3.20}$$

and we use the OLS approximation of eq. 3.10 with $\tilde{X}$ and $\tilde{Y}$ to retrieve B.

3.3.3.1 Circular-Symmetric PLS

As before, the only change in the circular-symmetric PLS version is that the Hermitian transpose is used instead of the normal transpose. This holds true for the EVD as well.

3.3.3.2 Widely Linear PLS

The widely linear PLS version is a bit more complex than previous derivations. In (23), an attempt to derive the widely linear transform of the Nipals PLS algorithm was attempted. Unfortunately, the authors provide several mistakes regarding the augmented forms, both in the EVD but also in the loading projection steps. Nevertheless, the majority of the report is rigorously derived and provides a good reference. Additionally, if we wish to rewrite into the kernel version eq. E.3 (not accomplished in (23)), we wish to use the $\underline{X}\underline{X}^H$ and $\underline{Y}\underline{Y}^H$ form. We derive,

$$\underline{X}\underline{X}^H = X_{Re}T_m^H(X_{Re}T_m^H)^H = X_{Re}T_m^H T_m X_{Re}^T = X_{Re}X_{Re}^T \tag{3.21}$$

with similar results for $\underline{Y}$. Essentially this means that the latent matrix T has the property $\underline{T} = T_{Re}$. While the result is not surprising (since $XX^H \in \mathbb{R}^{N\times N}$ per definition), it is worrisome since we essentially lose the imaginary part.

Several implementations of widely linear PLS have been attempted, although we only provide the description of one here, and refer to appendix E for the others. While the other implementations offer a simple truncation of the matrices to perform the dimension reduction, the one proposed here uses an iterative method. The reason for this change lies in numerical stability. Additionally, we will not provide a kernel-based version and instead of using the EVD, we will use the SVD again.

Using the SVD, we extract the eigenvectors for $\underline{X}$ and $\underline{Y}$ by decomposing the cross-covariance matrix

$$\underline{X}^H\underline{Y} = \underline{W}\ \underline{\Sigma}\ \underline{C}^H, \tag{3.22}$$

and only keep the eigenvectors, $\underline{w}, \underline{c}$, corresponding to the highest eigenvalues, i.e., the first columns of $\underline{W}$ and $\underline{C}$. Following the next step as described in (17), we extract the inner representations (latent vectors) using,

$$t = \underline{X}\ \underline{w}, \quad \underline{t} = [t, t^*]$$
$$u = \underline{Y}\ \underline{c}, \quad \underline{u} = [u, u^*].$$

The loading matrices, $\underline{p}$ and $\underline{q}$, are then calculated by the widely linear OLS approximation eq. 3.12,

$$\underline{p} = ((\underline{t}^H\ \underline{t})^{-1}\underline{t}^H\ \underline{X})^H,$$
$$\underline{q} = ((\underline{u}^H\ \underline{u})^{-1}\underline{u}^H\ \underline{Y})^H,$$

and the matrices $\underline{X}$ and $\underline{Y}$ are projected (or so-called deflated) into the new space by

$$\underline{X} = \underline{X} - \underline{t}\ \underline{p},$$
$$\underline{Y} = \underline{Y} - \underline{u}\ \underline{q}.$$

Each vector $\underline{w}, \underline{c}, t, u, \underline{p}$, and $\underline{q}$ is stored as columns as matrices $\underline{W}, \underline{C}, T, U, \underline{P}$, respectively $\underline{Q}$ and the process is repeated from eq. 3.22 using the deflated matrices for the desired number of components.

3.3.4 Kernel extensions

The kernel-based version can quite easily be implemented for OLS, PCR, and the circular symmetric PLS simply by changing the $X^H X \to K_{XX}$ (for OLS, PCR, and PLS), and $Y^H Y \to K_{YY}$ (only for PLS).

4

Case I: Particle flow in pipe

The current chapter will provide an attempt at developing a fluid bed process monitor. The fundamentals of the project were first presented in the dissertations of Johan Nohlerts (5), and the aim is to examine and continue his work.

In the subsequent section, a brief introduction will be provided, followed by the specific aim of the project. In section 4.3 the analysis methods are discussed and related to the developed data analysis algorithms derived in chapter 3. Relevant parameters of the study are discussed, and the conducted experiments are presented. We finally present the results and conclude the chapter with a section containing a discussion of results and future work.

4.1 Introduction

Continuous flow chemistry in the pharmaceutical industry, where the aim is to produce desired chemicals continuously in tubes rather than in batches, has gained recent attraction (24). Possible benefits of continuous flow instead of e.g. the traditional batch stirred solutions, range from a more environmentally friendly production to product quality enhancements (24; 25). Typically, the process occurs in narrow channels where lower volumes can be used and better control of temperatures and other parameters can be obtained. Hence, improved control of selectivity, ratio, and mixing of chemicals can be used with carefully selected environmental parameters to enhance desired yield in chemical reactions (24; 25). In contrast, clogging in the channels may occur under certain circumstances, and is undesired as it will prevent or halt the flow within the channel. (24; 25) Thus, monitoring of the flow to determine the state - chemicals component ratios, humidity level, porosity, mass, volume, etc. - is desired to optimize compositions and chemical reactions as well as to detect anomalies early.

Prior work on flow monitoring using microwaves is exhaustive, and several working principles exist that can be implemented. Most versions can be truncated to microwave imaging using microwave tomography (26; 27), where several antennas are placed in a circle, or an E-probe which is inserted into the flow (28). Both methods offer quality analysis possibilities, but the tomography version is hard to implement and requires multiple transceivers and receivers to cooperate to function properly

(e.g. 12 antennas were used in (26)), and the E-probe only provides near-field information limited to one spot. Another method using cavity resonators only requiring one or two antennas was studied in (5), where a metallic cylinder was attached over a plastic pipe and two H-probes were attached to the inner walls of the cylinder. Using the resonant modes of the cylinder combined with hypothesis testing, they provided a method to detect anomalies in the system based on sampled spectrum.

4.2 Particle flow set-up and aim

In figure 4.1 the system used for simulating particles/granules flowing through a pipe is shown. As such, a plastic pipe is fastened in the middle of a metallic cylinder (used as the resonator), where the particles flow.

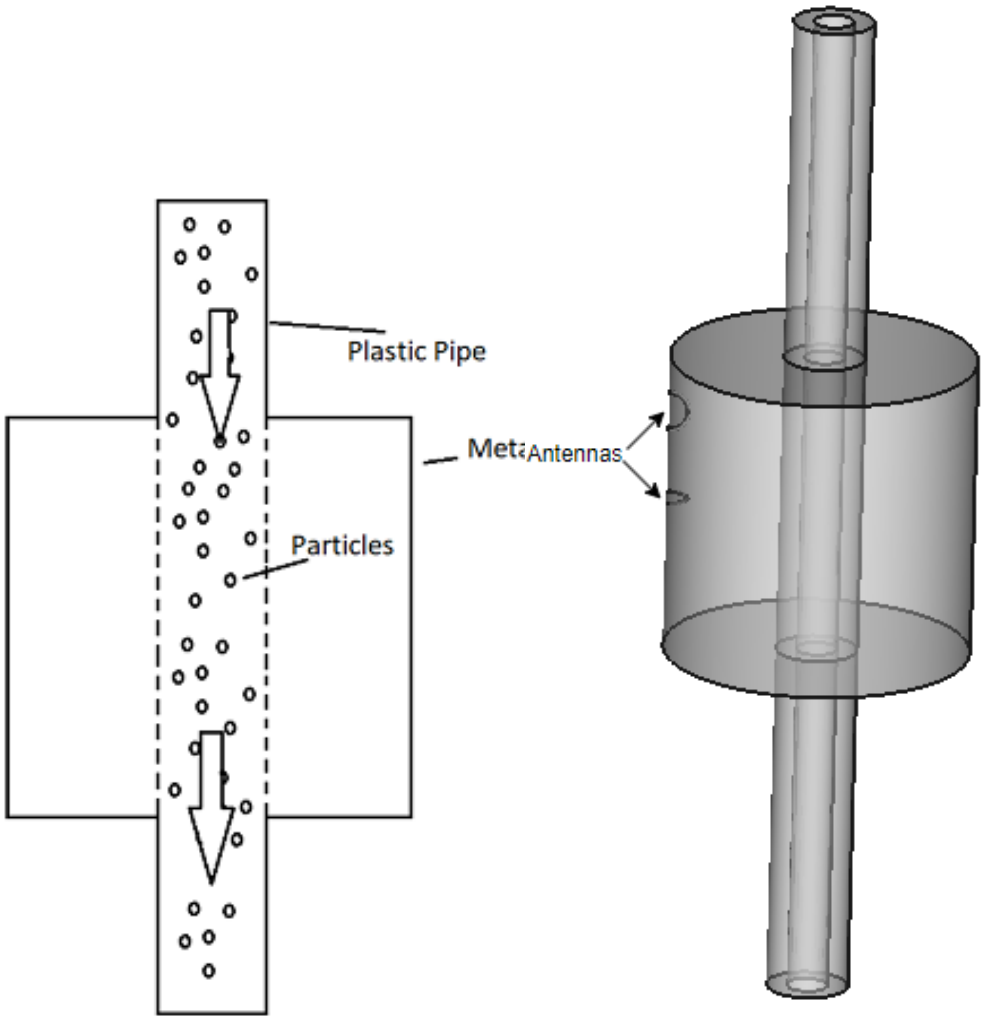

(a) Fluid bed dryer concept sketch.

(b) The simulated particle flow set-up used for the experiment. CAD model.

Figure 4.1: Simulated system of particle flow, sketch (a) and cad model (b). In (a) the flow of the granules may be seen.

The aim of the project is to review the possibilities of using the cavity resonator to monitor the flow in a plastic pipe. Instead of the hypothesis formulation used in (5), we will analyse the data using the regression methods derived in chapter 3, but also attempting to incorporate the physical interpretation models. We thus aim to investigate if different levels of density/porosity, humidity, and substances can be differentiated by the cavity resonator.

4.3 Method and design

The flow process was analysed using a VNA collecting samples from a frequency range of 1 - 5 GHz, where the antennas are found at the top right and middle left of the cavity walls. The number of frequencies collected was set to 500, and each spectrum will be represented at each time-point, t, using the L_1 norm between a reference spectrum and the current retrieved spectrum:

$$L_1(t) = ||\vec{x}(t) - \vec{x}_{ref}||_1 = \sum_n |x(n;t) - x_{ref}(n)|.$$

The L_1 norm was chosen as it reflects changes within the system. While other norms, such as the L_2 norm, would possibly follow more standard practices, the noise of the VNA may at resonant frequencies be larger than one, and thus the plot would be considerably fluctuating. The reference spectrum was retrieved from an empty cavity and as such for noiseless systems simply reduces to the sum of changes by the particles, $L_1(t) = \sum_n |dS_{21}MUT(s)|$. For simplicity, efficiency, and overall better representation the scatter parameter S_{21} was chosen.

Values representing the samples, Y, for regression were manually added. We note that this formulation may be insufficient for various problems, for instance in a continuous flow of substances where above y may be ill-defined. Thus, an improvement using the physical interpretations models in chapter 3 could be made. As such the Y matrix is loaded with values derived from the physics-related equations.

4.3.1 Experiments and data

Essentially, three experiments were conducted. The aim of the experiments was to determine the sensitivity of the monitor from various characterisation parameters of the samples falling through the pipe. Specifically, the size (experiment one), dielectric constant/change of material (experiment two), and porosity/density (experiment three) were examined. Before any experiment with pharmaceuticals in the form of tablets (paracetamol, MCC) was conducted, the tablets were exposed to room temperature and moisture for an hour.
In the first experiment, a tablet of paracetamol (500 mg) was dropped through the pipe 10-11 times while the monitor retrieved the spectra and then was cut in half before the experiment was repeated. The experiment was repeated twice.
In the second experiment, 0.5 ml sample holders were filled with one of several different materials (paracetamol, MCC, ethanol 95%, water (tap), water (distilled)), and as in experiment one dropped through the pipe multiple times. First, an empty

sample holder for comparison was dropped through the pipe for comparison.
Lastly, in experiment three, four 0.5 ml sample holders were filled with MCC powder. To increase the density, the sample in three holders where subjected to increasing pressure as more sample content was added. The weights of the samples in the holders were recorded to be 240, 260, 300, resp. 320 μg and the holders were then dropped as in experiments one and two repeated five times.

4.4 Results

We first provide a short section of numerical results, followed by a section containing an analysis of the process where the aim was to examine the process using the L_1 norm. Subsequently, we perform the data analysis described in chapter 3 and attempt at estimating Y given the retrieved spectrum.

4.4.1 Numerical results

Due to the then-current difficulties of meshing and receiving coincident nodes, the model was simplified to a cylinder where both solutions using Elmer and analytical solutions could be derived, and an example is provided in figure 4.2. Other numerical results using an antenna are presented in the chapter (in appendix) F, with full explanation and code.

4.4.2 Analysis of acquired data

From figure 4.3 we note that using the simple L_1 norm as a separator a clear change between 500 mg compared to 250 and 125 mg of paracetamol can be seen. The magnitude seems to have a higher difference in mean, but instead, the variance of the experiments seems to increase for larger particles. This presumably indicates that the unevenness of the sample passing through the pipe matters, as the smaller samples were much more uniform in shape. The error bars show a clear difference in amplitude, especially so for the magnitude, but also for the phase.

Similarly, in figure 4.4 we note that materials can be differentiated using the L_1 norm. Especially, we note that tap water and distilled water have different means with distilled water being slightly higher. This is to be expected since water molecules have a higher dielectric constant than impurities in the water. Lower dielectric samples, such as paracetamol and MCC, could also to some degree be differentiated.

Lastly, an increase in the L_1 norm for higher porosity samples was noted, where the results are shown in figure 4.5. Unfortunately, the variance between the experiments is high, resulting in overlapping intensities increases and difficulties in separating the obtained results using the simple L_1 norm. This though makes it an interesting case to analyse using regression.

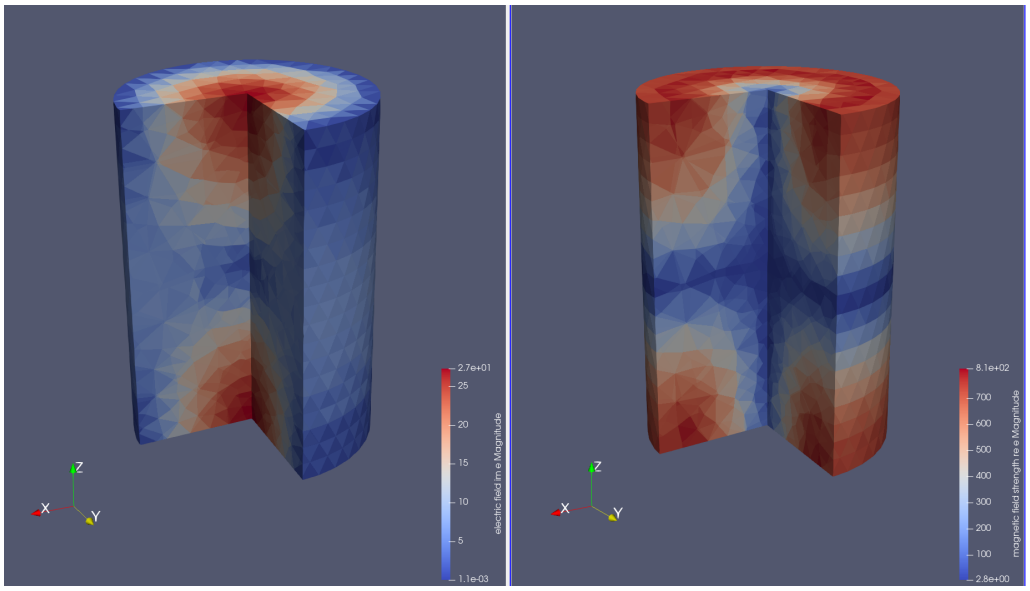

(a) Eigensolution with eigenfrequency 2.1GHz.

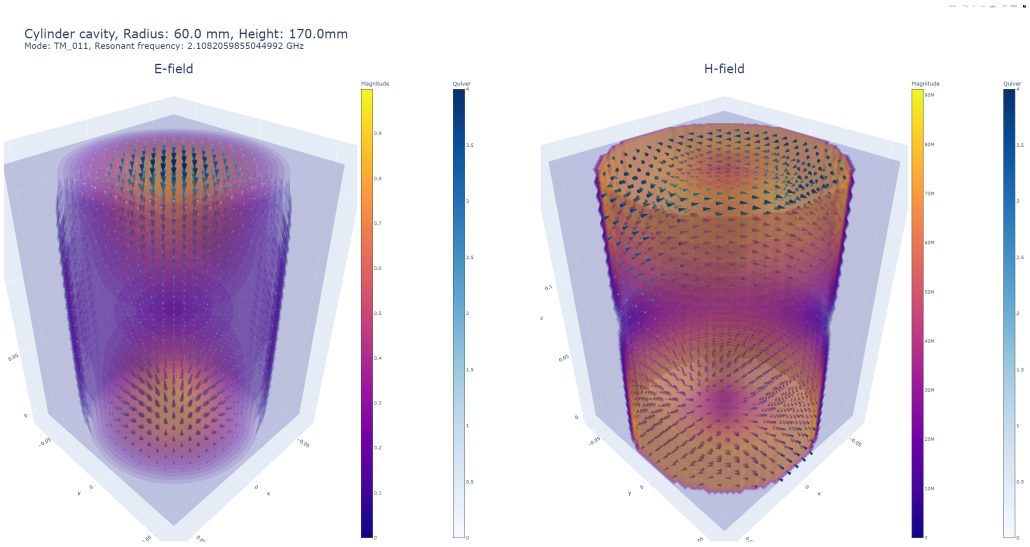

(b) Analytically derived fields for the TM_{011} mode.

Figure 4.2: Microwave simulated cavity with a radius of 60 mm, height of 170 mm, (a) Elmer simulation results and (b) analytical results.

4.4.3 Regression analysis of the acquired data

The dependent variable, Y, was set to the weights of the samples for experiments one and three, and the L_1 norm for experiment two. For experiment three, an effort was put into turning the *stochastic flow* method mentioned in section 4.3 using the simplified approach (assuming homogeneous material distribution), to derive porosity values from several resonant frequencies which then could be used for the dependent variable Y. The attempt failed and provided extremely off-values for the porosity (values of magnitude $\sim 10^6$) and as such results are omitted. Reasons for this could be plenty, where simple mistakes such as bugs in codes or more complex

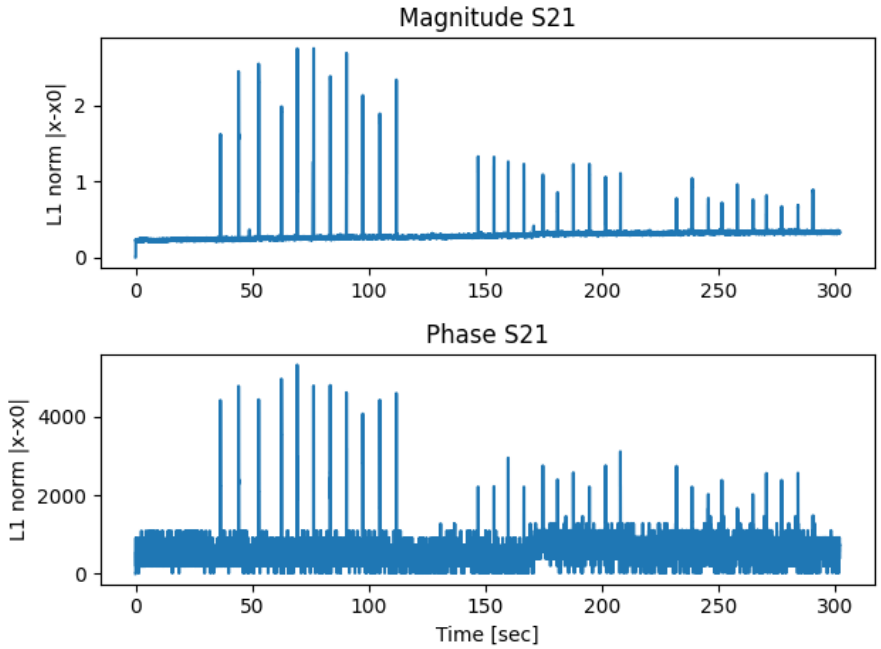

(a) Free falling paracetamol of in total four sizes (approximately weights: 125, 250, and 500 mg). The experiment for each weight was repeated 10-11 times.

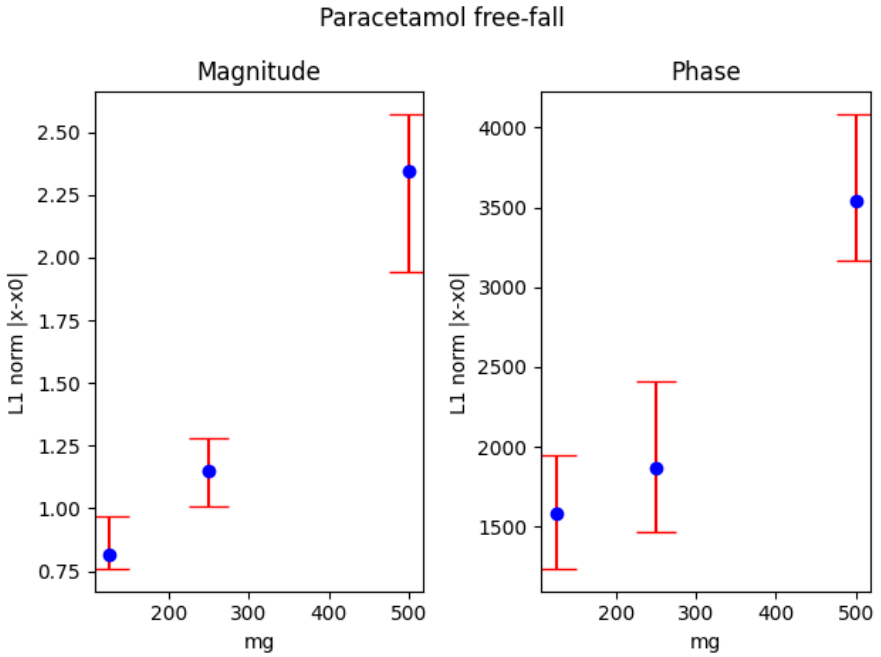

(b) Error bars of L_1 norm for each sample (peaks in previous plots). Max, min, and average (dot) shown.

Figure 4.3: Experiment one: Free fall of paracetamol. We note that samples with more mass were sampled first.

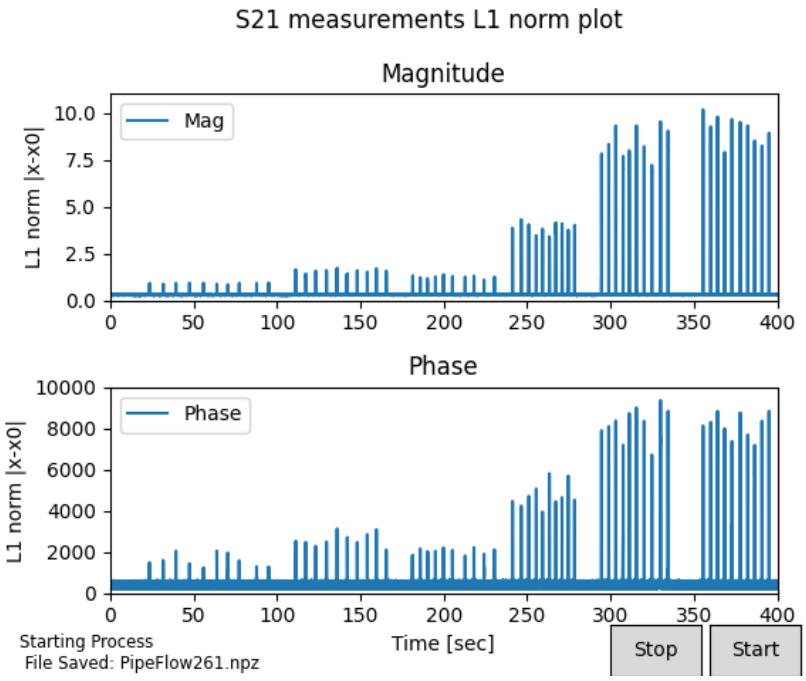

(a) Free falling sample holder (0.5 ml) with different samples (empty, paracetamol, MCC, ethanol 95 %, water, water distilled). The experiment for each sample was repeated 10 times.

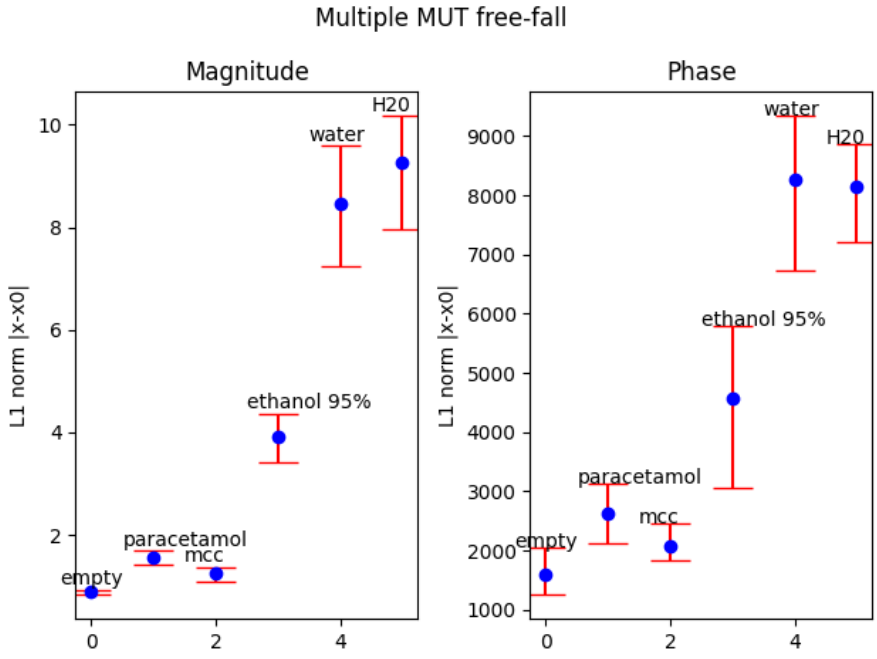

(b) Error bars of L_1 norm for each sample (peaks in previous plots). Max, min, and average (dot) shown.

Figure 4.4: Experiment two: Free fall of multiple samples.

issues such as invalid approximations could be at fault.

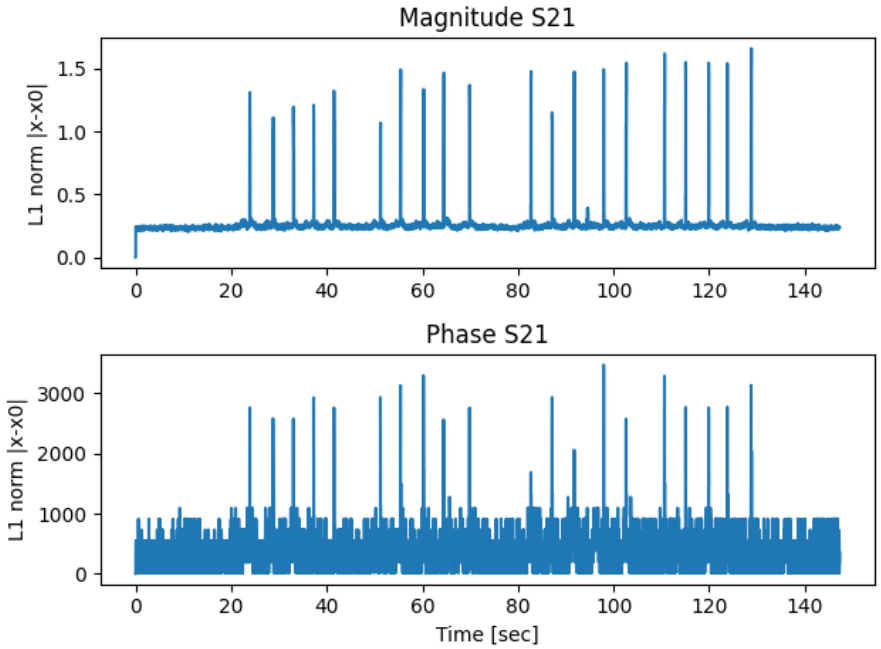

(a) Free falling sample holder (0.5 ml) completely filled with MCC of different densities (weights: 0.24, 0.26, 0.30, 0.32 gram). The experiment for each sample was repeated five times.

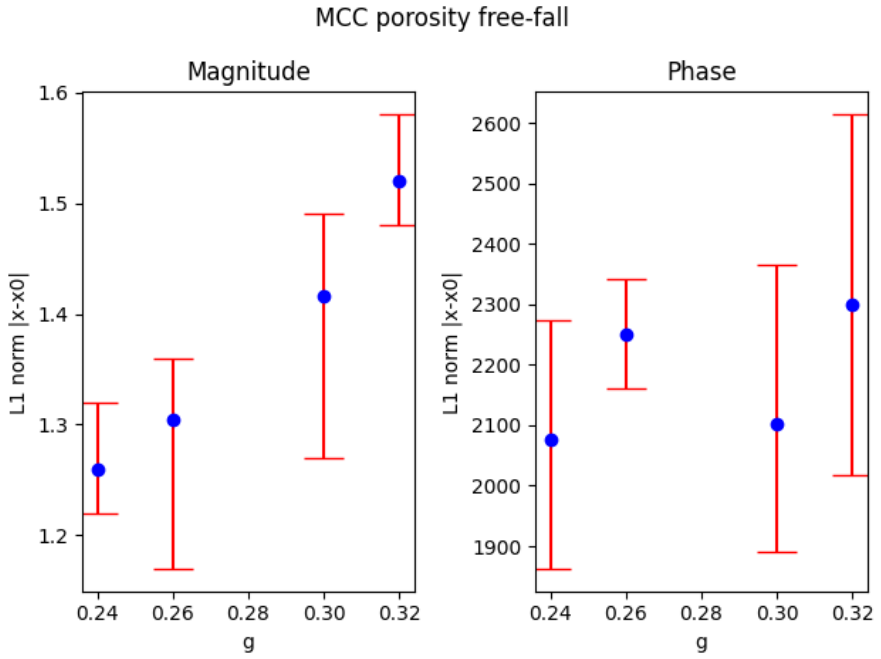

(b) Error bars of L_1 norm for each sample (peaks in previous plots). Max, min, and average (dot) shown.

Figure 4.5: Experiment three: Free fall of MCC of various densities occupying same space.

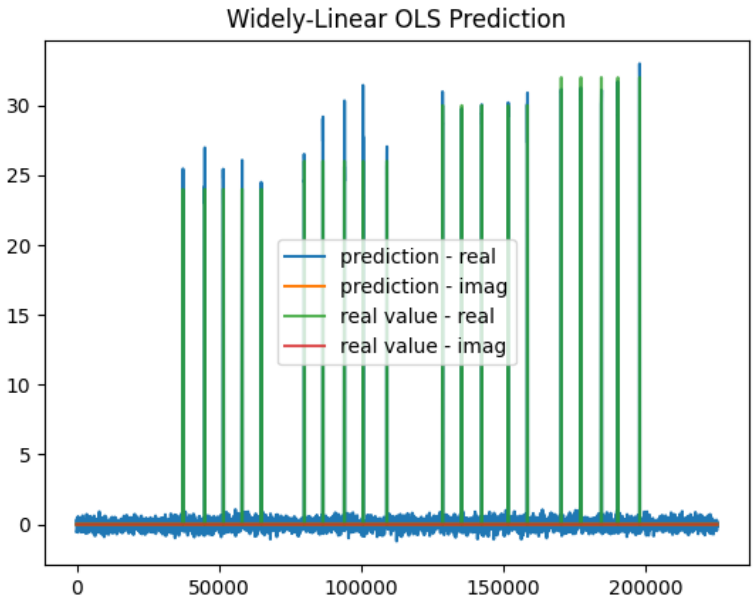

Figure 4.6: Experiment three: OLS predictions with real values.

	Exp. 1	Exp. 2	Exp. 3
CS OLS	0.93	0.93	0.94
CS PCR	0.87	0.89	0.88
CS PLS	0.93	0.93	0.91
WL OLS	0.96	0.97	0.98
WL PCR	0.89	0.90	0.87
WL PLS	0.90	0.90	0.87

Table 4.1: Mean (five runs) goodness of prediction / predictive power, Q2. Five components were used for PCR and PLS.

Prediction results of the three experiments is shown in table 4.1. We note that the OLS prediction typically provides the highest predictive power of the three and that the widely linear approximation more often decreased the predictive power. Still, the highest predictive score was attained with the widely linear OLS model. Only one prediction using the derived regression methodologies (chapter 3) is presented with figures, as most showed similar results and as such do not provide any interesting discussion point. The result is shown in figure 4.6. Typically, it seems that the prediction of non-zero dependent values is often over-estimated, which is a typical problem for all models. A quick analysis shows that the predictive power for only $Y > 0$ is below 0.5, indicating that most correct predictions are of $Y = 0$. A possible remedy is to make the dataset more balanced by removing the spectrum representing an empty cavity. By doing so an increase in predictive power for all was around 2 %.

4.5 Discussion

From the results of section 4.4.2, we note several parameters can be differentiated and characterised by the falling samples. Depending on the flow, the device should though quite easily notice clogging or high changes in density, mass, and moisture levels. For more specific information, both more experiments as well as more sophisticated models should be adapted as the current regression results have high uncertainty in the case of the desired values.

A possible way to improve predictions could be to adapt the physics-related methods presented in section 4.3, but as noted the simplified approach of the stochastic version failed. As such, one way to accommodate for the electric field inside the cavity is to add numerical results into the equation and assume the position of the sample using the first high rise of the L_1 norm and subsequently estimate the position with the gravitational constant, or by putting lasers at the top and bottom and interpolating. A slight attempt to realise this using the results attained from Elmer was initialised, but as it required too much effort timewise the attempt was concluded. Specifically, the models used in the Elmer simulations were heavily simplified due to the lack of understanding of the specific operations of the software.

4.6 Conclusion

An attempt at monitoring pharmaceuticals flowing through a pipe was conducted, and improvements in some areas as compared to previous works have been accomplished. What the current thesis though fails at was the incorporation of physical interpretation models into the analysis. Improvements to current results in the thesis have been proposed, and we note that what the project needs most of realistic, high quantity of experiments.

5

Case II: Fluidized bed dryer monitor

The current chapter aims at developing a fluid bed process monitor. The fundamentals of the project were first presented in the dissertations of Johan Nohlerts (5) and Lvivia Cerullo (6), and the aim is to examine and continue their work.

In the subsequent section, a brief introduction will be provided, followed by a description of the fluid bed process as a whole and the previous attempt at global monitoring by Nohlert and Lvivia. In section 5.2 the analysis methods are discussed and related to the developed data analysis algorithms derived in chapter 3. Relevant parameters of the study are discussed, and the conducted experiments are presented. We finally present the results and conclude the chapter with a section containing a discussion of the results and future work.

5.1 Introduction

Coating of pharmaceuticals using a fluid bed dryer is the process of encapsulating granules with a material to enhance the quality attributes of the finishing product. Qualities could be such as stability of an active pharmaceutical ingredient (29), granule hardness, dissolution behaviours, morphology, and mass uniformity of the coating (30; 31). High variability of coating material may lead to poor product quality and deviations in anticipated results during subsequent processing steps (31). As such, monitoring of the coating process may be seen as an important activity to ensure quality of the coated granules. While monitoring could be accomplished by extracting granules during the coating process (off-line monitoring), more desirable would be in-line, real-time monitoring during the process run. For instance, if the monitoring indicates abnormal process conditions, the process can be stopped while the issues are resolved, then the process could be continued.

Several attempts have been made to construct in-line, real-time monitoring devices for fluidized beds utilising microwave spectroscopy, including local monitoring using a novel ring-resonator (29; 31–33), local monitoring using tomographic sensors (34), but also global monitoring using magnetic field probes as sensors and the fluid bed dryer as cavity (5; 6). While the solutions provide different advantages and

disadvantages, global monitoring seems especially promising due to the possibility of extracting information from any part of the fluid bed, while only providing minimally invasive measurements. Process parameters such as flows and temperature, and also particle properties can be monitored to some degree. Such parameters appear to be less accessible for measurements using local monitor sensor approaches. On the other hand, global monitoring may fall short in the specificity of the characterisation of granules quality, where local monitoring should be better suited (31; 32).

In this work, global monitoring was chosen. As specified above, we found the work conducted by (5; 6) especially inspirational. Though, we also note other global monitor attempts for other types of processes, using different methodologies to accomplish comparable results (11; 12; 35).

5.1.1 Fluidized bed dryer and Spiritus - theory, and use

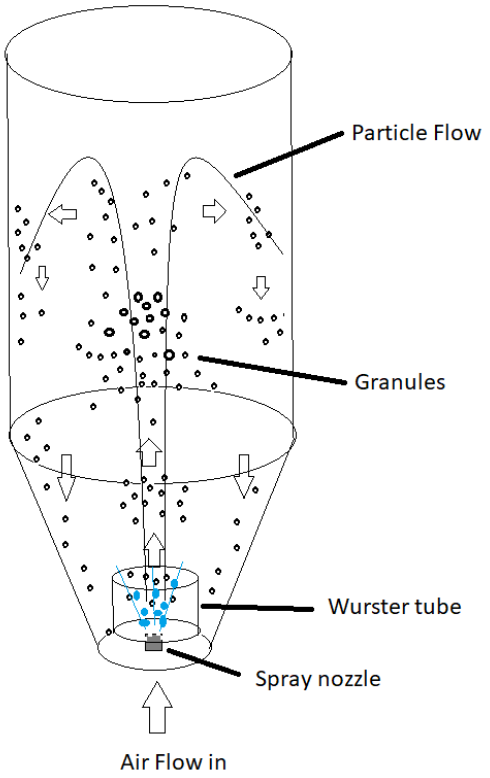

(a) Fluid bed dryer concept sketch.

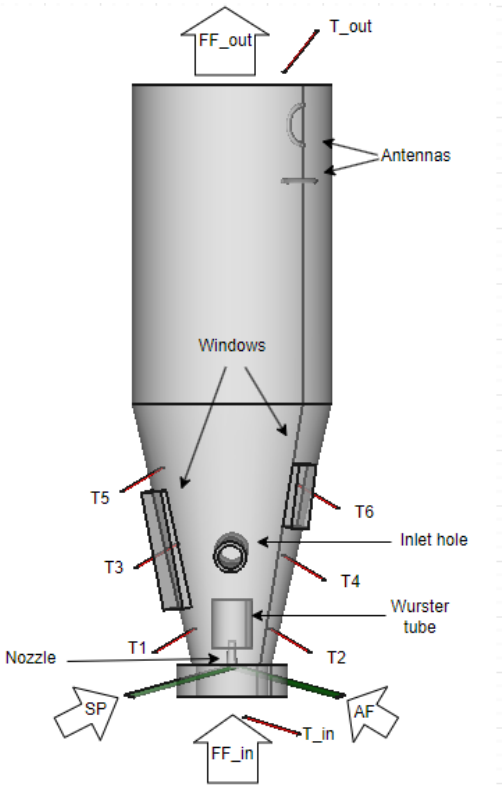

(b) The fluid bed used for experiments, Spiritus. CAD model.

Figure 5.1: Fluidized bed dryer device, sketch (a) and real (b). In (a) the flow of the granules, or particles as well as the coating process can be seen.

In figure 5.1 the fluidized bed dryer process is visualised, where in 5.1a) particles can be seen circulating in the cavity while being coated, and in figure5.1b) some details and labels of the used fluid bed (Spiritus) are shown. Three different in-flows can be considered in the process: fluidisation flow (FF), atomiser flow (AF), and liquid spray flow abbreviated (SP) alluding to the fact that a spray pump is used for this

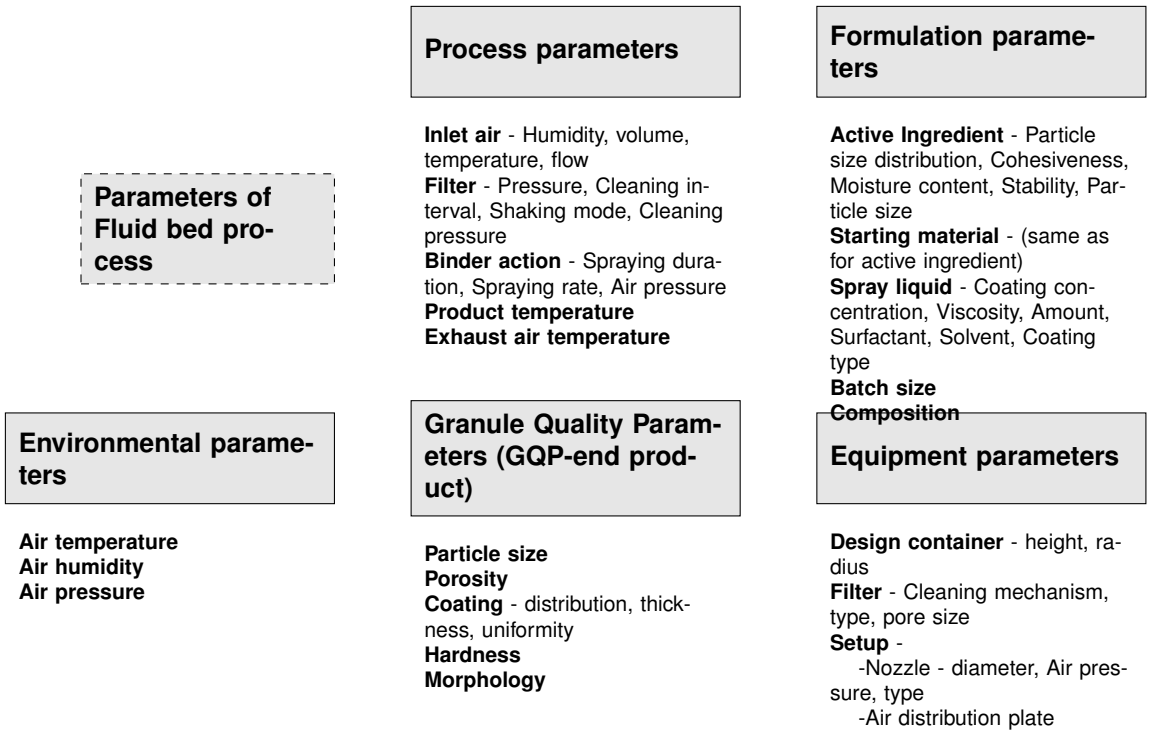

Figure 5.2: Parameters for quality management of the fluid bed process (36). Here the GQP defines the end product and suffices as a final quality check sample. The list is non-exhaustive.

flow. Each in-flow has four parameters that can be adjusted: temperature ($C°$), flow (Nm3/h), composition/humidity (g/m3), and volume (m3). Additional to the flows, there are a variety of parameters that can be altered and changed, ranging from granules/particles, spray liquid, and size of particle batches to nozzle diameter and filters. In figure 5.2 a list of parameters is shown, based on the dissertation of Johanna Peters (36). In the current thesis, we will mostly consider only variations of the flows and fix the other parameters for simplicity.

A brief description of the process is provided, where labels and names used are illustrated in figure 5.1b). Both FF flow and AF flow causes the particles/granules to elevate from the bottom of the cavity, but as is important to note, inherently different. The FF makes the particles slightly elevate around, but not much higher than, the Wurster tube. The AF flow on the other hand forces the particles to flow through the Wurster tube and continue high up in the fluid bed, to then fall along the walls effectively creating a 'fountain'. The higher the flow of AF is, the higher the granules will reach. Typical values of FF used in the current thesis were 20-60 Nm3/h and for AF 2-9 Nm3/h. The FF is typically heated prior to entering the cavity (measured as T_{in}), which results in the drying effect of the fluid bed, and typically used set values of the temperature in the thesis were 30-60 $C°$. The fluid bed is heated only with the FF flow set as > 0 since the heat will otherwise not be transported into the cavity. After pre-heating the cavity, and after elevating the particles using both FF and AF, the SP is activated. with A typically set spray flow

in this thesis was 9-16 g/min, depending on the desired outcome. Increasing the SP flow increases the risk of system collapse, which is also of interest to study as it is inherently undesired, and methods to detect and prevent such is thus desired. The SP contains the liquid sprayed onto the particles. For a normal spray coating process, the coating material is dissolved in this liquid, which then will coat the granules. This liquid flows together with the AF into the nozzle prior to the cavity.

During the process, the coating of granules normally binds either by hardening due to evaporation of the sprayed liquid during the drying phase. Additionally, granules collide and may aggregate when sprayed; aggregation which also may break and split during the process. If the moisture level of both granules and the environment is inadequate, or the airflow or the drying is insufficient, undesired aggregation may arise (36). The process, as seen in figure 5.2, contains a multi-complex, multi-decision problem with several parameters to consider. Each parameter is tightly interlinked with several other parameters and affects the end product. In our case, where microwaves are intended to be used to monitor the process, environmental-, process- as well as formulation parameters may affect the quality and preciseness of the measurements.

Spiritus is one of the fluid bed dryer equipment which was available for use for the experiments. The construction of Spiritus is different from other fluid beds as it contains six additional temperature measurement sticks inside the cavity. An illustrative CAD (Computer Aided Design) model of Spiritus is shown in figure 5.1b) where the additional temperature sticks are T1-T6 as shown in the images. Two more temperatures are measured, the inlet flow and the outlet flow. Two windows on Spiritus can be shown, which were used to fundamentally understand the coating process before sampling from the VNA. Prior to conducting the microwave measurements, the windows were sealed using aluminum foil to prevent both microwaves from leaking out, and also to block signals from the outside which may affect measurements. At the top right of Spiritus two antennas/H-probes were attached.

In the following text, we will refer to the FF flow (Nm3/h) as simply FF, AF flow as AF (Nm3/h), the temperature of FF as T_{in}, and the humidity of the SP flow as SP (g/min).

5.1.2 Problem statement and previous work

In the global monitor method, we may extract two types of information, 1) process parameter information and 2) particle positional and characterisation information. Of the two, the latter is of more interest. As such the aim is to derive as detailed information of the particles/granules in the fluid bed as possible while avoiding affecting the process. The most extensive work found on global monitoring of a fluid bed can be found in Johan Nohlerts (5) and Lvivia Cerullo (6) dissertations, where two magnetic probes/antennas were attached to a metallic wall like what is shown in figure 1.1. At the other end of the antennas, a VNA was connected, and the system was scanned over a 1 GHz range of frequencies (0.8- 1.8 GHz). In the dissertations, they divided the inner space of the fluid bed into three sub-regions and attempted

at finding the shift in the dielectric permittivity of the resonance frequencies as a means to monitor the state of the process in each region. Ridge regression was used with a priori estimate as described in chapter 3, assuming the relationship between the data and the process parameters could be described and approximated using circular-symmetric models. Unfortunately, performing the statistical test presented in section 2.4.3, the collected spectra are not circular-symmetric.

The methods used in the dissertations, similar to the derived method in chapter 3, both require a good priori estimation within the ridge regression method. Deviations in the estimation will cause the methods to miss-fit all further predictions. Thus, if either method is used, or any other which aims at separating the particle and parameter contribution to spectrum changes, there is a need for a well-adapted estimation model. In the previous dissertations, the focus on this issue was limited, and the authors only hinted that the model could be improved. An improvement could thus be to extend the current models using the so-called widely linear transform, effectively accounting for improper complex signals.

Another problem of Nohlert and Lvivia's work is the collection of raw data. As interpreted by reading their dissertations, they sampled a single spectrum for two seconds prior to approximately eight seconds of transferring the data from the device. The sample speed of such should be considered way too slow, and much valuable information would be missed. Furthermore, the velocity of particles within the cavity moves at a higher pace than the spectrum sampled, which means one spectrum does not reflect the one-and-same position of observed particles. Thus, in this work, the sampling speed during the spectral acquisition was increased, and the analysis and sampling process was constructed to be parallel to not stop the data acquisition. Details of the data acquisition can be found in appendix D.3. The latter issue was initially studied in a simplified process setup. While differences in spectral responses between sampling speeds can be seen, it was difficult to determine the extent of the problem in the simple setup used.

5.2 Methods and data analysis

The fluid bed was analysed using the VNA collecting samples from the whole possible spectrum (0.1 GHz - 26.5 GHz), where the antennas are found at the top right of the cavity walls to avoid being affected by for instance FF and particles as much as possible. Each spectrum contained 20 000 samples/scatter parameter for each time point, and was represented at each time-point t using the L_1 norm between a reference spectrum and the current retrieved spectrum:

$$L_1(t) = ||\vec{x}(t) - \vec{x}_{ref}||_1 = \sum_n |x(n;t) - x_{ref}(n)|.$$

Again, the L_1 norm was chosen as it reflects changes within the system and we have $L_1(t) = \sum_n |dS_{21}^{Environment} + dS_{21}^{MUT(s)}|$ for noiseless systems. Again, S_{21} was chosen and will henceforth be referenced as simply X.

The fluid bed process parameters were measured using data acquisition (DAQ)

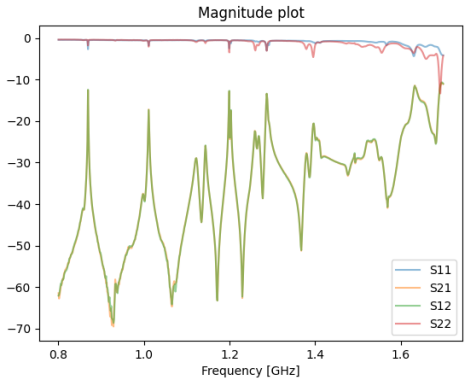

(a) Subset of the full spectrum. Here 0.8-1.8 GHz is shown.

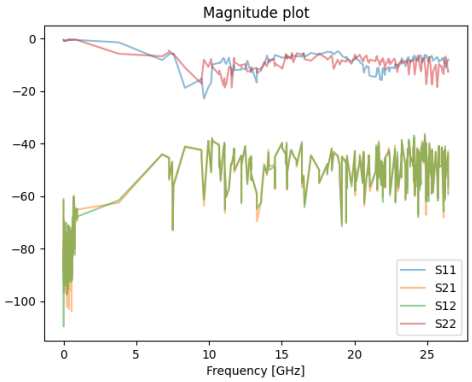

(b) Subset of the full spectrum. Here frequencies with variance > 50 for the first experiment are shown.

Figure 5.3: Studied subsets in the thesis. Only the magnitude of the data is shown.

boards, and the parameters of interest are discussed in the next section. We will first provide an analysis of the data by comparing the L_1 norm with the corresponding process data, to determine how environmental changes (e.g., increased temperature) affects the measured frequency spectrum. This will provide essential information in regard to the subsequent analysis, where we attempt at estimating both the fluid bed parameters from the spectra, and also the spectra from the fluid bed parameters, previously described in detail in chapter 3. Since the spectra were too large to process at the same time, subsets of the data along the frequency axis were extracted and used for regression. Two different subsets were considered and studied separately: the first subset was essentially the same as the one studied by Nohlert and Lvivia, in the range 0.8-1.8 GHz (where they studied 0.7-1.7 GHz). The other subset was extracted by considering the variance in each frequency, and a frequency was kept if the variance was above fifty, where fifty was arbitrarily chosen. While the first subset was chosen to reproduce previous results, the second was used as a representative of the whole spectrum due to most frequencies are non-resonant frequencies and thus do not vary much. The two subsets are shown in figure 5.3, and we will henceforth refer to them as *interval subset* for the subset used by Nohlert and Lvivia, and *variance subset* for the other.

Additional to the experiments and data analysis, we also provide numerical results using the open-source multi-physics software Elmer, where previous work relied on commercial software such as COMSOL. The results are presented in section 5.3.1

5.2.1 Parameters under study

The aim of the experiments was to investigate the possibility to monitor a fluid bed process with circulating particles sprayed with a liquid. Microcrystalline cellulose (MCC) particles were chosen as those are commonly used in this process. The spraying liquid was chosen as distilled water (H20). This is a simplification compared to a

Experiment	Parameter(s) studied	Used Material	Process Time[min]
Blank run	None	None	10
Sensitivity	None	None	3
MUT put in	MUT	MCC	10
1	FF_{in}	None	5
2	AF	None	5
3	T_{in}	None	5
4	FF+T_{in}	None	5
5	FF+AF+T_{in}	None	15
6	SP+FF	None	10
7	SP+FF+AF+T_{in}	None	15
8	FF	MCC	5
9	AF	MCC	5
10	FF+AF	MCC	5
11	FF+T_{in}	MCC	10
12	SP+FF+AF+T_{in}	MCC	30

AF = Atomizer flow [Nm3/h]
FF = fluidisation flow [Nm3/h]
T_{in} = temperature T_{in} [C]
SP = humidification [g/min]
MUT = material under test

Table 5.1: Conducted fluid bed dryer experiments.

full process that would involve a liquid such as ethanol with a dissolved or dispersed coating material. Additionally, we simplify the problem by assuming constant values for some process parameters. These assumptions, as understood when instructed on how to use Spiritus, are typically standard practices. For the fluidisation flow, we assume both dry air and constant volume and only change the flow rate and temperature. For the atomiser, we set all but the flow rate to a constant value, and again chose dry air. Lastly, for the liquid spray flow, only the humidity is changed. This restricts us to only four parameters to study, FF (flow), T_{in}, AF (flow), and SP (humidity). A subset of conducted experiments is shown in table 5.1.

5.3 Results

Attained results for Case II in the thesis are presented here. We first provide a short section of numerical results, followed by a section containing analysis of the process where the aim of the second mentioned section is to examine the process and determine the difficulties of the current set-up. Subsequently, we perform the data analysis described in chapter 3 and attempt at estimating both the parameters of the fluid bed (FF, AF etc.), labelled Θ, but also attempt at estimating the spectrum, labelled X, given the fluid bed parameters.

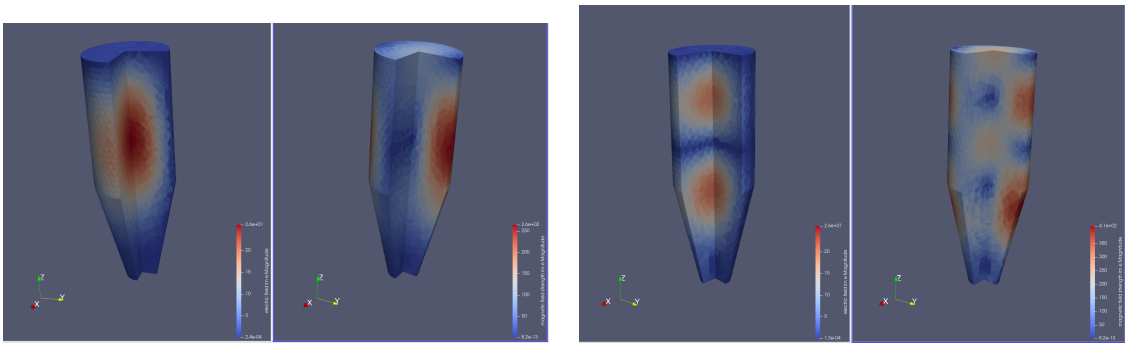

(a) Eigenfrequency ∼0.71GHz **(b)** Eigenfrequency ∼0.90GHz

Figure 5.4: Eigenvalue solution of the fluid bed with the corresponding eigenfrequency.

5.3.1 Numerical results

Numerical results from electromagnetic modelling of the fluid bed using the open-source multi-physics software Elmer was attained. In referred work, numerical results were attained by the commercial tool COMSOL (see (5; 6)), and by means of visual comparison, the results were equal. An example of solving the eigenvalue problem can be seen in figure 5.4 where two such solutions are shown. Additional to solving the eigenvalue problem, an antenna similar to the H-probe was added to the model at the top of the fluid bed, and excited microwaves into the system. For specified excitation frequencies chosen close to a resonant frequency, the results provided comparable results as to the eigenproblem solution as should be expected. Thus, we provided an additional approach to analysing the fluid bed which resembles the real system more than the eigenvalue problem. Another advantage of using the antenna model is that we may calculate the frequency spectrum, as the one attained by the VNA in the real experiments, while the eigen solutions only provide discrete values of the frequency spectrum. A disadvantage is the simulation time, which is several hours longer than the eigenvalue solutions. A longer description of what has been accomplished, as well as with more results is provided in the appendix F.

5.3.2 Analysis of acquired data

Firstly, we consider the sensitivity of the fluid bed towards outward interactions. In figure 5.5 the results from a blank run and a sensitivity experiment are shown. The blank run is especially noteworthy (figure 5.5a)) since neither are any particles in the system, nor are any parameters altered, nor is the fluid bed interacted with. Even so, the L_1 norm rose with time. A first guess was that the air extractor coupled to the top of the fluid bed was too strong and as such affected the antennas or filter at the top. The strength of the extractor was lowered and indeed the problem was mitigated. In figure 5.5b) the effect of some arbitrary sensitivity tests such as moving the fluid bed or moving the VNA is shown. The idea was to investigate how possible normal occurrences and operation of the fluid bed can affect the measurements as if some actions permanently change the system, this could lead to very unexpected and hard-to-interpret results in subsequent analysis. From the results, we note

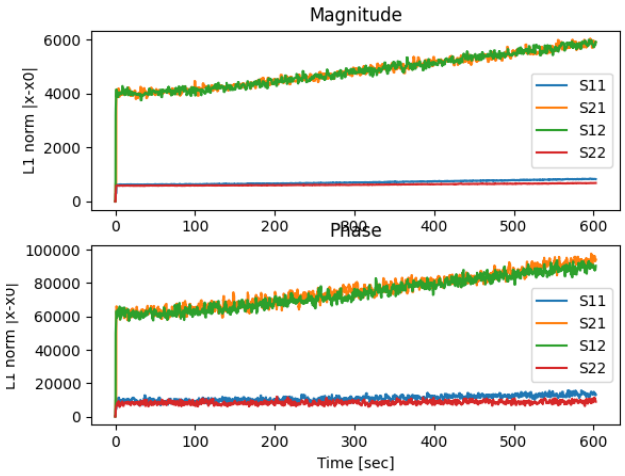

(a) L_1 norm of the spectrum, magnitude (upper) and phase (lower) for all scatter parameters. The blank experiment with an empty cavity and no changes to the environmental parameters.

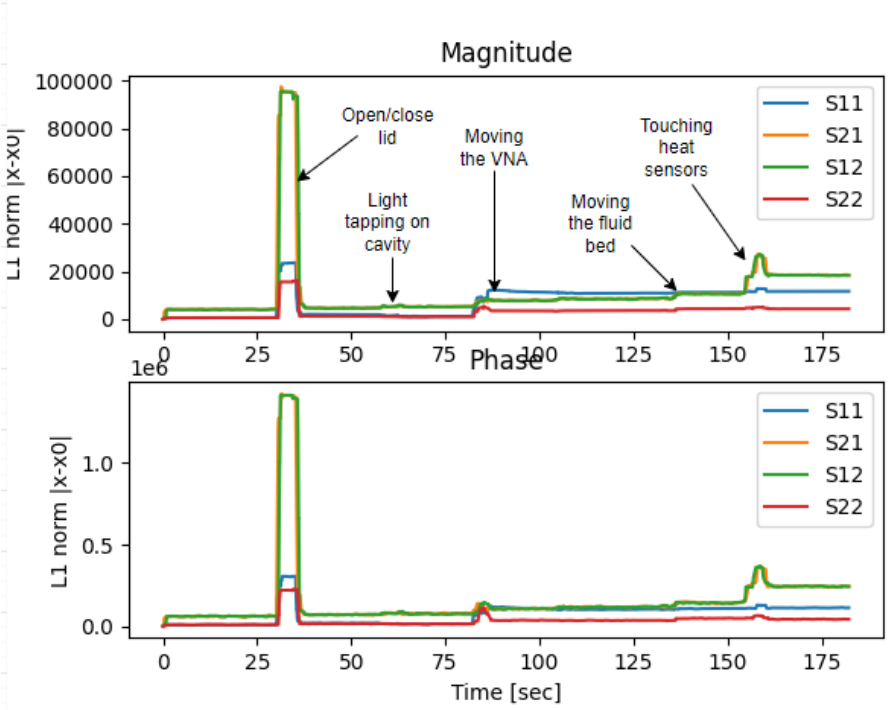

(b) L_1 norm of the spectrum, magnitude (upper) and phase (lower) for all scatter parameters. The sensitivity experiment with an empty cavity and no changes to the environmental parameters.

Figure 5.5: Sensitivity analysis of the fluid bed and the VNA measurements.

that opening and closing the lid and touching and tapping the cavity causes little to no permanent changes. On the other hand, moving or altering the position of the VNA and fluid bed caused permanent changes to the measurements. The first

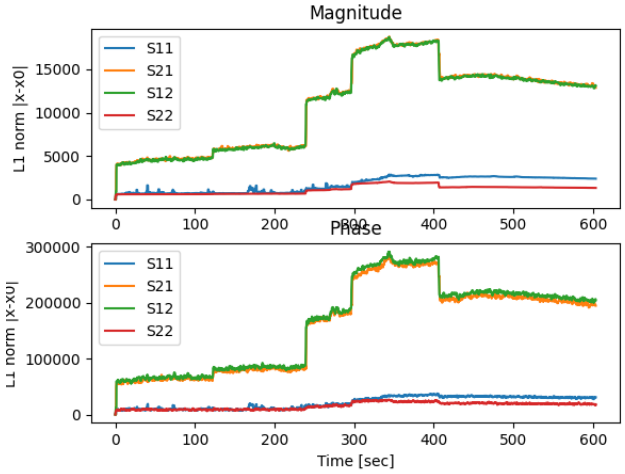

(a) L_1 norm of the spectrum, magnitude (upper) and phase (lower) for all scatter parameters.

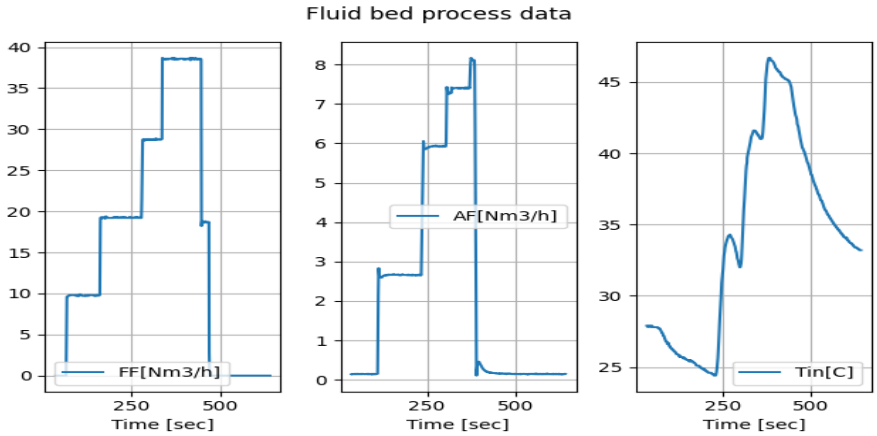

(b) Process data for the fluidisation data. From the left: FF, AF, and T_{in}. (y-axis from left: Nm3/h, Nm3/h, C^o)

Figure 5.6: Results from the fifth experiment, were FF, AF, and T_{in} were altered. Here an empty fluid bed is studied.

mentioned is mostly due to the coaxial cable position from the VNA to the fluid bed, which optimally should be the same. This is unwanted behaviour since fluid beds are regularly dissembled for cleaning etc., in which the VNA is detached and later re-attached again for other experiments. The latter issue is due to outward disturbances, and shielding the cables mitigated the problem. For Spiritus, the extra heat sensors (T1-T6) are typically quite loosely attached, and touching and moving them slightly caused significant changes to the spectrum.

Secondly, consider figure 5.6 where the L_1 norm is compared to the corresponding fluid bed parameters (FF, AF and T_{in}) which were altered during the experiment. Since the cavity was empty during the experiment, the changes in the spectrum shown by the L_1 norm are purely a result of changes in the fluid bed environment. As seen from the figure, several challenges, but also possibilities of the system can

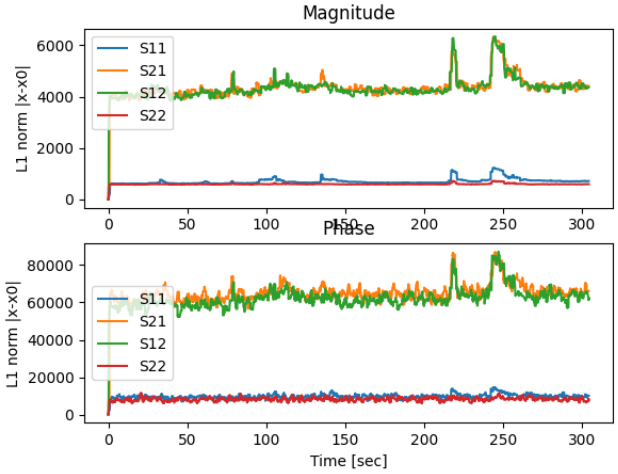

(a) L_1 norm of the spectrum, magnitude (upper) and phase (lower) for all scatter parameters.

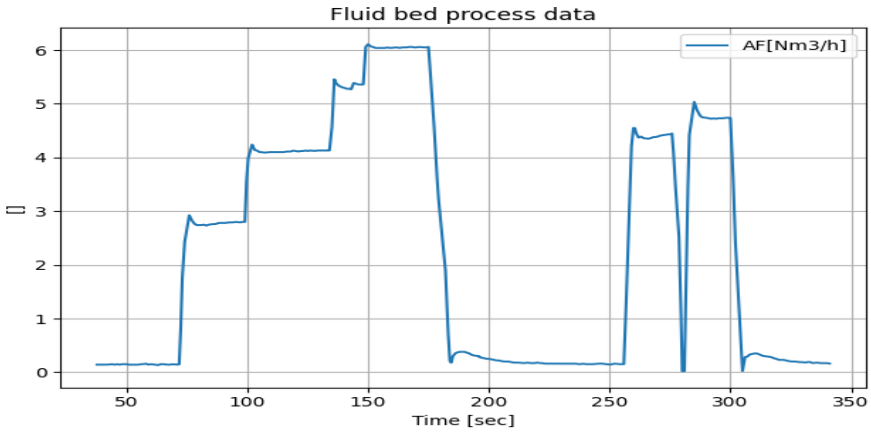

(b) Process data for the fluidisation data (y-axis: Nm3/h)

Figure 5.7: Results of the second experiment where the AF parameter was altered. Here an empty fluid bed is studied. The y-axis label is shown as a legend in the plot.

already be noted. We first present the challenges:
We observe that most drastic changes of the L_1 norm coincide with the FF parameter, except for the first and last changes of the parameter which the norm could not detect. While the other parameters AF and T_{in}, had a much smaller impact. The changes which the monitor measures, occurring in the L_1 norm at time point $\sim 125, 240, 300$ and 400 seconds, are not linear and seem to produce a higher effect for increasing flow strength. An explanation for this could be that the airflow effect the cavity and/or the antennas, for instance by altering the position or shape which in return is what the antennas measure. This explanation is strengthened by the fact that lower values of the flow have in general lesser effect on the measurements, due to possessing inadequate strength to move or reshape the cavity or antennas. Similarly, too high flow could cause permanent changes which would result in the

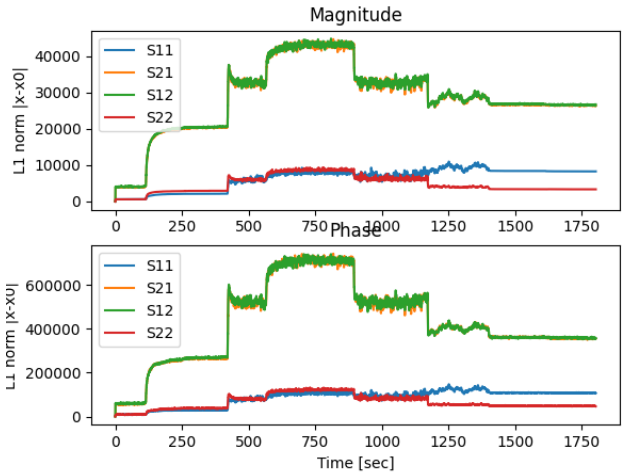

(a) L_1 norm of the spectrum, magnitude (upper), and phase (lower) for all scatter parameters.

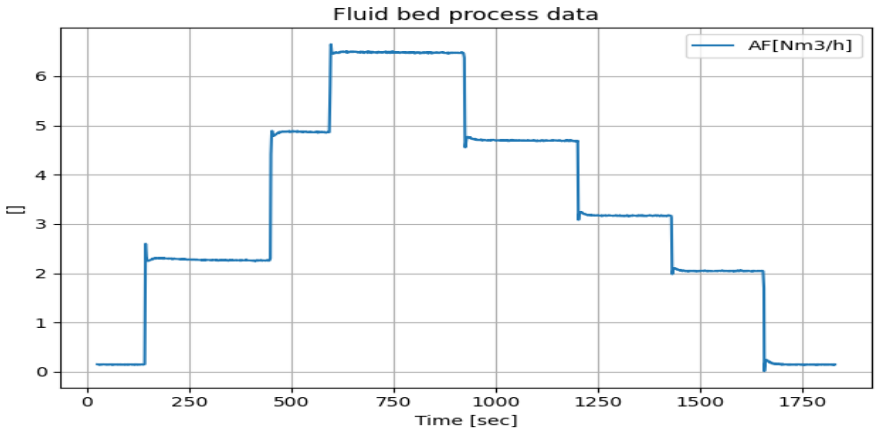

(b) Process data for the fluidisation data (y-axis: Nm3/h)

Figure 5.8: Results of the second experiment where the AF parameter was altered. Prior to the experiment, the fluid bed was partially filled with MCC.

L_1 norm being unable to return to the previous state even when the flow is again lowered, which could explain why no drop was recorded at the end of the experiment.
For T_{in} only a fast drop was recorded after 400 seconds while the temperature had a much slower decrease rate, which suggests that temperature does not have a quick direct effect on the measurements. For AF, we consider figure 5.7. While it is possible to notice some effects on the L_1 norm by the AF, we 1) note that the effect was less sustained compared to the AF, 2) the scale of change where the effect of AF is about 30 times lower than that of FF in figure 5.6, and finally 3) the effect is not much larger than the accumulated noise (the first step on the far left). We also note that the state of L_1 returns to the original state after the change, suggesting no permanent effect has occurred.
From these observations, we may assume that as of the current state, reproducibility

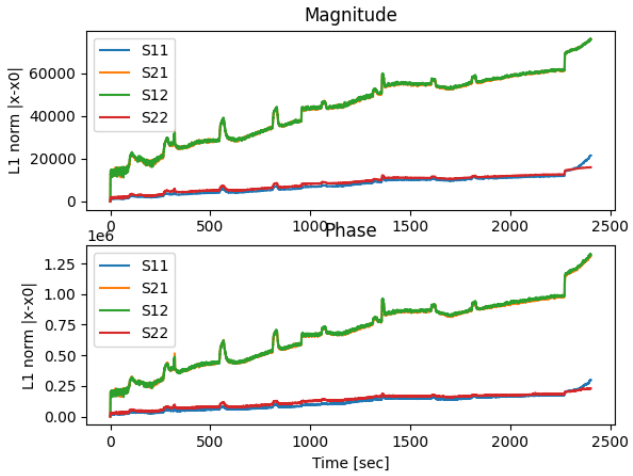

(a) L_1 norm of the spectrum, magnitude (upper), and phase (lower) for all scatter parameters.

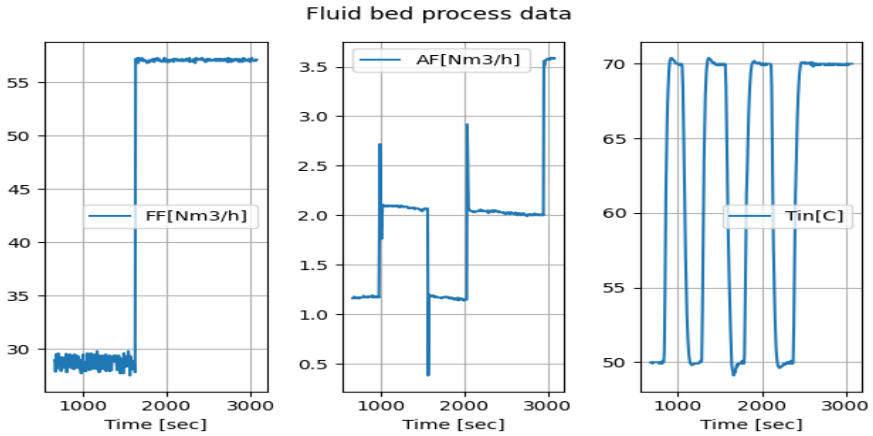

(b) Process data for the fluidisation data. From the left: FF (y-axis: Nm3/h), AF (y-axis: Nm3/h), Tin (y-axis: C)

Figure 5.9: Results of the 12th experiment, where FF, AF, T_{in} and SP were tested. Prior to the experiment, the fluid bed was partially filled with MCC.

may be an issue and the main cause lies in the FF parameter. Quick attempts to strengthen parts that may be affected by the FF flow, such as metallic filters at the bottom of the fluid bed, were attempted but ultimately did not yield sufficient improvements. On the positive side, the changes of L_1 show that it is plausible to estimate parameters from the spectra, and also plausible to estimate spectra from parameters.

Next, let us consider both figure 5.7, presenting the results from only increasing and decreasing the AF parameter with an empty cylinder, and 5.8 for the same experiment but this time with MCC present inside the cavity. As observed, almost no changes could be seen by the AF without particles in figure 5.7, but with the addition of particles, the change is several times higher (up to ten times). The cause is of course the movement of the particles inside the cavity, which when the

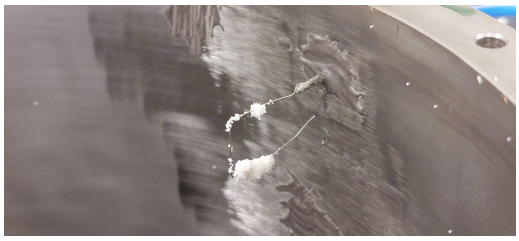

(a) Particles (MCC) stuck on the antenna due to static charges of the particles.

(b) System collapse due to too humidified atmosphere in the fluid bed.

Figure 5.10: Two observed issues; in a) particles stuck on the antenna and in b) system collapse.

AF is increased forces the particles to go up through the Wurster tube and then fall along the walls, thus creating the 'fountain'. Thus experiments two and nine combined provide a special interesting case of study using the data analysis discussed in chapter 3. Furthermore, we note by comparing figure 5.6 and 5.8 that for higher AF values, the L_1 norm fluctuates more when particles are presented in the system compared to when they are not. The first guess as to why, is again the movement of particles. This guess is strengthened by the results gained from experiment twelve, see figure 5.9. We note that when the spray nozzle is turned on (with limited flow $\sim$ 9 g/min), the fluctuations are temporarily smaller only to return shortly after. If the spray is instead turned on with a high flow, e.g., $\sim$ 16 g/min, the L_1 norm is again steady. This is due to the occurrence of a so-called system collapse, in which the MCC particles clog together next to, or on the nozzle. In figure 5.10b) a failed coating experiment is shown, in which the clog is formed, and the AF flow is disturbed.

In figure 5.9 another issue is displayed; the L_1 norm is constantly increasing even if the parameters are altered as before. The cause of this is shown in figure 5.10a), where particles attach to one of the antennas due to static charges of the particles. The issue reinforces the choice of the H-probe instead of the E-probe to avoid static voltages from the particles into the VNA.

Lastly, the temperature distribution within the fluid bed was recorded to change when particles were introduced. Similar observations of the phenomena can be found in (37). The effect is unknown, but using similar reasoning the FF and AF could also be affected.

5.3.3 Regression analysis of the fluid bed data

Essentially we make two different regressions, wherein the first we estimate the process parameter Θ using the spectrum X by

$$\Theta = XB_\Theta \qquad \textit{estimation of } \Theta$$

In the second we instead attempt at estimating the spectrum X using the process parameters Θ by,

$$X = \Theta B_X \qquad \textit{estimation of } X$$

As such we wish to determine B_X and B_Θ using the regression methods we derived in chapter 3. In the first experiment, we avoid inverses of approximated B's, as quick tests indicated worse performance. For both regressions, the effect of how many parameters Θ contains is studied, in which one, two, and nine are tested. We chose for simplicity the number of regression components of PCR and PLS to be five, where five was chosen by some initial tests and typically provided good regression results. Additionally, before considering the regression analysis a general result of the difference between circular-symmetric and widely linear regressions is presented.

Each regression was performed on the data from a single experiment, as the data size was too big for combining from multiple experiments. Each such dataset was split into two sets: a training set, X_{train}, with 80% of all spectra (randomly sampled), and a validation set, X_{val}, of the remaining 20%. The models were as such trained on the training set, and a prediction was later made using the validation set. The predictive power, Q_2, was calculated using equation 3.9 on the predictions. To get a better estimation of the overall quality of the models, the predictive power was cross-validated on different subsets of the data. As such the Q_2 value was calculated 10 times by re-sampling X_{train} and X_{val}, and the fitting and predictions were made on the new selection of data. The mean of the Q_2's values was then used to compare the models.

Only the predictions of the variance subset will be added for the estimation of Θ, $\Theta = XB_\Theta$. The motivation is that the prediction of almost all models gave low Q_2 scores (mean around 0.3) for the interval subset. For the $X = \Theta B_X$ case, we will provide results using both subsets, as both yielded satisfactory results but the interval subset being slightly easier to inspect visually.

5.3.3.1 Estimation of $\Theta = XB_\Theta$

We first consider the results presented in figure 5.11 where PCR was used to regress with the data from the first experiment. Three observations may be noted: 1) the circular-symmetric PCR inaccurately predicts non-zero complex values, while widely linear PCR correctly returns only real values. 2) The fluctuations, or noise, of the real part in the widely linear prediction are though considerably greater than that of the circular-symmetric prediction. 3) the predictive power of both the circular-symmetric and the widely linear regression models are more or less the same. Thus, while the widely linear prediction offers more 'realistic' real- and imaginary value predictions, the noise is instead concentrated in the real part. The result is mostly

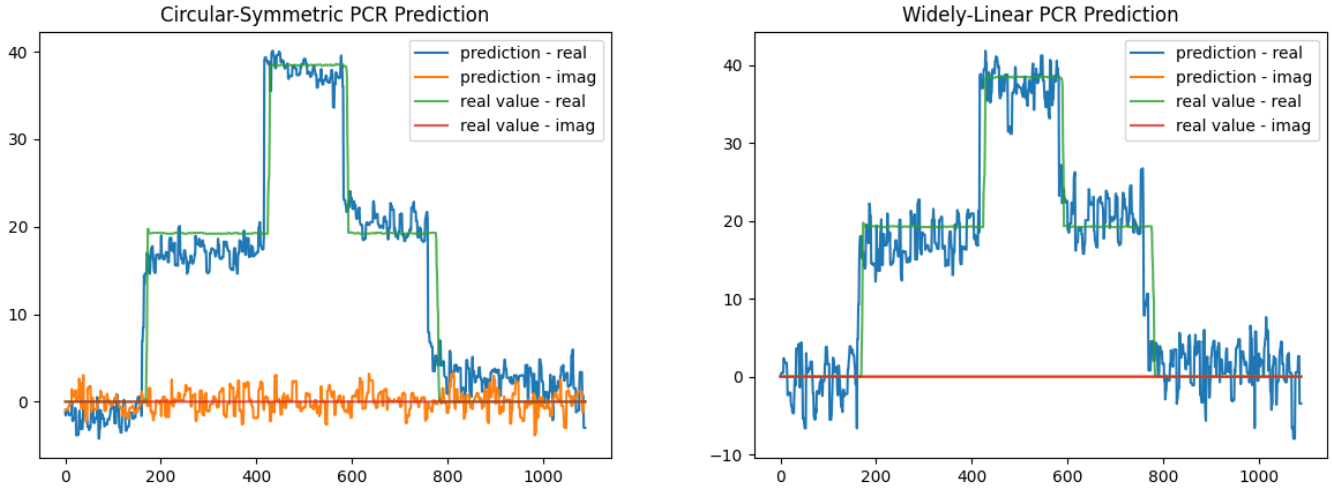

Figure 5.11: PCR regression (five components) results from the first experiment. Both the real and complex values are shown. Time (seconds) is on the x-axis, and flow [Nm3/h] is on the y-axis.

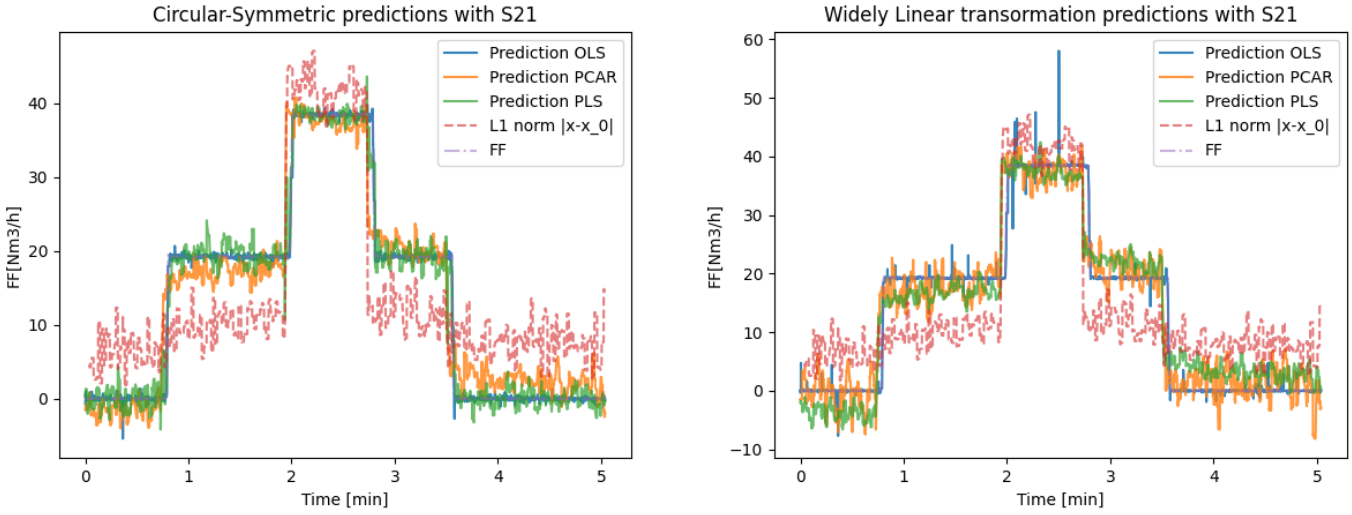

Figure 5.12: First experiment studying FF regression results. L_1 norm scaled to fit the data for comparison. For PCR and PLS five components were used. Only the real values of each prediction are shown.

consistent between different algorithms (OLS, PCR and PLS) but also between a number of predicted components throughout all experiments and regressions. As such, henceforth only the real part will be shown in subsequent figures, to provide easier visual comparison between the OLS, PCR and PLS, but the reader should keep the current result in mind.

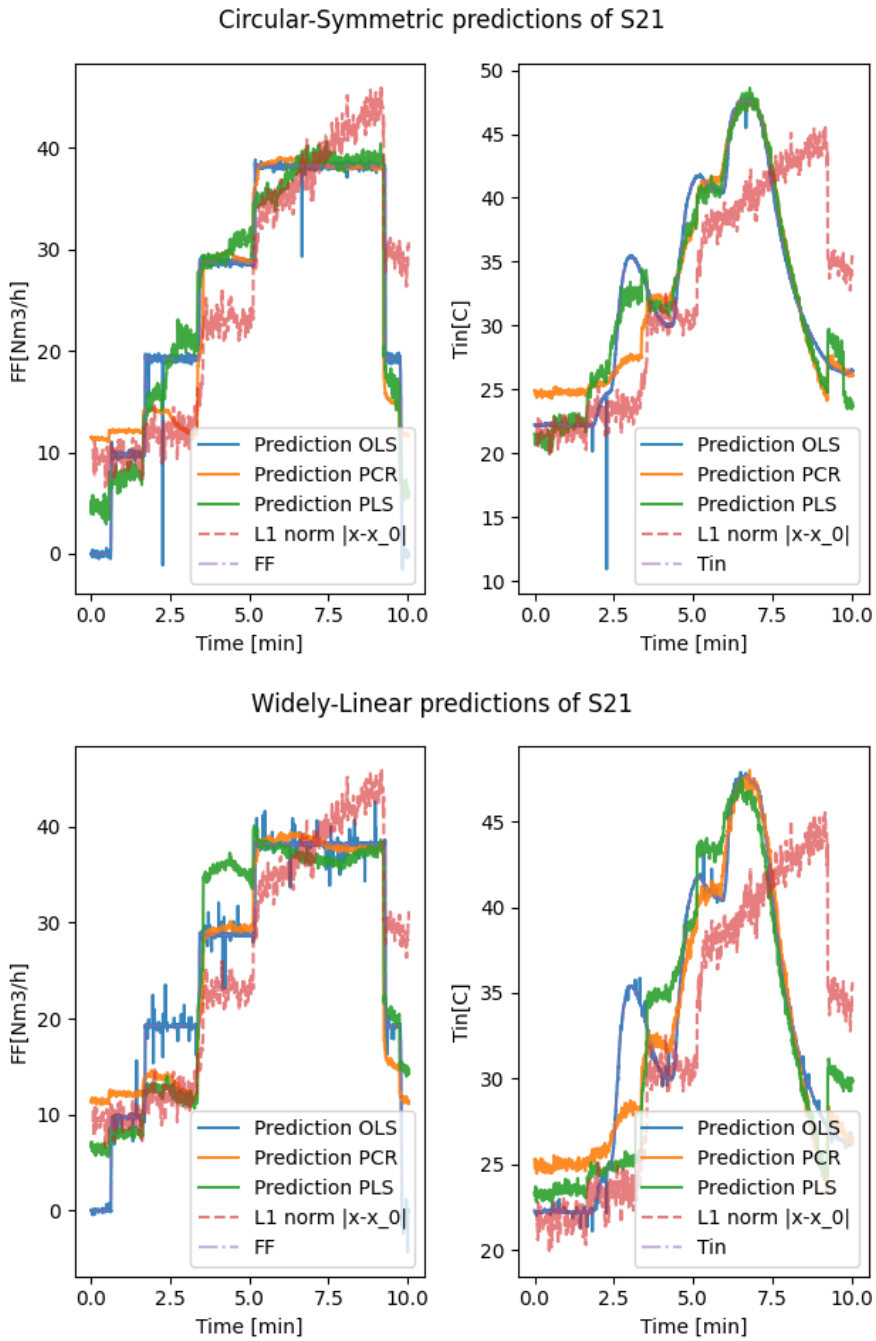

Figure 5.13: Regression results of the fourth experiment. L_1 norm scaled to fit the data for comparison. For PCR and PLS five components were used. Only the real values of each prediction are shown.

In figure 5.12 the real part of the predictions of the OLS, PCR, and PLS regressions predictions are shown for the first experiment, where FF was studied. The OLS regressions performed the best, followed by the PCR and lastly the PLS model. While noisy, the PCR model tends to follow the true values of Θ but is more noisy. Equivalent results were attained for the PLS. The OLS regression barely deviated

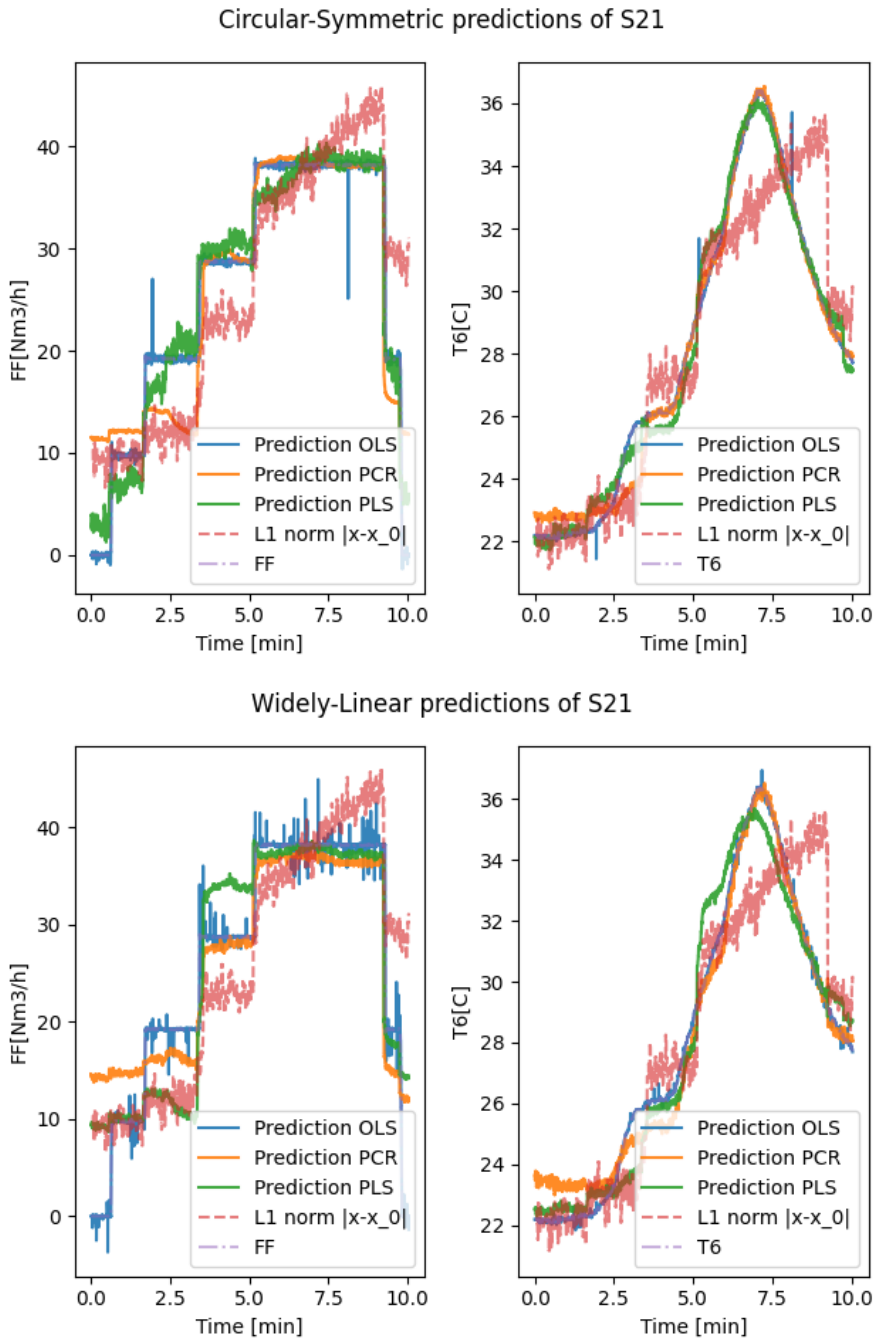

Figure 5.14: Regression results of the fourth experiment. L_1 norm scaled to fit the data for comparison. For PCR and PLS 20 components were used. Only the real values of each prediction are shown.

from the true values of FF, except for a few distinct points. For PCR, the Circular-Symmetric regression provides a better fit in general compared to the widely linear regression, while for PLS the opposite is observed. The cross-validation f the predictive power for the circular-symmetric models was: OLS - 0.98, PCR - 0.93, and PLS - 0.93, and for widely linear: OLS - 0.95, PCR - 0.93, and PLS - 0.93.

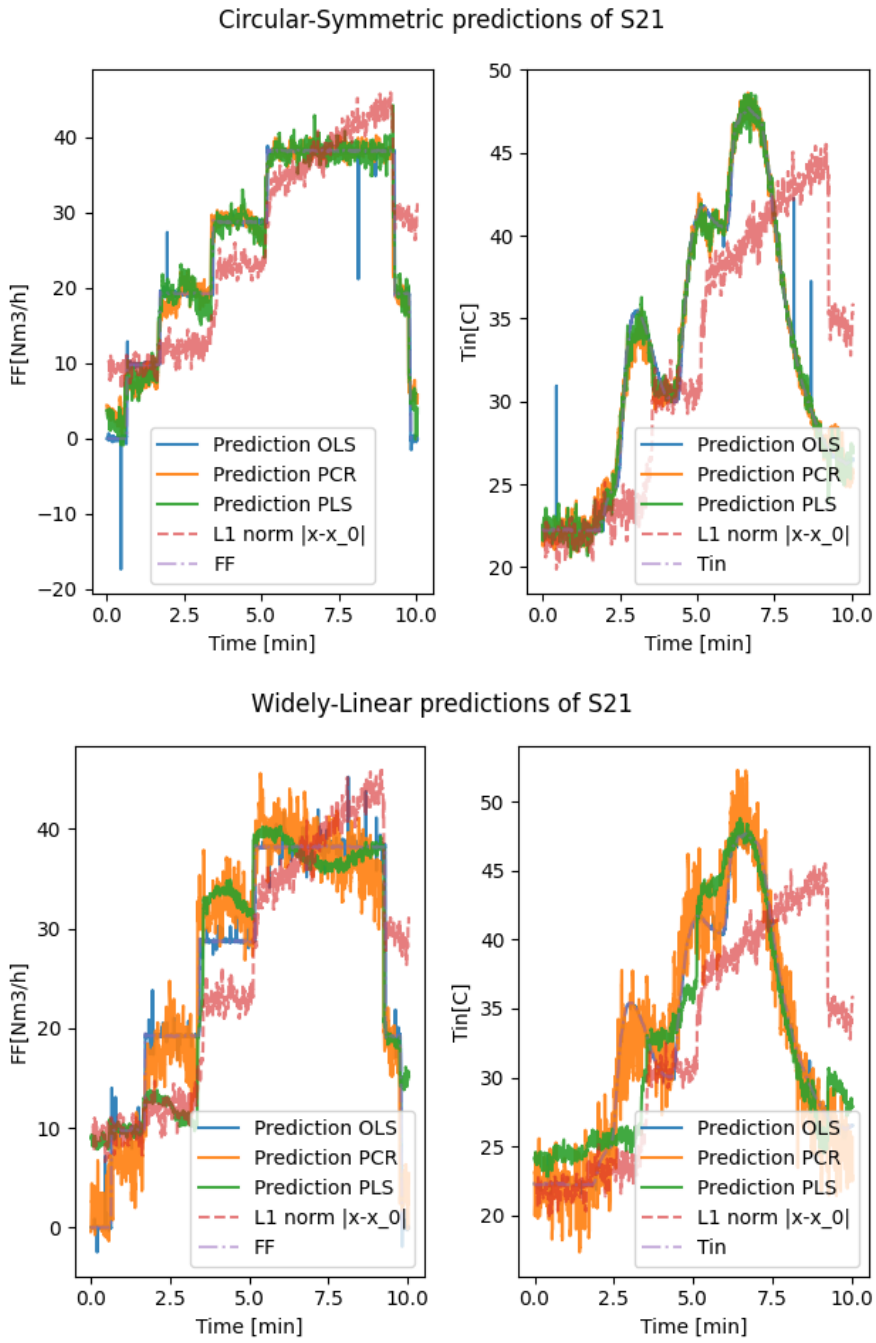

Figure 5.15: Regression results of the fourth experiment, but with T6 instead of T_{in}. L_1 norm scaled to fit the data for comparison. For PCR and PLS 20 components were used. Only the real values of each prediction are shown.

Comparable results for one parameter were attained while predicting two parameters, but both the PCR and PLS in general performed worse. As before, we first ran the regression using five components with results shown in figure 5.13. Two contributing factors to the poor results may be inquired, 1) the number of components is too small, and 2) since the T_{in} value is not measured inside the cavity, it might be

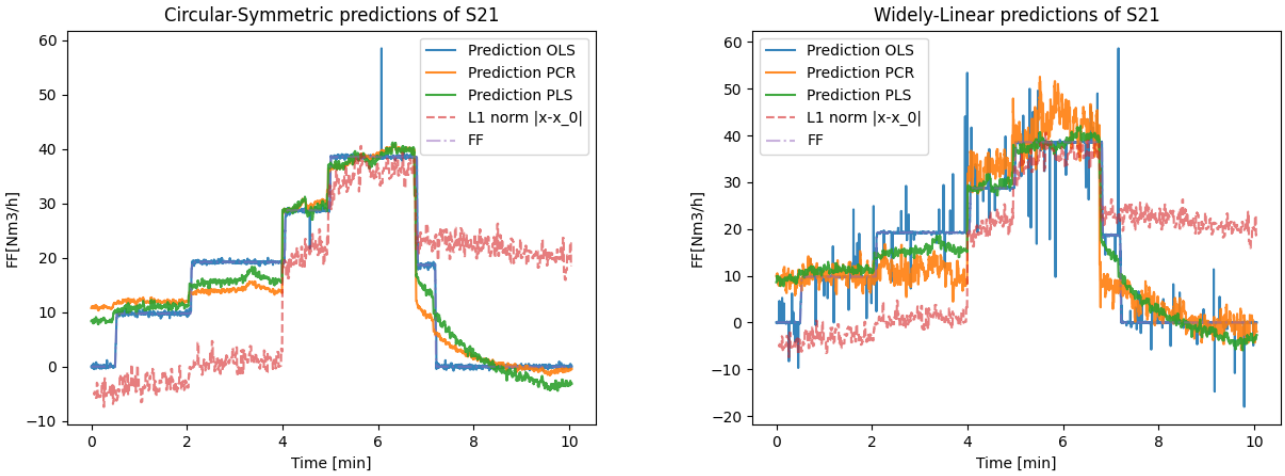

Figure 5.16: Regression results of the fifth experiment. Regression was performed with Y = {FF, AF, T_{in}, T1-T6}. L_1 norm scaled to fit the data for comparison. For PCR and PLS five components were used. Only the real values of each prediction are shown.

misleading compared to the spectrum of the sample. We re-ran the regression twice, first using T6 instead of T_{in} (see figure 5.14), and secondly with 20 components (see figure 5.15). A predicted power performance boost by approximately 20 percent for both PCR and PLS was noted for the latter, while the regression with T6 showed about a ten percent boost for the circular-symmetric and a five percent boost for the widely linear. The circular-symmetric PCR seems to visually perform the best but had slightly lower predictive power than the OLS. The mean predictive power using five components (over ten samples) of the circular-symmetric regressions was: OLS - 0.98, PCR - 0.71, and PLS - 0.87, and for widely linear: OLS - 0.95, PCR - 0.72, and PLS - 0.63.

Regression of several parameters (used parameters were FF, AF, T_in, and T1-T6) typically yielded much better results than that of one or two in the sense of predictive power. The cross-validation of predictive power for circular-symmetric models was: OLS: 0.99, PCR: 0.98, and PLS: 0.98, and for widely linear OLS: 0.99, PCR: 0.94, and PLS: 0.98. In figure 5.16 the prediction of FF is shown, where the rest was left out save space. We note that the circular-symmetric OLS and PCR prediction is several times less noisy compared to the widely linear prediction and offers a better prediction. As mentioned before, the imaginary part of the circular-symmetric in this case is much noisier while it is zero for the widely linear prediction. For PLS both circular-symmetric and widely linear have more or less the same level of noisiness, but again the widely linear imaginary part was zero where the circular-symmetric was not.

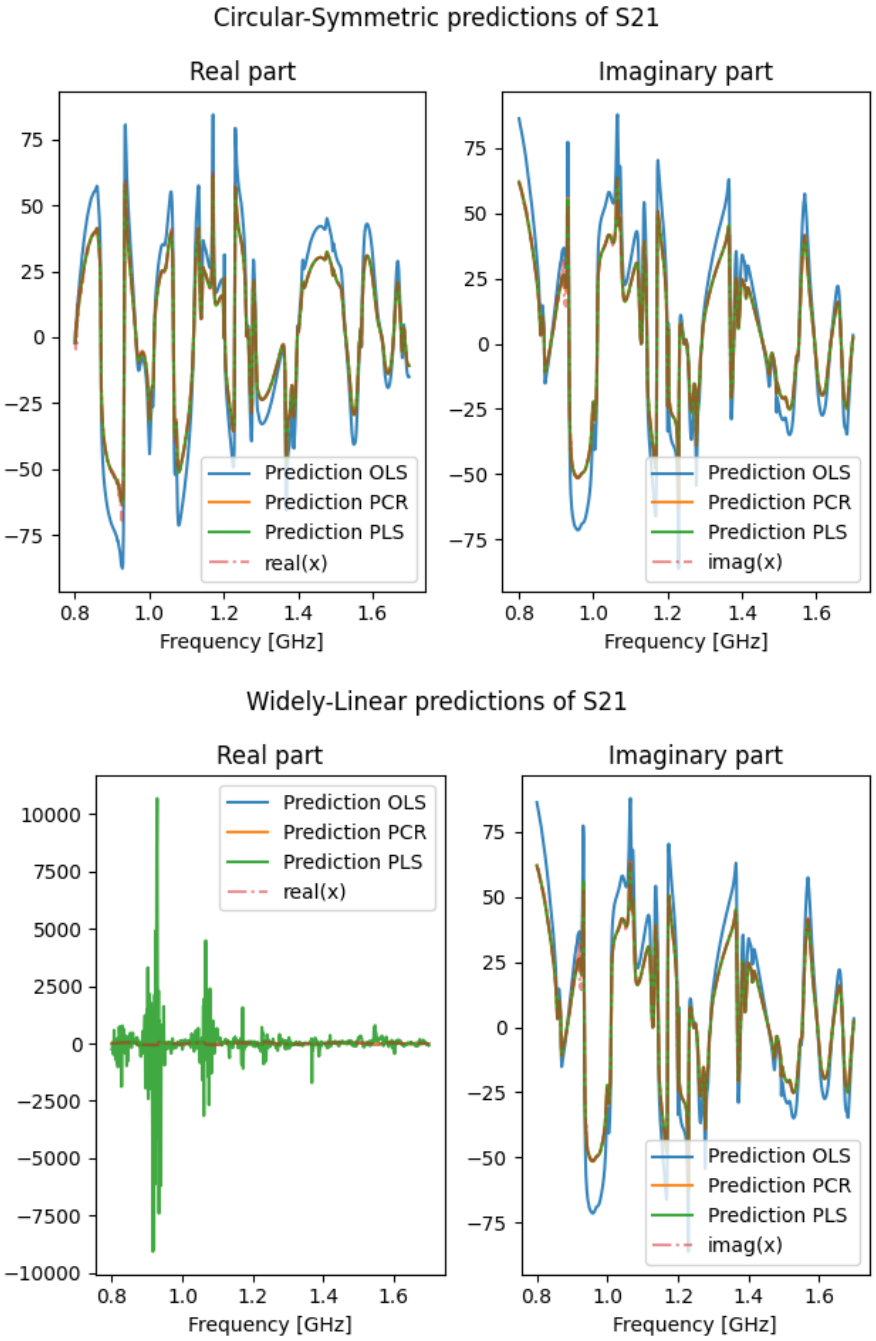

Figure 5.17: Predictions of S21 of the first experiment using the interval subset. For PCR and PLS five components were used.

5.3.3.2 Estimation of $X = \Theta B_X$

In figure 5.17 and 5.18 the predictions of S21 for the first experiment are shown, using the interval respectively variance subset. For illustrative reasons only one predicted spectrum is shown. We note that the variance spectrum is much more fluctuating and as such more difficult to predict. We also note the real part of

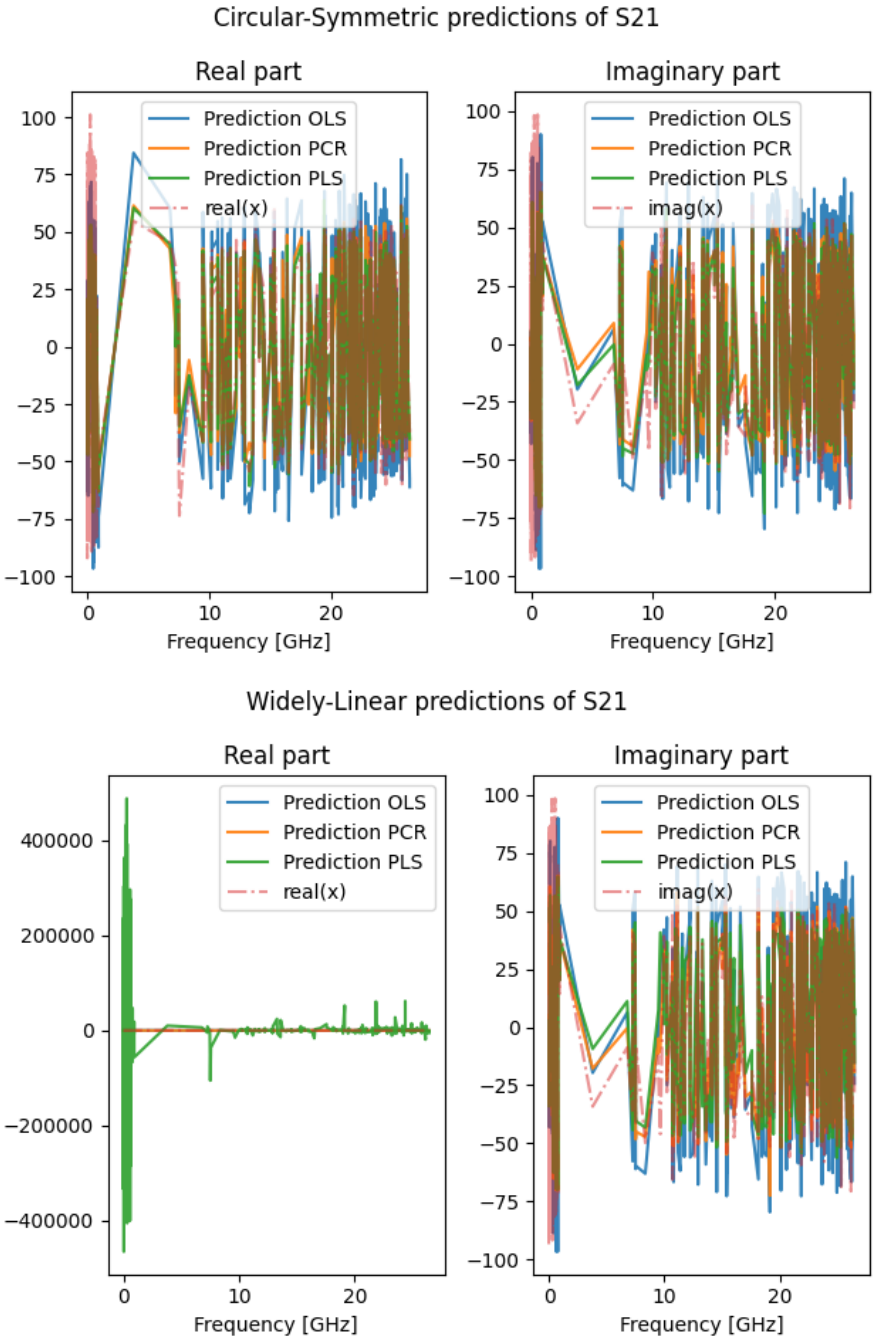

Figure 5.18: Predictions of S21 of the first experiment using the variance subset. For PCR and PLS five components were used.

the widely linear prediction, which produces awful predictions for both subsets. For the interval subset the predictive powers were recorded as, circular-symmetric OLS:0.70, PCR: 0.95, PLS: 0.95 and for widely linear OLS: 0.7, PCR: 0.90 and for the PLS the values were negative (thus invalid). Instead for the variance subset, the predictive powers were recorded as, circular-symmetric OLS:0.30, PCR: 0.4, PLS: 0.4, and for widely linear OLS: 0.32, PCR: 0.4, and again for the PLS the values were

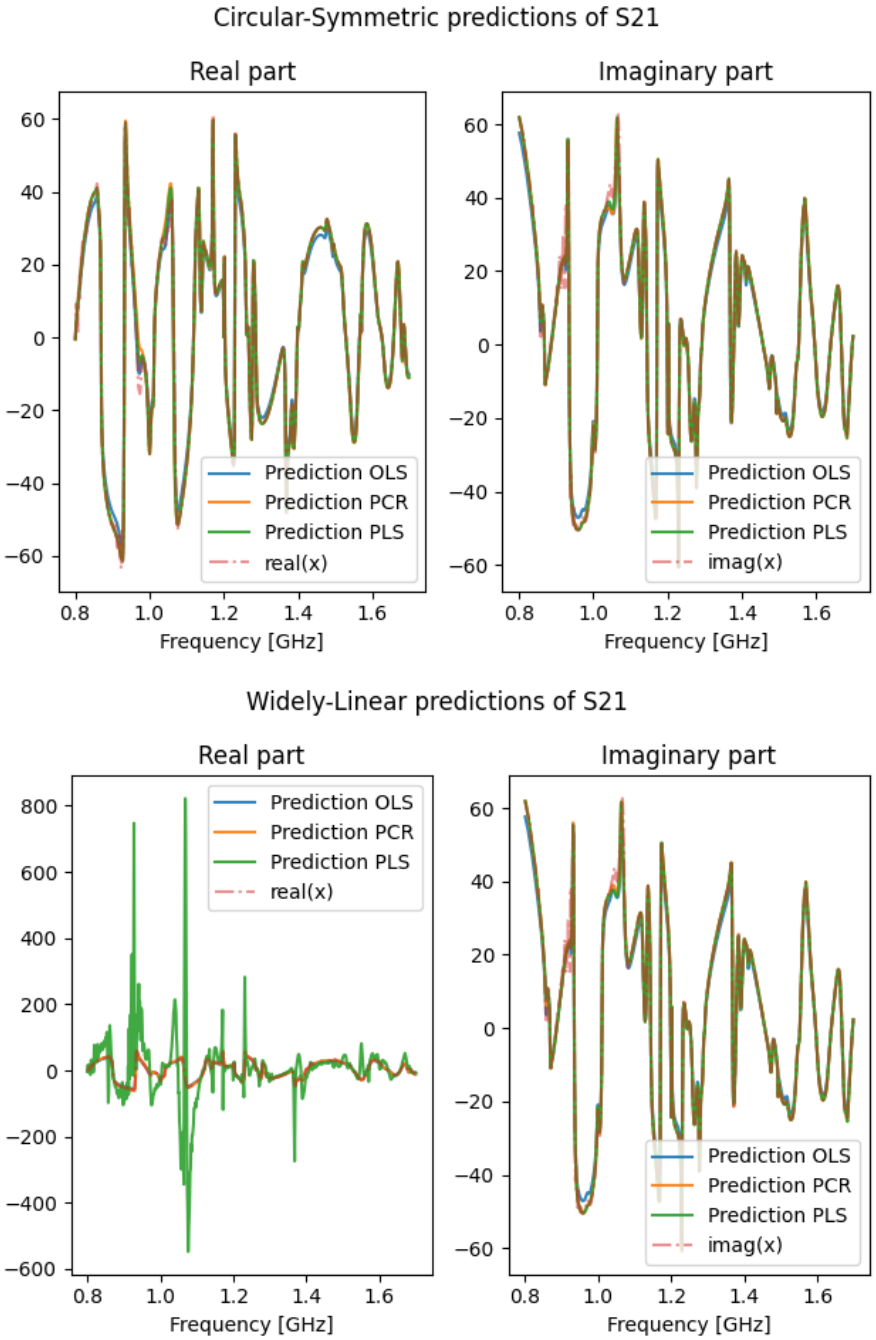

Figure 5.19: Predictions of S21 of the fourth experiment using the interval subset. For PCR and PLS five components were used.

negative. This problem seems to disappear as the number of process parameters used in regression rose, see 5.19, 5.20 and 5.20. Similarly, the accuracy of the prediction for both subsets visually increased greatly, and for six process parameters used in the predictions an accurate mean predictive power of ∼0.99 was recorded for all algorithms for the interval subset, and ∼0.4-0.5 for the variance subset, where the OLS prediction especially improved (19% as compared to the others ∼4-5%). The

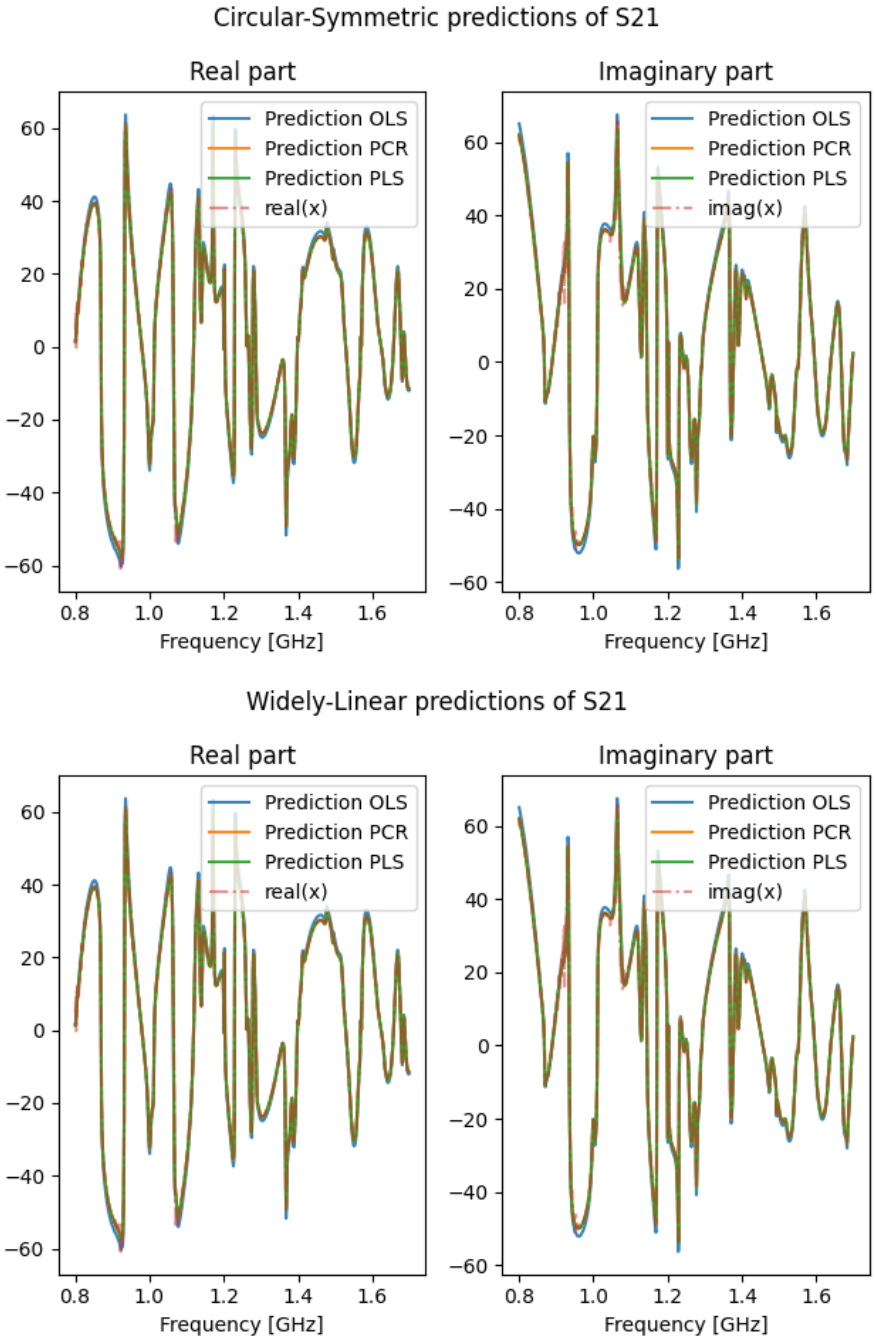

Figure 5.20: Predictions of S21 of the fifth experiment with Y = {FF, AF, T_{in}, T1-T6} and using the interval subset. For PCR and PLS five components were used.

PLS then performed as well, or better than the corresponding circular-symmetric version.

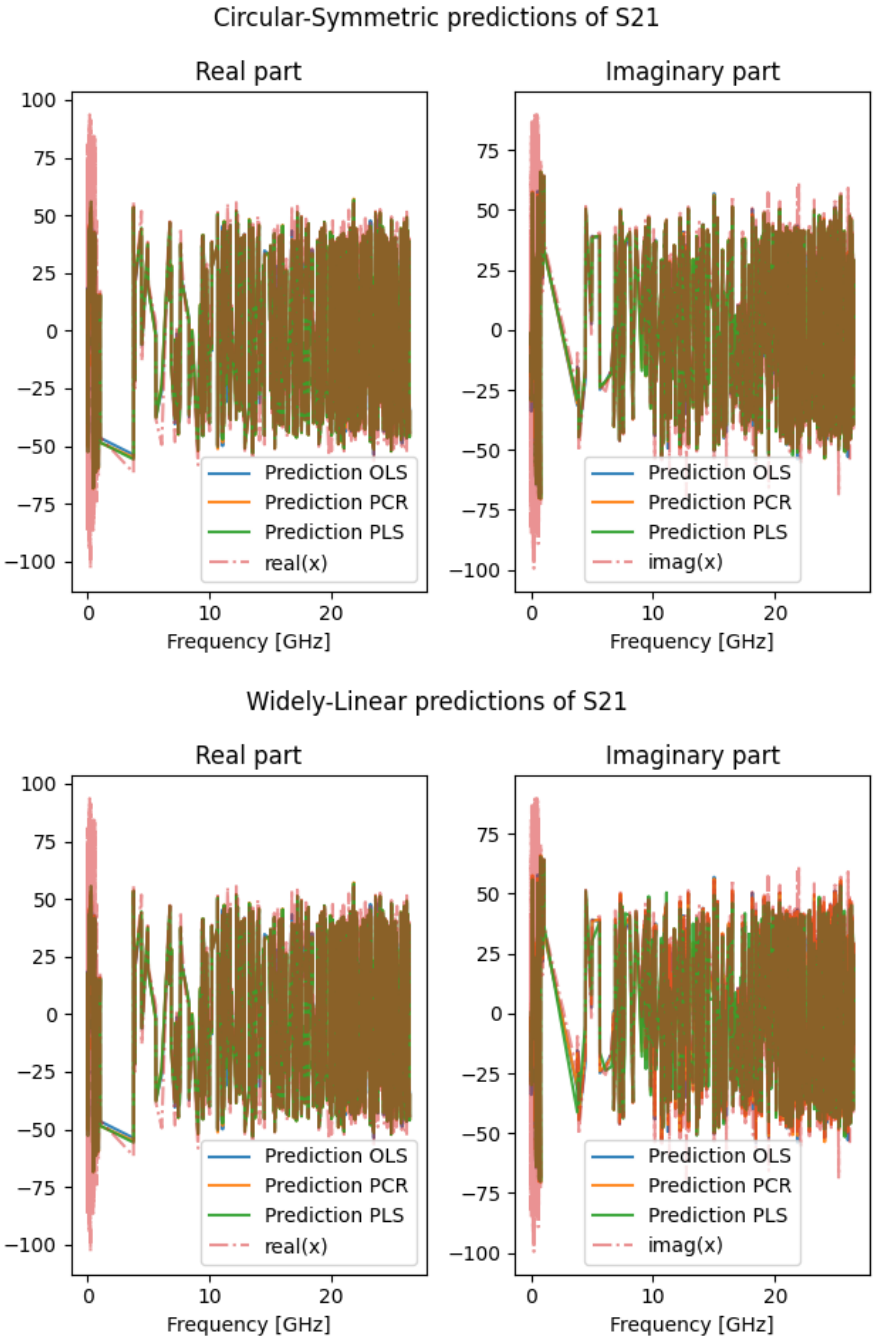

Figure 5.21: Predictions of S21 of the fifth experiment with Y = {FF, AF, T_{in}, T1-T6} and using the variance subset. For PCR and PLS five components were used.

5.4 Discussion

Analysis of the fluid bed process

From the results in the first paragraph in section 5.3.2, it is evident that a direct

improvement of the current solution is to stabilise the antennas. Currently, the measurements suffer from several instabilities such as loose filters (top and bottom) and weak antennas which is affected by process parameters. The weak antennas also pose a different problem, which occurs when the antennas are cleansed and, in such cases, typically bend. A remedy is to increase the strength of the H-probes by covering them with a low-dielectric, stable material.

In addition to strengthening the probes, the added heat sensors T1-T6 should either be removed or fastened more carefully, as they provide a non-trivial, undesired contribution to the measurements. Disassembling and reassembling the fluid bed needs to be consistent, as we otherwise would have shape perturbations in the measurements. We though note that these could be accommodated for using the shape perturbation equation 2.8. We also note that the distance between the filter at the bottom and the Wurster tube must be the same. Additionally, there is a need for shielding the fluid bed, VNA, and the coaxial cables connecting them from outward disturbances.

From the second paragraph, we simply note that the effect of FF, as compared to AF and T_{in} is considerably greater. A possibility to mitigate the effect is possibly to, yet again, strengthen the antennas as well as the heat sensors T1-T6. This could simplify the analysis of the particles, which would then have a larger relative effect on the relative perturbations. We note that as expected the AF flow only affects the measurements greatly if particles are present in the system, as it has a considerably smaller flow strength (a tenth of FF) but affects the positions of the particles more. Since we also know that the particles will flow fountain-like, areas such as what was shown in figure 5.4 are of special interest. Without the presence of particles, the AF flow contribution is not much higher than that of noise and has no permanent effect on the system.

From the sensitivity analysis of the current set-up, it may be noted the problem is ill-posed / ambiguous due to permanent changes in the system. This is of course undesired, and measures to accommodate this should be implemented. While not tried here, a possible simple analytical extension of the current implementations would be an extra Tikhonov regularisation term in the OLS approximations (thus extending it to ridge regression).

Estimation of Θ and X

Regardless of the experiment, the OLS provides better predictive power than PCR and PLS which was surprising. The OLS prediction though finds discrete values where the residual of the predicted value and the real value differs greatly. The cause is believed to be overfitting, in which slightly off values provide completely off predictions. Considering this, both the PCR and PLS provide more reasonable results. The noise in the circular-symmetric predictions seemed to be distributed over the real and imaginary parts, where the imaginary of course in reality is zero. For the widely linear regressions, the noise previously in the imaginary part seemed to transfer into the real values, providing a noisier prediction, although accurately

with a zero imaginary part.

In the estimation of $\Theta = XB_\Theta$, when only one parameter was predicted all algorithms performed well with high predictive power. When a second parameter was added, the predictive power was significantly lower but could be increased again simply by adding more regression components. Even more process parameters gave an overall performance boost to the predictive power, but when inspecting specific predictions process parameters the results seems off. We thus note, as expected, that increasing the predicted values becomes quickly increasingly difficult. The number of regression components is vital, and the priority should be to optimally decide such that it is not set too low.

Opposite from the estimation of Θ, the predictions of $X = \Theta B_X$ showed that the more process parameters that were used, the better predictions. Yet again this should be expected behaviour. The OLS predictions typically performed worse than PCR or PLS. There was no gain from using the widely linear versions rather than the circular-symmetric. The results suggest the use of either PCR or PLS over OLS, but both should be further trained on more data.

The effect particles induce of the temperature distribution, FF, and AF was not studied, and how it will affect the measurements is thus unknown. The L_1 norm though seems to suggest that the process parameters in general have a greater effect on the microwave measurements than the particles, and optimally models should be studied on concatenated data sets. This could be accomplished by iterative models, in which also larger subsets may be studied. As such development of more advanced prediction models can be seen as the next step after the thesis.

5.5 Conclusion

In conclusion, the current implementation of the global monitoring (see 5.1.2) of the fluid bed had several flaws, both practically and analytically, and we have proposed improvements and countermeasures for each. Specifically, the antennas need to be both strengthened and shielded from the fluid bed process. This could be accomplished by covering the antenna with a dielectric material. Another important finding is that the equipment used has to be adapted to a situation where all parts can be placed into exactly the same positions after e.g. cleaning to contribute as small variation as possible. Additionally, all parts need to be free of movement during the process run. Analytically, a foundation has been explored and extensions to the previously published attempts have been suggested. It was noted that the naive estimation of the priori for the ridge regression previously used by others assumed circular-symmetric complex-valued data. This may be detrimental if there are small faults in the priori estimation. Several widely linear adaptations of standard linear regression algorithms to improve this estimation was proposed and the performance of each compared to their circular-symmetric correspondence was studied. The results at this stage contain models and methods to describe the X_E part of the solution. Due to time limitations, analysis of the data in relation to the

particles that are in the X_P part of the solution was moved to future work.

For the prediction of process parameters, the widely linear models were better at predicting the imaginary part than the circular symmetric counterparts. For the prediction of spectra from process parameters, there was no particular gain observed with widely linear models. In particular, the PLS model breaks down more quickly for the real part than the other algorithms when fewer process parameters are employed.

6

Case III: Electroporation of cells

As specified in the introductory chapter, 1, the following chapter will include two cases; both the electroporation case and the particle properties case. The cases will be split into sections, where each section will include both an introduction, a small literature review, an idea and implementation (with results), and finally a discussion of possible future improvements.

6.1 Electroporation using microwaves

We first present a brief introduction to the electroporation concept and a few examples found in the literature. Subsequently, we provide a brief theoretical section covering the electroporation process both on a biological and mathematical level, followed by a section covering important considerations while performing electroporation as told in the literature. Two important, and influential, articles for the project which attempted electroporation using microwaves are then covered in deeper detail, followed by the method and result, and lastly, a section discussing the current implementation, concluding the electroporation case. It should be noted that no experiments with cells were ever conducted, with reasons covered in the result and discussion section. The project was instead concluded early.

6.1.1 Introduction

Transfection using electrical field pulses at different wavelengths, conventionally called electroporation, is a convenient method to increase and accelerate the uptake of molecules of cells (38). The attractiveness of electroporation, compared to other transfection methods, can be seen from its applicability across cell types. Using electroporation, mammalian-, insect- and yeast cells have successfully been electroporated where only the field strength pulses have been varied (38; 39).

The main idea of so-called reversible (explained below) electroporation is to create pores/a passage in the cell membrane for molecules, ions, and water to migrate over the plasma membrane (39). The migration, which may occur in both directions, typically takes milliseconds (7; 38; 39). Several factors should be considered, such as electrical field strength, pulse length but also buffer mediums. The cell type to be electroporated may though affect chosen parameters, where for instance cell size

directly determines required field strength (39). Most such experiments are conducted using two parallel plates to establish the electrical field (38; 39), although this approach has found some criticism of having low cell viability (7; 40). Traditional approaches typically use a batch of suspended cells when electroporated, but other methods where cells are electroporated as single cells have been developed offering higher cell viability (40; 41). That being said, methods where both a larger cell count, high uptake, and low cell mortality have been recorded (7; 8).

Typically, electroporation can be divided into two sub-types: reversible and irreversible. In reversible electroporation the aim is to apply an electric field just strong enough to open pores but avoid the cell from bursting or rapture, and where the cell after treatment may regenerate. (40) In irreversible electroporation, the intent is instead to kill the cell, by creating a large enough rapture to burst the cell. In the current thesis, the aim was to develop an in vitro, reversible electroporation method to assist studies where the aim is to introduce foreign molecules to cellular bodies.

6.1.2 Electroporation theory

We cover three topics in this section; Transmembrane voltage, pore creation, and finally pore size. The concept of electroporation is much more complex than how it will seem here, the belief of the author is that what is discussed below is enough for conducting successful electroporation. The interested reader is instead referred to other literature.

Trans-membrane voltage (TMV):
While several working theories persist and the fundamental process and dynamics of electroporation remain unclear, theories and models simulating the dynamics with supporting experiments are under heavy development (42–45). The main idea of electroporation is that pores (holes) develop across the cell membrane allowing for greater cell permeability when an external electrical field pulse(s) is applied to the cell (42). It is believed that these pores (raptures) develop in a stochastic fashion dependent on the trans-membrane voltage (TMV, or V_m), and that there is some kind of critical voltage level which results in a higher probability of raptures (42). The typically used equation for approximating TMV is given as,

$$V_m \approx 1.5Er|cos(\alpha)| \tag{6.1}$$

where E is the electric field intensity, r is the cell radius and α is the angle between the incident wave and the normal of the pore center point (39). This equation has been used frequently in several published articles but may be faulty in higher frequency areas. Instead, the so-called *Schwan equation*,

$$\begin{aligned} V_m &\approx \frac{1.5Er}{\sqrt{1+(\omega T)^2}}|cos(\alpha)|, \\ T &= \frac{rC_m(\rho_i + 0.5\rho_a)}{1 + rG_m(\rho_i + 0.5\rho_a)} \end{aligned} \tag{6.2}$$

can be used. Here, ω is the angular frequency and T is a time constant. C_m is the membrane capacitance per area unit, G_m is the membrane conductance per

unit area, and ρ_i and ρ_a are resistivities in the cytoplasm and extracellular space, respectively (47).

A quick review of articles gives values for C_m as 0.9 $\mu F/cm^2$ (48), for G_m between $0.013 - 0.028\ \ 1/(\Omega cm^2)$ (49), for ρ_i between 40 - 74 Ωcm (50) and if we also assume the surrounding medium to be PBS, then ρ_a as $0.0001\Omega/cm$ (51). Thus using the definition of T (eq. 6.2), and using typical mammalian cell radius, r between $0.5-5\mu\ cm$ (or possible smaller) (52), we note that T is of magnitude $10^{-8}-10^{-5}$. For low frequencies or DC current, we can thus use eq. 6.1, but for higher frequencies, were ω is of frequency MHz or higher, the denominator $\sqrt{1+(\omega T)^2}$ in eq. 6.2 must be taken into account.

The equations above are approximated for thin-layered cell membranes, and validity may be lost for thicker membranes. If the approximation holds, pores may be created when the TMV reaches 0.5 V or higher, although this value may be dependent on environmental aspects (39).

Pore creation and location:
The cell membrane consists of a two-layered, non-planar, non-zero trans-membrane voltage phospholipid bilayers with proteins present scattered across the layer, and acts as a semi-permeable protection to the cell (42). The phospholipid bilayer consists of molecules both with a hydrophobic part (tail) and a hydrophilic part (head), where the tails are connecting, resulting in an amphipathic bilayer. Two theories of how the pores establish can be derived from this observation; either a pore is hydrophobic, meaning the heads rotate inwards the pore's center, or, the pore is hydrophilic meaning it kept the original shape and only the molecules have separated (42). Both theories have been experimented with and supported previously, but no official irrefutable proof for any of them has been presented to the authors' best knowledge (42; 46). Additionally, based on simulations and numerical results, a hypothesis is that pores do not develop close to proteins in the phospholipid bilayer, and are more likely to appear where mostly the phospholipid bilayer is present. Another hypothesis states that pores can fundamentally be seen as water tunnels, from one layer to the other (42).

Pore size:
The pore size mostly depends on the applied electrical field strength, although other important factors may also have an effect, such as temperature (7), pre-treatment using shock wave(s) (53), or choosing a different buffer medium (39). Pores typically form in a matter of microseconds and for reversible electroporation, close again after a couple of seconds (7; 39; 42). As specified below, the regeneration time may differ.

6.1.3 Considerations and important factors for successful electroporation

In (39), important factors for successful electroporation are given as; specified waveform (typically square or exponential decay wave), chosen wave duration/pulse length (depends on frequency), wave amplitude, and field strength, number of pulses,

and electrode distance(s) (if applicable) when designing a construct. These specifications can effectively be determined by cell type and cell size. Other parameters mentioned include environment temperature, type of buffer medium used, and the concentration of DNA/RNA. In (42) the importance of pulse form, exposure, and number of pulses are again stressed, but also the choice of using DC or AC current, where DC typically is used (47).

The buffer medium may have a great effect on cell viability but may also affect the electroporation. For instance, PBS may generate a considerable amount of heat due to being inherently conductive, which can increase cell death. Instead, buffer mediums that may be used could be HEPES, DMEM, and Opti-MEM to name a few (39).

J. Gehl (54) discussed post-pulse strategies, such as waiting up to 15 minutes before performing subsequent experimental steps, so that the cell pores have proper time to reseal. Some studies claim that this process can be as short as a couple of seconds (42), while others claim it may take hours (55). J. Gehl also mentions electrode material and medium as important decision factors, where for instance aluminum electrodes can release metal poisonous to cells, and if calcium is present in the medium, it may cause high unwanted intracellular electrolytes production.

Sönke Schmidt et al. (7) took this a step further and considered cell toxicity of the cuvette and substrates additional to the electrodes, and coated adjacent materials with gold. In their experiments, they attempted electroporation using higher electrical field strength and higher frequencies compared to most articles, and they concluded that pore creation is mainly due to the high-frequency electrical field, rather than dependent on the temperature caused by the fields.

An important consideration in developed electroporation devices as described in most reviewed cases, has been the observability of the processes. As such, a part of the construct is left visible to e.g. a microscope, which may monitor the process during electroporation(7; 40; 41)

In summary, important optimisation factors include,

- wave properties; shape, amplitude, duration, repeating waves/number of pulses, field strength, frequency,
- current type; AC or DC,
- electrode design; distance, waveguide(s), placement, number of electrodes, material of electrodes,
- cuvette design; single- or multicell study design, cuvette and substrate material,
- protocol; buffer medium, DNA/RNA concentration, post-pulse waiting time, pre-heating or pre-cooling, pre-treatment, post-treatment.

6.1.4 Electroporation using microwaves; two cases

While several articles on microwave electroporation have been published, two stand out in particular; *Microwave Induced Electroporation of Adherent Mammalian Cells at 18 GHz* by Sönke Schmidt et al. (7) and *The biological effect of 2.45 GHz microwaves on the viability and permeability of bacterial and yeast cells* by Evans Ahortor et al. (8). The rationale for choosing these reports over others lies in their principally easy replicable, bulk-cell container approaches offering batches of cells (as compared to single cells) to be electroporated with high cell viability. Of the two, Ahortor et al. used the familiar cylinder cavity resonator, which would fall close to what already has been accomplished within this thesis. Schmidt et al. instead used a co-planar waveguide to electroporate the cells.

In the article published by Sönke Schmidt et al. (7), an in vitro, reversible electroporation experiment was successfully conducted at 18 GHz, using an ungrounded co-planar waveguide situated under a thin glass strip mounted on a brass structure for stability. The cell batch was pipetted into a hole made in a Rexolite which was mounted on the co-planar waveguide. The cells were then electroporated by direct contact with the electrode. The construct made it possible to directly monitor the process by placing it under a microscope, and the cells were subjected to microwave treatment using PBS as the medium. They observed the uptake of molecules by the cells first after 10 minutes after treatment, and the experiment was then concluded after 20 minutes. An important result of their experiments was regarding the produced heat effect on successful electroporation. They concluded that heat does not increase transfer but may possibly assist to a low degree.

In the second article, by Ahortor et al. (8) electroporation was carried out by adding three holes in a metallic cylinder with increasing distance from the cylinder center. They set the frequency to 2.45 GHz, which was constructed to be the base mode TM010 operating frequency, and performed three experiments, one at each of the added holes. As such they could observe the different uptake efficiency for different combinations of the electric (E) and magnetic (H) field intensities, namely (strong E, weak H), (half-strong E, half-strong H), and (weak E, strong H). From these experiments, they concluded that only the electric field has any effect on the cells' transfection rate.

In conclusion, the method used should have high electric intensity but should avoid the heating effect of microwaves. The sample may of course be cooled during the process, but the experimenter should be careful not to kill the cells due to low heat. A disadvantage of both methods is the lack of re-usability of the built constructs due to contamination of the batch-holder between the experiments. Optimally, the batch holders should be replaceable, or the construct should be able to integrate common holders into the process.

6.1.5 Method and results

Neither the VNA nor the SDR has the initial capabilities to perform electroporation, as the initial power (Watt; Joule/sec) is too weak to reach an electric field strong enough to create pores. Therefore, a Wolfspeed power amplifier was connected to increase the intensity. Unfortunately, the amplifier was broken and missing a capacitor, in which three weaker capacitors were soldered on the amplifier chip to accommodate for the missing piece. A small circuit was then built to provide the amplifier with enough power to operate, as per the amplifier's manual instructions. Additionally, the power amplifier was limited to the 5 - 5.9 GHz frequency span, and thus constructs should optimally be adjusted to a frequency inside this span.

The VNA was used to analyse the systems and find optimal frequencies to electroporate, while the SDR was used to create the waves. The reason for changing instrumentation lies in the control of the waveforms, where the SDR offers more flexibility. A simple GNURadio program was built to generate a bipolar square wave with frequencies 5.35 GHz and high intensity, followed by several low-intensity square waves. In figure 6.1 the small program with the corresponding wave can be viewed.

Two initial designs were originally attempted; the first was designed as a microwave stripline resonator imitating the idea of (7), and the second as a rectangular cavity resonator based on (8). Due to difficulties in receiving a good enough Q-factor and accurate resonant frequency with available methods (taping and cutting), the stripline construct was quickly abounded. The rectangular cavity was constructed using a nearby metallic box, and the setup can be seen in figure 6.2. The cavity could possibly yield a good, feasible electroporation procedure, in which multi-well pipetting plates can be placed inside, see figure 6.2. In each well located inside one of the high-intensity areas of the cavity, electroporation could occur, effectively enabling a multi-batch solution for electroporation. The multi-well could be a pipetting plate used in standard procedures where its lid would not need to be removed, diminishing the chances of additional contamination.

The cavity is of dimension (0.12, 0.19, 0.04) m, and we calculate two resonant frequencies, TM420 and TM311, to be both in the amplifier range but also well separated from other resonant frequencies. In figure 6.3 measured amplitude of S11 and corresponding eigensolutions TM311 and TM420 are shown[1]. We note that the measured resonant for TM311 is almost identical to the theoretical value and that the electric field distribution offers three different high-intensity areas, in which the cells to be electroporated should be placed. Furthermore, the measured peak of TM311 had both a better Q-value and higher attenuation and was thus chosen to be the electroporation frequency. To verify that it indeed is the TM311 mode, a tissue was dragged from one side to the other, in which the intensity changed according to the field distribution.

[1]The filed distributions have been plotted by solving Helmholtz equations similar to appendix A.8, and can be found in (56)

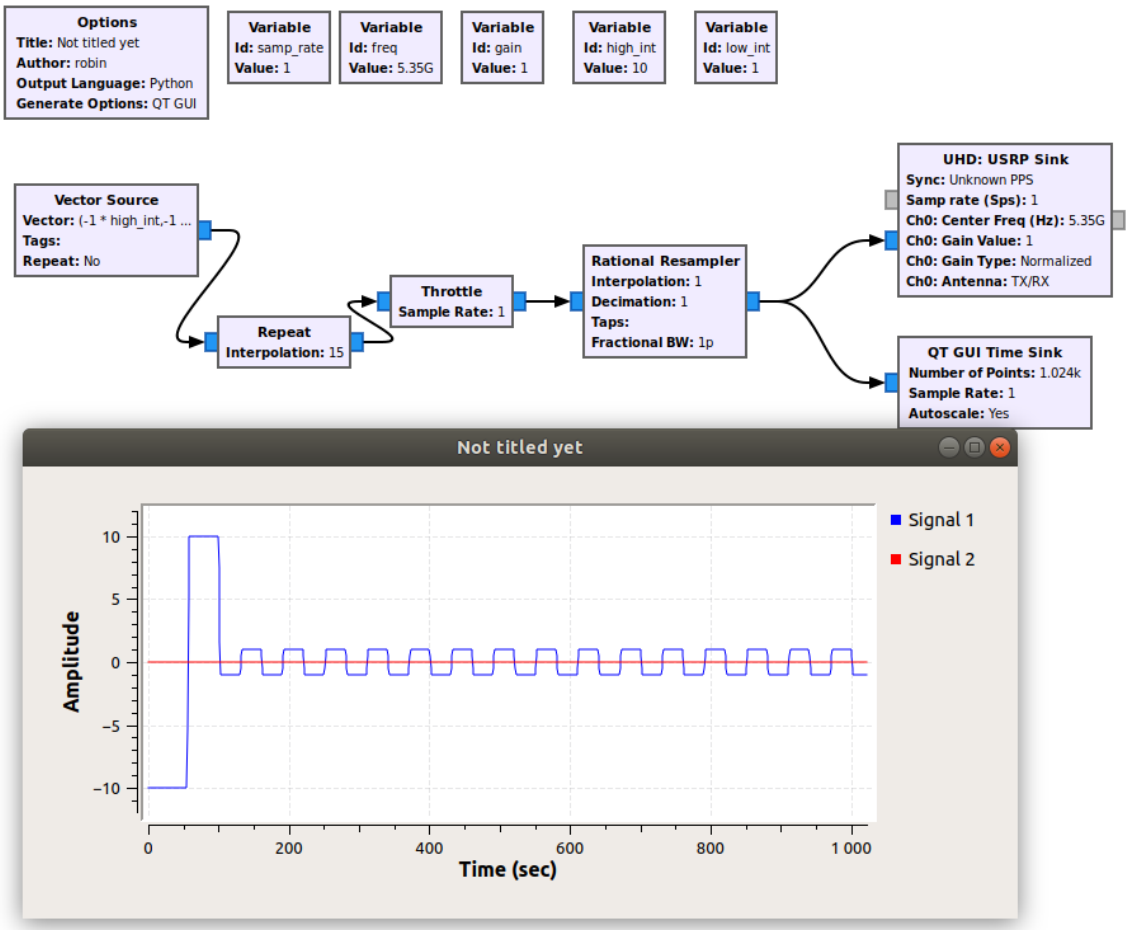

Figure 6.1: GNURadio file for electroporation, with the resulting wave. The sample rate was set to a low value for reassurance that the plot would not update, and the pulse length was made long for illustrative purposes.

As noticed by comparing the resonance frequency close to 6.25 GHz, the resonant frequencies at 5.35 is sub-optimal. To accommodate for this a longer antenna was soldered onto the current to match $\lambda/4$ wavelength but resulted in less accuracy and heavy distortions in the measurement signal and ultimately the TM311 mode was lost. A few different attempts were made, but no satisfactory results were found with similar issues as before.

6.1.6 Discussion

The tests concluded early, and the project was abounded to attain more time for the other cases. There were several reasons for this, and the current section will provide the reasons why, as well as discuss possible improvements.

The antenna was not optimised for the specific frequency, which was not solved with satisfactory results. The believed reason as to why is the additional noise resulting in the soldering but also a miss-match with the 50 Ohm impedance. Additionally, the fields are perturbated due to the size of the addition on the antenna, which could

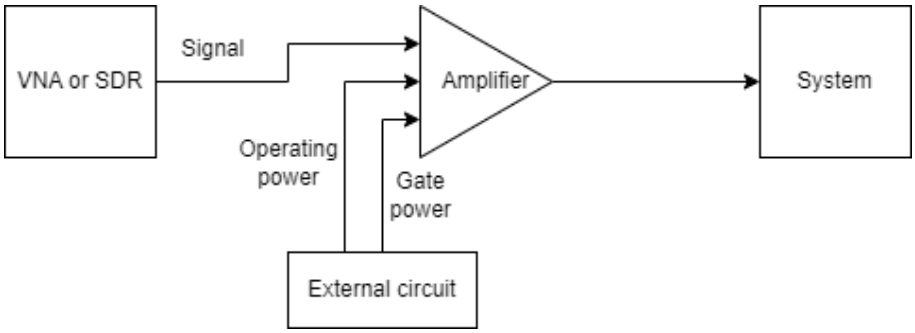

(a) Electroporation circuit schema. Drawing made using the `https://app.diagrams.net/` online drawing program.

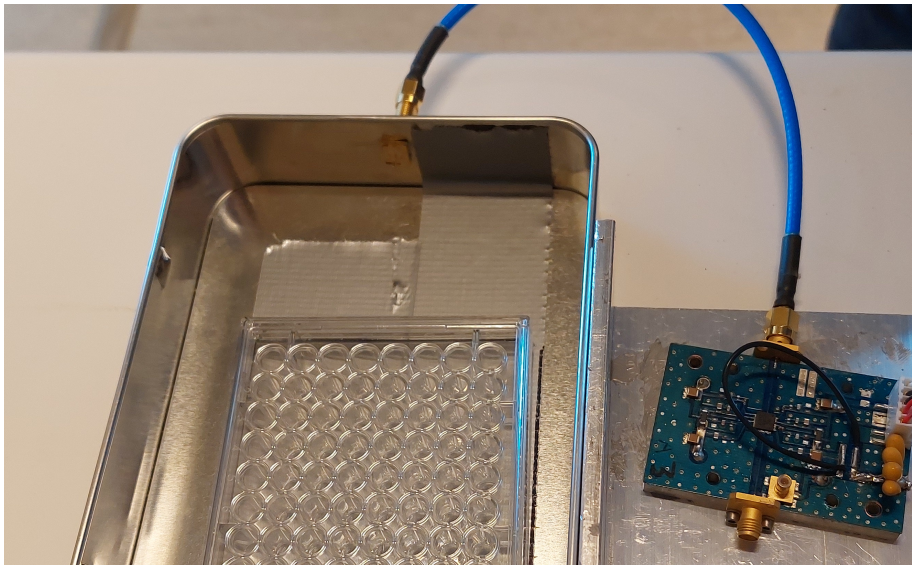

(b) Cavity resonator connected to the power amplifier. The power amplifier is glued using thermal paste on a thick metallic plate to distribute potential operating heat. Inside the cavity a standard multi-well, pipetting plate has been placed.

Figure 6.2: Electroporation experiment setup. In a) the schema, and in b) the 'system'/ electroporation constructs.

not be neglected with the small metal box. The original antenna was instead very small and constructed to match the 50 Ohm impedance, resulting in good agreement with theoretical values.

Typically, the fundamental mode with the lowest resonant frequency, TE101, should be used instead of higher modes. The fundamental reason is the increased power loss in walls when the frequency is increased (56). As such, either the cavity size should be decreased, or the amplifier should be swapped to one with a lower allowed frequency range.

Another reason why the project was concluded was that both the external circuit and the capacitor attachment to the amplifier were sub-optimal. For the amplifier, the soldered capacitors fell off one time before being re-soldered more carefully. Even

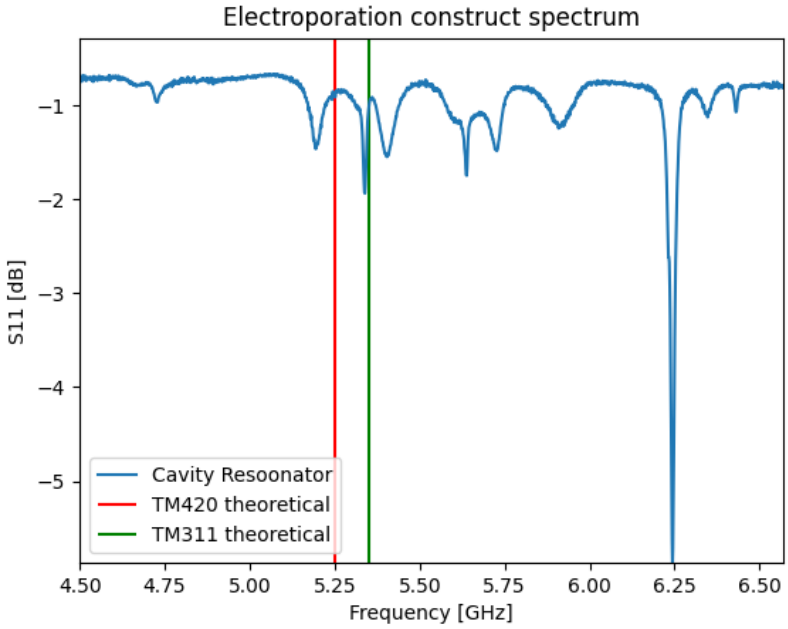

(a) Magnitude of S11 around amplifier range.

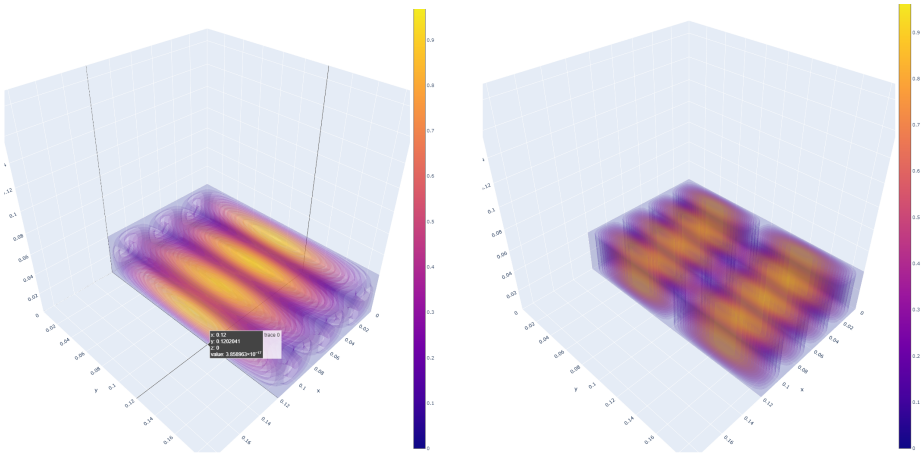

(b) Electric field for eigensolution with mode TM311.

(c) Electric field for eigensolution with mode TM420

Figure 6.3: a) Measured amplitude of S11 with two theoretical values for resonant frequencies TM311 and TM420 shown, and b) E field solutions of TM311 (left) and TM420 (right).

then the stability of the capacitors was weak. Optimally, a new amplifier with a corresponding circuit should be bought.

Lastly, and most importantly, due to the currently low progress in the numerical simulations (using Elmer, see appendix F), the amplitude and signal strength to get the electric field and corresponding TMV (using eq. 6.2) had to be guessed. Due to the non-trivial system but at the same time intensity-sensitive cells, guessing would be far from a trivial task. As such, progress in the numerical simulation area would

be welcomed. We note in the later phase of the project that the modelling could be accomplished by calculating the so-called poytning vector, $S = E \times H$, which correspondingly relates the electric and magnetic energies densities, as well as the power dissipation density by the *Poyting Theorem*. Thus, in addition to the electric field across the membrane, heat transfer can also be calculated. There have lately been a few published examples of Elmer attempting heating of various objects using this method.

7

Case IV: Characterisation of chemical sample properties

A brief introduction is presented, followed by theory as well as some examples from literature for the T-resonator, and how it may be used for determining sample properties. Constructed T-resonator and results are presented followed by a discussion of the results and finally the chapter is concluded with future improvements.

7.1 Introduction

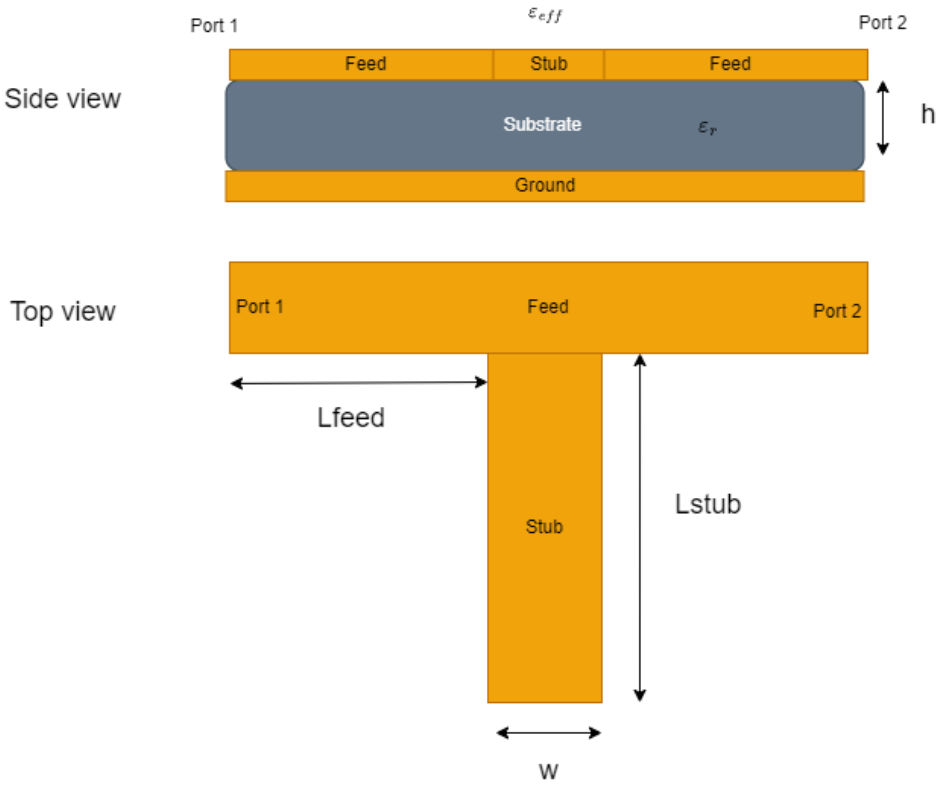

Figure 7.1: The general design of a microstrip T-resonator.

In figure 7.1 the design of a microstrip T-resonator is shown. The microstrip T-

resonator, among many other microstrip resonators, has been used for determining dielectric properties of materials for both high and low dielectric materials (10). Typically, solid substrates have been studied (9; 57), but records of characterising fluids may also be found(58). The strength of the microstrip resonators lies in the simplicity of use, where the sample only must be close to high energy dense areas of the resonator. For the T-resonator, the highest energy density is found at the end of the stub of the resonator, and the samples are thus optimally placed there. Traditionally, most articles attempt to determine the dielectric properties of the substrate between the resonator and the ground, i.e., ϵ_r, as most field strength is concentrated between the two. In another attempt, a jack was created directly adjacent to the end of the stub and filled with the material under test (58). A more interesting attempt is instead found in (9), where the area over the T-resonator, which otherwise is assumed to be air, was used to determine the dielectric properties of placed material.

While the dielectric constant in many cases may not be of interest to the pharmaceutical industry, it may be used to derive other quantities by using similar equations as described in equation 3.5. Additionally, if enough good quality experiments have been conducted and corresponding data have been stored, regression analysis can be used to estimate several characteristics of the samples from a collected spectrum, and could thus potentially be used for e.g., quality controls.

7.1.1 Aim of project

The aim is to investigate the possibility of using a T-resonator as a means to characterise the properties of samples. Properties could include density, porosity, humidity, and other possible parameters of interest.

7.2 Theory

Only a few equations are enough to design the T-resonator and will be provided here. We will assume the T-resonator to operate on the frequency f. The following equations assume that the material over the T-resonator is air (and thus loss-less), and thus the subject of interest is the substrate permittivity. From (10)

$$\epsilon_{eff} = \frac{\epsilon_r + 1}{2} + \frac{\epsilon_r - 1}{2} \frac{1}{\sqrt{1 + 12h/w}}, \tag{7.1}$$

$$Z_0 = \begin{cases} \frac{60}{\sqrt{\epsilon_{eff}}} ln\left(\frac{8h}{w} + \frac{w}{4h}\right) & \text{for } w/h \leq 1 \\ \frac{120\pi}{\sqrt{\epsilon_{eff}}[w/h + 1.393 + 0.667 ln(w/h + 1.444)]} & \text{for } w/h \geq 1 \end{cases}. \tag{7.2}$$

Here ϵ_{eff} is the effective permittivity describing the air over the microstrip and the dielectric of the substrate, ϵ_r is the substrate relative permittivity, Z_0 the characteristic impedance, w the width of the microstrip and h the thickness of the substrate. All variables are outlined in figure 7.1. Typically, we wish to have a specific characteristic impedance (50 Ω), and the substrate relative dielectric constant is already

known, in which the ratio w/h can be determined using

$$\frac{w}{h} = \begin{cases} \frac{8e^A}{e^{2A}-2} & \text{for } w/h < 2 \\ \frac{2}{\pi}\left[B - 1 - ln(2B-1) + \frac{\epsilon_r+1}{2\epsilon_r}\left\{ln(B-1) + 0.39 - \frac{0.61}{\epsilon_r}\right\}\right] & \text{for } w/h > 2 \end{cases} \tag{7.3}$$

where

$$A = \frac{Z_0}{60}\sqrt{\frac{\epsilon_r+1}{2}} + \frac{\epsilon_r - 1}{\epsilon_r + 1}\left(0.23 + \frac{0.11}{\epsilon_r}\right)$$
$$B = \frac{377\pi}{2Z_0\sqrt{\epsilon_r}}.$$

The above equations give us enough information to build our T-resonator, in which we assume 50 Ω characteristic impedance, and use a 3D printed substrate with relative permittivity. We then use equation 7.3 to determine the ratio of the thickness of the substrate and width of the microstrip. The equations

$$L_{stub} = (2n+1)\frac{c}{4f\sqrt{\epsilon_{eff}}}, \quad L_{feed} = 2L_{stub},\ n = 0, 1, 2, ... \tag{7.4}$$

are then used to determine the length of the stub and feed.

7.3 Previous work

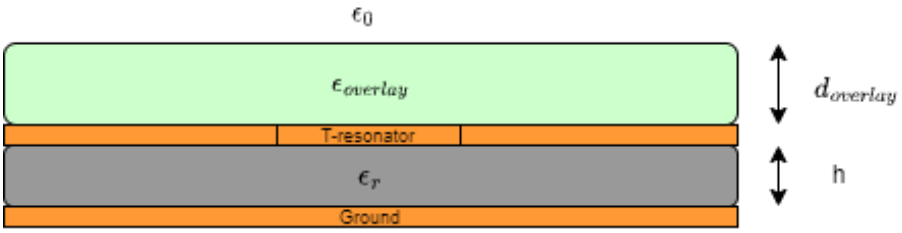

Figure 7.2: T resonator with overlay.

There are numerous articles considering the uses of the microwave T-resonator for determining dielectric properties of samples (10; 57; 58). Most cases assume the material over the microstrip to be air, which simplifies the governing equations to the above equations(10). Thus, the substrate and materials between the microstrip and ground may be determined. The downside of this approach is that the substrate is not straightforwardly exchangeable, and thus several steps are required when changing materials under test. In (58) they attempted to solve this issue by removing one part of the substrate with a microfluid system. This, of course, limits the analysis to fluids and may result in clogging issues depending on the tested fluid. In another attempt, by (9), the substrate was kept as is but the region over the microstrip was used to determine the permittivity of the samples. The effective permittivity, ϵ_{eff}, thus is perturbed and can be used as the means of measure. Although it also renders

the above equations invalid which the authors of (9) did not account for. Instead, they fitted their data to some known values.

In the publication (59) the dielectric effect of overlying materials was derived for either a homogeneous material completely substituting the air, or a thin material over the microstrip (not necessarily a T-resonator) covered by air. In figure 7.2 the approach which (59) developed, but instead using the T-resonator is shown. The equation of effective permittivity (eq.7.1) becomes several times more complex but still is offered with simple equations where integration and similar operations are avoided. As such, we estimate the effective permittivity by (59),

$$\epsilon_{eff} = \frac{\epsilon_r + \epsilon_o}{2} + k_1(\epsilon_r - \epsilon_o)s(\overline{w})Corr(\overline{w}, \epsilon_r, \epsilon_o) \tag{7.5}$$

where

$$s(\overline{w}) = \begin{cases} \left(1 + \frac{12}{\overline{w}}\right)^{-1/2} & \text{for } \overline{w} \geq 1 \\ \left(1 + \frac{12}{\overline{w}}\right)^{-1/2} + 0.04(1 - \overline{w}) & \text{for } \overline{w} < 1, \end{cases}$$

$$Corr(\overline{w}, \epsilon_r, \epsilon_o) = \begin{cases} 1 & \text{for } \epsilon_r \geq \epsilon_o \\ \left(\frac{\epsilon_o}{\epsilon_r}\right)^{ExpCorr(\overline{w})} & \text{for } \epsilon_r < \epsilon_o, \end{cases}$$

$$ExpCorr(\overline{w}) = \begin{cases} \frac{k_2}{\overline{w}^{k_3} + k_4} & \text{for } \overline{w} \leq 2 \\ \frac{k_5}{\overline{w}^{k_6} + k_7} & \text{for } \overline{w} > 2, \end{cases}$$

$$\epsilon_o = \begin{cases} 1 + \frac{2}{\pi}(\epsilon_{overlay} - 1)arctan\left(k_8 \overline{d}^{k_9} \overline{w}^{k_{10}}\right) & \text{for } \overline{w} \geq 1 \\ 1 + \frac{2}{\pi}(\epsilon_{overlay} - 1)arctan\left(k_{11} \overline{d}^{k_{12}} \overline{w}^{k_{13}}\right) & \text{for } \overline{w} < 1, \end{cases}$$

$$\overline{w} = \frac{w}{h}, \quad \overline{d} = \frac{d_{overlay}}{h}.$$

The parameters $k_i,\ i = 1, 2, ..., 13$ are best fit parameters, and the author estimated them to be

$$\{k_i\} = \{0.52, 0.241, 0.715, 0.446, 1.814, 1.798, 12.52, 1.877, 0.904, 0.367, 1.782, 0.782, 0.214\}$$

under the assumptions

$$0 < \overline{w} \leq 10, \quad \frac{\epsilon_{overlay}}{\epsilon_r} \leq 10.$$

7.4 Method

Using the above equations, we can combine them with the presented equations in 4.3 to derive quantities such as porosity or humidity. Given the operational frequency, f_{op}, we thus design the T-resonator (assuming the overlay material is

air => $\epsilon_{overlay} = \epsilon_0$) using equations 7.1, 7.3 and 7.4 to determine the height of substrate, the width of microstrip and stub length and feed length. Using the VNA, we determine the real resonant frequency f_0, which optimally should be the same as the operational frequency but may differ due to practical implementation. The difference between analytical and measured frequency, $\Delta f = f_{op} - f_0$ is stored and will be used to shift measured frequencies to corresponding theoretical values. Knowing the length of the stub, and being able to measure the resonant frequency, we again use equation 7.4 but this time to retrieve ϵ_{eff}. Equation 7.5 with subsequent equations is then used to determine ϵ_o by gradient descent, which then is used to find $\epsilon_{overlay}$ using equation 7.3. Samples are optimally placed over the whole microstrip, which may not be feasible and can thus be placed on the end of the stub where the energy density is the largest (9).

To determine the fractional porosity two factors are required to be known, both the effective permittivity but also the real permittivity of the sample. One way to accommodate this is to first derive the porosity of the sample by other means and then determine the permittivity of the sample. This value is then used to estimate the porosity of subsequent samples, using the known permittivity.

Finally, we will use an operational frequency of 2.47 GHz, and the substrate will be of ABS material (dielectric constant of 2.7-3.2). For practical reasons, the height of the substrate was set to 1 mm, in which the microstrip should be around 2.5 mm wide for a characteristic impedance of 50 Ω. The length of the stub should be around 2 cm, and the feed can be set to around 2 cm. The dimensions of the substrate should thus at a minimum be a 4 by 4 cm^2 square. The constructed resonator is shown in figure 7.3, and was made using copper tape, cutting, and soldering. Several different versions were constructed, but the presented one coupled best to the theoretical value.

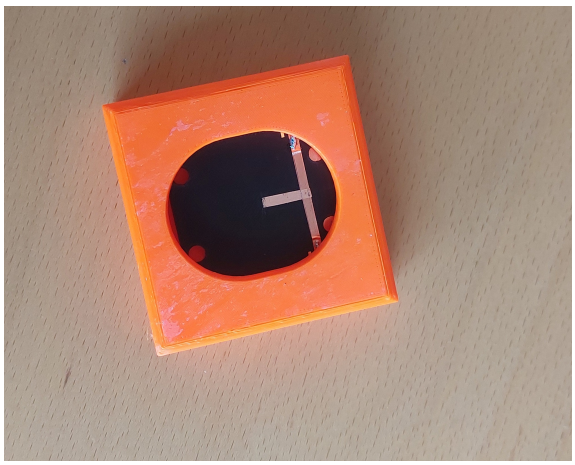

Figure 7.3: Realisation of one of the T-resonators. The operation frequency is at 4.8 GHz. Covering the T-resonator is a 3D-printed 'shell' to add stability to the construction.

7.4.1 Experiments

Initial experiments using materials of known dielectric properties, such as water were conducted to validate the methods or non-fluids such as MCC. Porosity was then tested by compressing MCC and other substances to tablets, only altering the pressure excited by the compressor.

7.5 Results

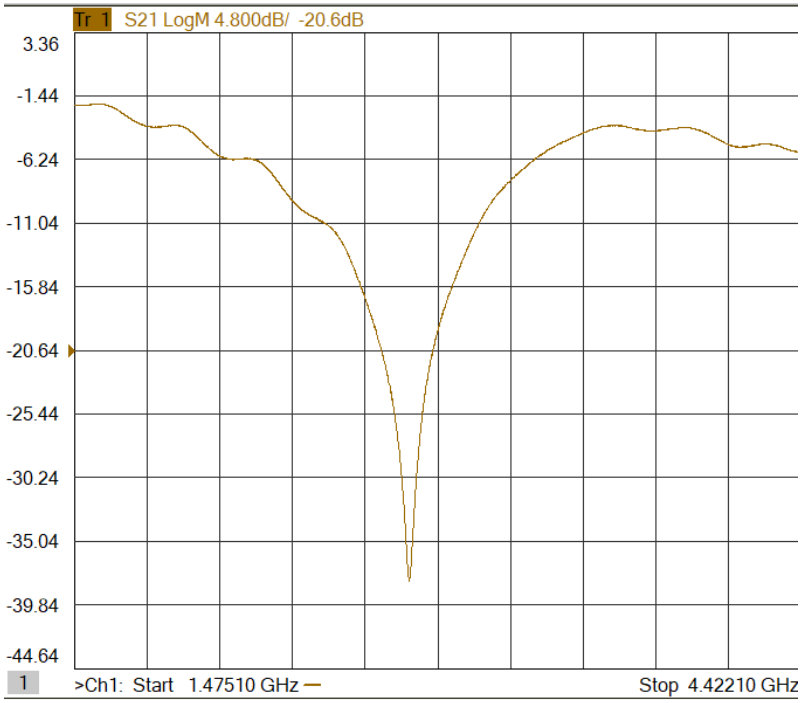

Figure 7.4: S21 parameter of the 2.47 GHz resonator. The measured resonant frequency was found at 2.87 GHz.

In figure 7.4 the resonance of the 2.45 GHz resonator is shown. The measured resonance frequency was found around 2.87 GHz, and thus quite off the desired frequency. Additionally, the bandwidth was a bit larger than expected, thus leaving much to be improved regarding the construction of the T-resonator. Several attempts, as well as other designs/constructions, were tested but most had equal or worse performance. Nevertheless, the 2.47 GHz construction was used for various experiments.

Several dielectric constants for various materials, such as water (~ 80) and MCC (~ 2.25) (60) could be reconstructed with $\pm 10\%$ accuracy (water: 72-93 depending on the container used; MCC: 0.7-3 depending on amount and placement), leaving much to be desired. The experiment of (9) was also conducted, in which the regression similar to above was in the 10 % error range, but the tendency of the curve was observed. Since the specificity was considerably low for the constructions, but not entirely off, there is most likely a need for improving the construction of the T-resonator. An attempt to create the microstrips on printed boards using copper

etching methods to increase the stability and design of the T-resonator was initialised but never completed. Instead, other works were prioritised.

7.6 Discussion and conclusion

A sufficiently good T-resonator was never constructed, and current constructs need improvement on several levels. Nevertheless, the T-resonator indicated on having potential for several characteristics of samples, in which the equations relating the spectrum to sample characteristics are simple and straightforward to implement. We also note that the equations are not limited to the T-resonator, but other microstrip resonators, such as ring resonators may also be used.

An interesting realisation during the project is that microstrip antennas can also be used in flows, such as the ones studied in cases I or II. For instance, a ring resonator was incorporated into a fluid bed to measure the quality of the granules in a fluid bed (36) and could likewise be used for other types of flows. The advantage of using microstrips instead of the probes used in Case I-III is that it may more easily be protected from the process, as it is flat. The disadvantage is instead the 'reach', in which it measures local effect and not changes on a global (in the sense of the process machine) scale.

In conclusion, while the current study is lacking in several aspects, we have composed a simple framework of equations for microstrips, in which it is possible to characterise and quantify samples non-destructively. The samples are simply placed on top of the microstrip and removed when a spectrum has been saved, enabling quick and simple analysis protocols.

8

General discussion and Conclusion

In the current thesis, microwaves as a tool in the pharmaceutical industry have been validated for four different processes or areas, presented as cases I-IV. The cases were chosen based on whether they were already commercialised or not, and the progression of the projects as a whole. Non-commercialised in early stage development projects were then prioritised. Theory as well as previous work within the areas have been reviewed and presented, and improvements of each case have been both discussed and attempted to various degrees. Specifically, in case I and II a microwave monitor/sensor method have been developed for sensing particles either flowing through a pipe or floating in the air in a fluid bed. For case III an electroporation protocol using microwaves has been reviewed, revised, and implemented using a similar but yet different method. For case VI a T-resonator was investigated to characterise samples. Due to time limitations and low initial progress case III and VI was concluded early with only a few experiments, although the theoretical framework for each case was completed.

A special case of interest in this study has been the cavity resonator, which may be viewed as a microwave oven capable of both heating, electroporating, and monitoring samples inside the cavity walls. Thus it may find several use cases in many different processes within the industry. The theory behind the cavity resonator has been presented, and means to gain numerical results using open-source software have been provided. The cavity resonator has been shown to have the possibility to extract sufficiently specific information as a means to monitor processes. As such a better fit, and easier to construct, the fourth case could be to use the cavity resonator to characterise samples. On the contrary, microstrip antennas such as the one used in case IV can both be more stable, robust, and provide more specific information for a local area of the system.

All analysis, control of devices and automation have been accomplished using open-source softwares, as to make the process of continuing the current thesis easier. Open-source software used in this thesis includes but is not limited to ElmerFEM, FreeCAD, Paraview, GMSH, Salome, GNURadio, and Python. Especially python has been used to control devices such as the VNA, SDR, and Thorlab motion devices but also to perform data analysis and plotting. We note that the use of Elmer was difficult at first since many electromagnetic modules have not been properly implemented on all fronts. The use of eigensolutions for instance was only possible

close to three months before the end of the thesis, as a new release then had the feature. Similarly, some devices only allowed restricted use of Python. To the author's best knowledge, the electromagnetic modules of Elmer are in development and many features and possibilities, in addition to the already broad and exhaustive usefulness, may soon be available. Nevertheless, it has been displayed in this thesis that open-source software can be as good as commercial tools in some cases, and may be interchangeably used.

Regression methods have been derived accommodating for complex signal processing of improper signals, which can be used in several more cases than what has been used in this thesis. The results have shown that circular-symmetric regression methods may inaccurately predict the imaginary part for real-valued dependent variables, but may in general be better than the corresponding widely linear version. This observation is based on as it seems the widely linear accumulates the noise from both the real and imaginary parts, while if the imaginary prediction of the circular-symmetric prediction is neglected it is more stable.

As the final remark, microwaves, while already firmly established in the pharmaceutical industry, have yet to explore its full capabilities within several areas or processes. We thus conclude the thesis highlighting that one of the main contributions of the thesis is the framework for a simple, early stage analysis of relations between complex-valued data (such as scatter parameters) to quantitative measures. This framework can then be used in several, non-adjacent applications for quick analysis; enabling a simple way to overview analysis possibilities of different pharmaceutical processes.

Bibliography

[1] Bonde, M., Sohani, A., Daud, A. & Sapkal, N. Microwave: An emerging trend in pharmaceutical processes and formulations. *International Journal Of Pharmacy And Technology*. **3** pp. 3499-3520 (2011,9)

[2] Kappe, C. & Dallinger, D. The impact of microwave synthesis on drug discovery. *Nature Reviews Drug Discovery*. **5**, 51-63 (2005,12), https://doi.org/10.1038/nrd1926

[3] Aram, M., Aliakbarian, H. & Trefná, H. An ultra-wideband compact design for hyperthermia: Open ridged-waveguide antenna. *IET Microwaves, Antennas & ; Propagation*. **16**, 137-152 (2022,1), https://doi.org/10.1049/mia2.12226

[4] Singh, S., Gupta, D., Jain, V. & Sharma, A. Microwave Processing of Materials and Applications in Manufacturing Industries: A Review. *Materials And Manufacturing Processes*. **30**, 1-29 (2014,11), https://doi.org/10.1080/10426914.2014.952028

[5] Nohlert, J., Electrical Engineering, Chalmers & Högskola, C. Microwave Measurement Techniques for Industrial Process Monitoring and Quality Control. (Chalmers University of Technology,2018)

[6] Cerullo, L., Siganals and Systems, Chalmers & Högskola, C. Microwave Measurement Systems for In-line 3D Monitoring of Pharmaceutical Processes. (Chalmers University of Technology,2013)

[7] Schmidt, S., Schubler, M., Hessinger, C., Schuster, C., Bertulat, B., Kithil, M., Cardoso, M. & Jakoby, R. Microwave Induced Electroporation of Adherent Mammalian Cells at 18 GHz. *IEEE Access*. **7** pp. 78698-78705 (2019), https://doi.org/10.1109/access.2019.2923073

[8] Ahortor, E., Malyshev, D., Williams, C., Choi, H., Lees, J., Porch, A. & Baillie, L. The biological effect of 2.45 GHz microwaves on the viability and permeability of bacterial and yeast cells. *Journal Of Applied Physics*. **127**, 204902 (2020,5), https://doi.org/10.1063/1.5145009

[9] Alahnomi, R., Zakaria, Z., Yussof, Z., Sutikno, T., Sariera, H. & Bahar, A. Accurate characterizations of material using microwave T-resonator for solid sensing applications. *TELKOMNIKA (Telecommunication Computing Electronics And Control)*. **18**, 99 (2020,2), https://doi.org/10.12928/telkomnika.v18i1.14880

[10] Pozar, D. Microwave Engineering 4ed. (2011,11)

[11] Nasserdine, M., Mengue, S., Bourcier, C. & Richalot, E. Field measurements within a large resonant cavity based on the perturbation theory. *Prog. Electromagn. Res. B Pier B.* **57** pp. 1-20 (2014)

[12] Zhang, H., Zeng, B., Ao, L. & Zhang, Z. A novel dual-loop coupler for one-port cylindrical cavity permittivity measurement. *Electromagn. Waves (Camb.).* **127** pp. 537-552 (2012)

[13] Collins, T., Getz, R., Pu, D. & Wyglinski, A. Software-Defined Radio for Engineers. (Artech House,2018,5)

[14] Yogesh B. Gianchandani, O. & Zappe, H. Comprehensive Microsystems. (Elsevier,2010)

[15] Gallager, R. Circularly-Symmetric Gaussian random vectors. (2008)

[16] Schreier, P. & Scharf, L. Second-order analysis of improper complex random vectors and processes. *IEEE Transactions On Signal Processing.* **51**, 714-725 (2003)

[17] Schreier, P. & Scharf, L. Statistical Signal Processing of Complex-Valued Data. (Cambridge University Press,2010,2), https://doi.org/10.1017/cbo9780511815911

[18] Delmas, J. & Abeida, H. On the degree of second-order non-circularity of complex random variables. *2008 IEEE International Conference On Acoustics, Speech And Signal Processing.* pp. 3905-3908 (2008)

[19] Von Hippel, A. Dielectric Materials and Applications: Papers by Twenty-two Contributors. *Technology Press Books In Science And Engineering.* (1954), https://books.google.se/books?id=XRhRAAAAMAAJ

[20] Penn, S., Alford, N., Templeton, A., Wang, X., Xu, M., Reece, M. & Schrapel, K. Effect of Porosity and Grain Size on the Microwave Dielectric Properties of Sintered Alumina. *Journal Of The American Ceramic Society.* **80**, 1885-1888 (2005,1), https://doi.org/10.1111/j.1151-2916.1997.tb03066.x

[21] Shi, S., Gao, Y., Zhang, Y. & Zhao, J. A Novel Microwave Humidity Sensor Based on Resonant Cavity Perturbation Method. *IEEE Sensors Journal.* **22**, 22571-22581 (2022)

[22] Papaioannou, A. Component analysis of complex-valued data for machine learning and computer vision tasks. (Imperial College London,2017), DOI: https://doi.org/10.25560/49235

[23] Stott, A., Kanna, S. & Mandic, D. Widely linear complex partial least squares for latent subspace regression. *Signal Processing.* **152** pp. 350-362 (2018,11), https://doi.org/10.1016/j.sigpro.2018.06.018

[24] Baumann, M., Moody, T., Smyth, M. & Wharry, S. A Perspective on Continuous Flow Chemistry in the Pharmaceutical Industry. *Organic Process Research Development.* **24**, 1802-1813 (2020,1), https://doi.org/10.1021/acs.oprd.9b00524

[25] Burange, A., Osman, S. & Luque, R. Understanding flow chemistry for the production of active pharmaceutical ingredients. *IScience.* **25**, 103892 (2022), https://www.sciencedirect.com/science/article/pii/S2589004222001626

[26] Alidoustaghdam, H. & Çayören, M. Flow monitoring by microwave imaging inside a cuboid cavity: Theory and numerical feasibility analysis. *Flow Measurement And Instrumentation.* **82** pp. 102051 (2021,12), https://doi.org/10.1016/j.flowmeasinst.2021.102051

[27] Gao, Y., Ravan, M. & K. Amineh, R. Fast, Robust, and Low-Cost Microwave Imaging of Multiple Non-Metallic Pipes. *Electronics.* **10** (2021), https://www.mdpi.com/2079-9292/10/15/1762

[28] Zhan, M., Xie, C. & Shu, J. Microwave probe sensing location for Venturi-based real-time multiphase flowmeter. *Journal Of Petroleum Science And Engineering.* **218** pp. 111027 (2022,11), https://doi.org/10.1016/j.petrol.2022.111027

[29] Buschmüller, C., Wiedey, W., Döscher, C., Dressler, J. & Breitkreutz, J. In-line monitoring of granule moisture in fluidized-bed dryers using microwave resonance technology. *European Journal Of Pharmaceutics And Biopharmaceutics.* **69**, 380-387 (2008), https://www.sciencedirect.com/science/article/pii/S0939641107003256

[30] Foroughi-Dahr, M., Mostoufi, N., Sotudeh-Gharebagh, R. & Chaouki, J. Particle Coating in Fluidized Beds. *Reference Module In Chemistry, Molecular Sciences And Chemical Engineering.* (2017), https://www.sciencedirect.com/science/article/pii/B9780124095472122061

[31] Buschmüller, C. In-line monitoring of granule moisture in fluidized bed granulators using microwave resonance technology as novel PAT tool. (2010)

[32] Aghbashlo, M., Sotudeh-Gharebagh, R., Zarghami, R., Mujumdar, A. & Mostoufi, N. Measurement techniques to monitor and control fluidization quality in fluidized bed dryers: A review. *Dry. Technol.*. **32**, 1005-1051 (2014,7)

[33] Peters, J., Teske, A., Taute, W., Döscher, C., Höft, M., Knöchel, R. & Breitkreutz, J. Real-time process monitoring in a semi-continuous fluid-bed dryer - microwave resonance technology versus near-infrared spectroscopy. *Int. J. Pharm.*. **537**, 193-201 (2018,2)

[34] Lin, Y., Yang, W., Wu, Z. & Wang, H. Monitoring of high-moisture content particle drying in a fluidized bed by microwave and capacitance tomographic sensors. *Dry. Technol.*. **40**, 1153-1167 (2022,5)

[35] Cuenca, J., Slocombe, D. & Porch, A. Temperature correction for cylindrical cavity perturbation measurements. *IEEE Trans. Microw. Theory Tech.*. **65**, 2153-2161 (2017,6)

[36] Peters, J. Multi-resonance Microwave Sensors for Moisture Monitoring in Fluid-bed Processes. (2019), https://www.semanticscholar.org/paper/Multi-resonance-Microwave-Sensors-for-Moisture-in/482988102a977354686cb29d409e9c77ac521850

[37] Milacic, E., Nunez Manzano, M., Madanikashani, S., Heynderickx, G., Van Geem, K., Van de Greef, A., Richter, A., Kriebitzsch, S., Buist, K., Baltussen, M. & Kuipers, J. Experimental study on the temperature distribution in fluidised beds. *Chemical Engineering Science*. **248** pp. 117062 (2022), https://www.sciencedirect.com/science/article/pii/S0009250921006278

[38] Sukharev, S., Klenchin, V., Serov, S., Chernomordik, L. & YuA, C. Electroporation and electrophoretic DNA transfer into cells. The effect of DNA interaction with electropores. *Biophysical Journal*. **63**, 1320-1327 (1992,11), https://doi.org/10.1016/s0006-3495(92)81709-5

[39] Harvard Bioscience Inc., B. BTX ECM manual.. (2011), https://www.btxonline.com/media/wysiwyg/tab_content/BTX-ECM-830-User-Manual-0818.pdf, Accessed 2022.07.03

[40] Li, H., Ma, X., Du, X., Li, L., Cheng, X. & Hwang, J. Correlation Between Optical Fluorescence and Microwave Transmission During Single-Cell Electroporation. *IEEE Transactions On Biomedical Engineering*. **66**, 2223-2230 (2019,8), https://doi.org/10.1109/tbme.2018.2885781

[41] Krassowska, W. & Filev, P. Modeling Electroporation in a Single Cell. *Biophysi-*

cal Journal. **92**, 404-417 (2007,1), https://doi.org/10.1529/biophysj.106.094235

[42] Chen, C., Smye, S., Robinson, M. & Evans, J. Membrane electroporation theories: a review. *Medical & Biological Engineering & Computing*. **44**, 5-14 (2006,2), https://doi.org/10.1007/s11517-005-0020-2

[43] Sachdev, S., Muralidharan, A., Choudhary, D., Perrier, D., Rems, L., Kreutzer, M. & Boukany, P. DNA translocation to giant unilamellar vesicles during electroporation is independent of DNA size. *Soft Matter*. **15**, 9187-9194 (2019), https://doi.org/10.1039/c9sm01274e

[44] Sweeney, D., Weaver, J. & Davalos, R. Characterization of Cell Membrane Permeability In Vitro Part I: Transport Behavior Induced by Single-Pulse Electric Fields. *Technology In Cancer Research And Treatment*. **17** pp. 153303381879249 (2018,1), https://doi.org/10.1177/1533033818792491

[45] Kim, R. & S. A. Korchagin and Mathematical and computer simulation of the electrophysical properties of a multicellular structure exposed to nanosecond electrical pulses. *Izvestia Of Saratov University. New Series. Series: Mathematics. Mechanics. Informatics*. **21**, 259-266 (2021,5), https://doi.org/10.18500/1816-9791-2021-21-2-259-266

[46] Sengel, J. & Wallace, M. Imaging the dynamics of individual electropores. *Proceedings Of The National Academy Of Sciences*. **113**, 5281-5286 (2016,4), https://doi.org/10.1073/pnas.1517437113

[47] Jordan, C., Neumann, E. & Sowers, A. Electroporation and Electrofusion in Cell Biology. (Kluwer Academic/Plenum,1989,5)

[48] Gentet, L., Stuart, G. & Clements, J. Direct Measurement of Specific Membrane Capacitance in Neurons. *Biophysical Journal*. **79**, 314-320 (2000), https://www.sciencedirect.com/science/article/pii/S000634950076293X

[49] Babbs, C. & Shi, R. Subtle Paranodal Injury Slows Impulse Conduction in a Mathematical Model of Myelinated Axons. *PLoS ONE*. **8**, e67767 (2013,7), https://doi.org/10.1371/journal.pone.0067767

[50] Foster KR, Bidinger JM & Carpenter DO. The electrical resistivity of cytoplasm. *Biophys J.*. 1976 Sep;16(9):991-1001. doi: 10.1016/S0006-3495(76)85750-5. PMID: 963211; PMCID: PMC1334940.

[51] Chaparro, C., Herrera, L., Melendez, A. & Miranda, D. Considerations on

electrical impedance measurements of electrolyte solutions in a four-electrode cell. *Journal Of Physics: Conference Series*. **687** pp. 012101 (2016,2)

[52] Echave, P., Conlon, I. & Lloyd, A. Cell size regulation in mammalian cells. *Cell Cycle*. **6**, 218-224 (2007,1)

[53] Hu, Q., Hossain, S. & Joshi, R. Analysis of a dual shock-wave and ultrashort electric pulsing strategy for electro-manipulation of membrane nanopores. *Journal Of Physics D: Applied Physics*. **51**, 285403 (2018,6), https://doi.org/10.1088/1361-6463/aaca7a

[54] Gehl, J. Electroporation: theory and methods, perspectives for drug delivery, gene therapy and research. *Acta Physiologica Scandinavica*. **177**, 437-447 (2003,3), https://doi.org/10.1046$%5C%25$2Fj.1365-201x.2003.01093.x

[55] Wegner, L., Frey, W. & Silve, A. Electroporation of DC-3F Cells Is a Dual Process. *Biophysical Journal*. **108**, 1660-1671 (2015,4), `https://doi.org/10.1016\protect\T1\textdollar%5C%25\protect\T1\textdollar2Fj.bpj.2015.01.038`

[56] David H. Staelin. ELECTROMAGNETICS AND APPLICATIONS. *Massachusetts Institute of Technology*, Online text, retrieved: (04,09,2023), URL: `https://phys.libretexts.org/Bookshelves/Electricity_and_Magnetism/Electromagnetics_and_Applications_(Staelin)`

[57] Amey, D. & Curilla, J. Microwave properties of ceramic materials. *1991 Proceedings 41st Electronic Components Technology Conference.*, https://doi.org/10.1109/ectc.1991.163888

[58] Conchouso Gonzalez, D., Mckerricher, G., Castro, D., Arevalo Carreno, A. & Foulds, I. Radio Frequency Resonator For Continuous Monitoring Of Parallel Droplet Microfluidic Systems. (2015,10)

[59] Barbuto, M., Alù, A., Bilotti, F. & Toscano, A. Characteristic impedance of a microstrip line with a dielectric overlay. *COMPEL: Int J For Computation And Maths. In Electrical And Electronic Eng.*. **32** (2013,11)

[60] Ning, T. (2007). Evaluation of a Microwave Sensor for Powder Process Control. *Department of Technology University of Gavle*. (Dissertation). Retrieved from `http://urn.kb.se/resolve?urn=urn:nbn:se:hig:diva-703`

[61] Collin, R. FOUNDATIONS FOR MICROWAVE ENGI-

NEERING, 2ND ED. (Wiley India Pvt. Limited,2007), https://books.google.se/books?id=coBpP2SLiZQC

[62] Matthès, M., Bromberg, Y., Rosny, J. & Popoff, S. Learning and Avoiding Disorder in Multimode Fibers. *Physical Review X.* **11** (2021,6), https://doi.org/10.1103/physrevx.11.021060

[63] Juris Vencels, Peter Råback, Vadims Geža, EOF-Library: Open-source Elmer FEM and OpenFOAM coupler for electromagnetics and fluid dynamics, SoftwareX, Volume 9, 2019, Pages 68-72, ISSN 2352-7110, `https://doi.org/10.1016/j.softx.2019.01.007`.

[64] `https://github.com/FreeCAD/FreeCAD/releases/tag/0.20.2`; Jürgen, Werner, Yorik, Abdullah, Bernd, sliptonic and WandererFan, FreeCAD: 3D parametric modeller, retrieved: 21 April 2023.

[65] `https://www.salome-platform.org/`; EDF and CEA, Salome: Numerical Simulation, retrieved: 21 April 2023.

[66] `http://www.elmerfem.org/blog/`; CSC - IT Center for Science, Elmer: open source multiphysical simulation software, retrieved 21 April 2023.

[67] `http://paraview.org`; Sandia National Labs, Kitware Inc, and Los Alamos National Labs. Paraview: Parallel visualization application, retrieved: 21 April 2023.

[68] Råback, P., Malinen, M., Ruokolainen, J., Pursula, A. & Zwinger, T. Elmer Models Manual. (CSC–ITCenterforScience, April 6, 2023)

[69] Råback, P., Malinen, M., Ruokolainen, J., Pursula, A., Mikko B., & Zwinger, T. Elmer Solver Manual. (CSC–ITCenterforScience, April 6, 2023)

[70] Muehlmann, U., Gebhart, M. & Wobak, M. Mutual coupling modeling of NFC antennas by using open-source CAD/FEM tools. *2012 IEEE International Conference On RFID-Technologies And Applications (RFID-TA).* pp. 393-397 (2012)

[71] Chekhovich, E. Keyhole Resonators for Subwavelength Focusing of Microwave Magnetic Fields in Optically Detected Electron Spin Resonance. *Phys. Rev. Appl..* **15**, 034082 (2021,3), https://link.aps.org/doi/10.1103/PhysRevApplied.15.034082

[72] Panchal, J. 3 Dimensional Electromagnetic Analysis of an Axial Active Magnetic Bearing. (Aalto University. School of Electrical Engineering,2016), http://urn.fi/URN:NBN:fi:aalto-201608263082

[73] Gustaver, M. (2020) A Chalmers University of Technology Master's thesis template for LaTeX. Unpublished.

A

PDEs and general derivations

Following is a summary of the most important field equations, as well as some derivations necessary for understanding results. Most results can easily be derived or found online. These equations follows closely, but ultimately takes my own spin on derivations found in David Pozar's book microwave engineering (10).

A.1 Time-harmonic Maxwell's equations

In electromagnetic filed theories, typically any derivation originates from Maxwells equations,

$$\vec{\nabla} \times \vec{E} = -\frac{\partial \vec{B}}{\partial t} - \vec{M}, \quad \vec{\nabla} \cdot \vec{D} = \rho \tag{A.1}$$

$$\vec{\nabla} \times \vec{H} = \frac{\partial \vec{D}}{\partial t} + \vec{J}, \quad \vec{\nabla} \cdot \vec{B} = 0 \tag{A.2}$$

$$\vec{D} = \epsilon \vec{E}, \quad \vec{J} = \sigma \vec{E}, \quad \vec{B} = \mu \vec{H}. \tag{A.3}$$

Here $\vec{E}$ is the electric field (V/m), $\vec{D}$ the electric flux density $(Coul/m^2)$, $\vec{H}$ the magnetic field (A/m), $\vec{B}$ the magnetic flux density (Wb/m^2), J the electrical current density (A/m^2), $\vec{M}$ the magnetic current density (V/m^2) and ρ the electric charge density (C/m^3). ϵ and μ where previously presented as the permittivity and permeability, respectively. Generally, ϵ and μ can both be considered as complex and tensors.

Typically it is useful to assume that both ϵ and μ are both time-independent, as well that the electric and magnetic fields are time-harmonic, i.e.

$$E = Ee^{jwt}$$
$$H = He^{jwt}.$$

Maxwell's equations may then be written as,

$$\vec{\nabla} \times \vec{E} = -jw\mu H - M, \quad \vec{\nabla} \cdot D = \rho \tag{A.4}$$
$$\vec{\nabla} \times \vec{H} = (jw\epsilon + \sigma)E, \quad \vec{\nabla} \cdot B = 0 \tag{A.5}$$
$$\tag{A.6}$$

A.1.1 Helmholtz equation

If we further assume that the region we are dealing with is source-free (e.g. $M = 0, \sigma = \rho = 0$), as well as isotropic and homogeneous (ϵ, μ constant) the equations would look like

$$\begin{aligned} \vec{\nabla} \times \vec{E} &= -jw\mu H, \quad \vec{\nabla} \cdot E = 0 \\ \vec{\nabla} \times \vec{H} &= jw\epsilon E, \quad \vec{\nabla} \cdot H = 0. \end{aligned} \tag{A.7}$$

I.e. an equation system with only two unknowns. By taking the curl of any of these while using the relationship

$$\vec{\nabla} \times \vec{\nabla} \times \vec{A} = \nabla(\vec{\nabla} \cdot A) - \nabla^2 A = -\nabla^2 A \quad \text{if } \vec{\nabla} \cdot A = 0$$

,

we end up with

$$\begin{aligned} -\nabla^2 E &= -jw\mu(jw\epsilon E) = w^2\epsilon\mu E \\ -\nabla^2 H &= jw\epsilon(-jw\mu H) = w^2\epsilon\mu H. \end{aligned}$$

Or, using the more usual form, we arrive at Helmholtz equation,

$$\begin{aligned} \nabla^2 E + w^2\epsilon\mu E &= 0 \\ \nabla^2 H + w^2\epsilon\mu H &= 0. \end{aligned} \tag{A.8}$$

Here one usually defines $k : k^2 = w^2\epsilon\mu$ as the propagation constant.

B

Extended theory

B.1 Coupling probe and antennas extended theory

A connection to the measuring instrumentation into the cavity is necessary, both to excite but also measure waves within the cavity. Typically, either the cavity is connected via a hole to a hollow waveguide, or a 'straight' antenna inserted to the cavity via a transmission line (called E-probe), or a bent antenna with its end short-circuited to ground (cavity wall) (called H-probe) (5). Other options such as PCB patches (11) or variations of loops (12) can also be found in litterateur. Following the reasoning of Nohlert (5), the H-probe is most suitable. This due to an 'hole' and patch would not be able to both send and receive, and an E-probe may be imposed to static voltages arising from triboelectic charging of material inside the cavity which in turn can be harmful to the instrumentation, for instance granules hitting the cavities wall (5). An H-probe is instead both inside the cavity and can both excite and measure, but is also short-circuited or grounded into the cavity walls which protects instrumentation.

An H-probe, or coupling loop, are mainly sensitive to time variations in the magnetic flux that passes through the loop (61). The equivalent circuit of a H-probe (note,

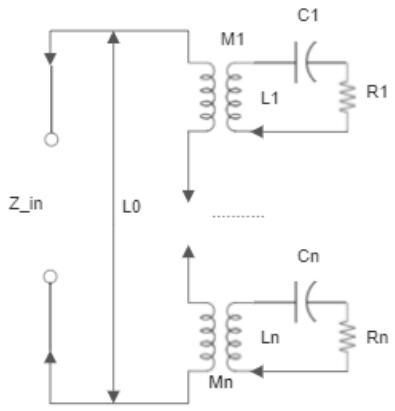

Figure B.1: Equivalent circuit of a H-Loop coupled to cavity resonator.

only one probe) to a resonant cavity can be seen in figure B.1. In such case the input impedance $Z_{in} = Z_{in}(w)$ is dependent on the mutual inductance's, M_n, of each and every resonant mode n, and each resonant mode can be viewed as an independent LCR circuit to the coupling loop. L_0 here is the self-inductance of the coupling loop. Defining resonant frequency as $\omega_n^3 L_n C_n = 1$ and the unloaded Q-value as $Q_n = \omega_n C_n / R_n$, the input impedance can thus be written as,

$$Z_{in} = j\omega L_0 + j \sum_{m=1}^{\infty} \frac{\omega^3 M_n^2}{L_n(\omega_n^2 - \omega^2 + j\omega\omega_n/Q_n)}. \tag{B.1}$$

If ω is not in the vicinity of the n'th resonant frequency, the n'th term's denominator in equation B.1 will grow, and the term vanishes. Thus for $\omega \approx \omega_n$, we may remove all terms where $m \neq n$ and we have approximately only one single LCR-circuit left (61). This bases on the assumption that the resonant frequencies $\omega_n,\ n = 1, 2, ...$ are well separated, thus in the lower regions in the density plot in figure 2.2.

Now, lets consider two antennas. If we only consider one resonant frequency, we have essentially two LCR circuits coupled to another LCR circuit by respective mutual inductanceses $M^{(1)}$, $M^{(2)}$, impedances $Z^{(1)}, Z^{(2)}$ and voltages $U^{(1)}, U^{(2)}$. Thus, we can correlate the scatter parameters with the LCR circuit as (5),

$$\begin{aligned}
S_{21} &= \frac{U^{(2)}}{U^{(2)}} = \frac{K}{1 + jQ\xi} \\
S_{11} &= \frac{Z(w) - Z_0}{Z(w) + Z_0} = \frac{\beta_1 - \beta_2 - 1 - jQ_u\xi}{\beta_1 + \beta_2 + 1 + jQ_u\xi} \\
S_{22} &= \frac{\beta_2 - \beta_1 - 1 - jQ_u\xi}{\beta_1 + \beta_2 + 1 + jQ_u\xi} \\
K &= \frac{2\sqrt{\beta_1\beta_2}}{1 + \beta_1 + \beta_2} \\
Q &= \frac{Q_u}{1 + \beta_1 + \beta_2} \\
\beta_i &= \frac{(wM^{(i)})^2}{RZ_0} \\
Q_u &= \frac{1}{w_0 RC} \\
\xi &= \frac{w}{w_0} - \frac{w_0}{w}
\end{aligned}$$

Finally, two important inquiries can still be made of the the design of such antennas, namely what size or length it should have, and where the probe should be located. In short, the H-probe as it should be coupled against the magnetic fields rather than the electric field, is optimally placed in a resonant area (bright areas in figure 2.1a)) for the lowest (fundamental) mode of the cavity to optimally transfer energy into the system. Similarly, it should be placed in a the same area as the strongest magnetic field passing through there, which is then measured. The length of the probe can be set at quarter wavelength of the fundamental resonant frequency, for intermediate

impedance matching between the two systems (instrument + antenna vs cavity). (61) While this set-up favours the fundamental resonant frequency more so than for the others, it still provides analytical feasible measurements for other frequencies as we will see later. Also, it may be that in practical situations the H-probe cannot be located in the fundamental resonant frequency magnetic field-peak, as such lower frequency modes could instead be used in a similar fashion.

A last note for the reader; above we made the assumption that $\mu_r \approx 1$, but $\epsilon_r \neq 1$ for any material under study inside the cavity. Essentially, this means that while we study changes in the magnetic field, the material causes perturbations in the electric field and hence the magnetic field as described by Maxwell's equations, while it causes no "direct" changes to magnetic field. The strongest measured change within the cavity for a given resonant frequency is then when the material under study is in a peak electric field location (left cylinder in 2.1a)), but the H-probe is located at one of the peaks of the magnetic field (right cylinder in 2.1a)).

C

Cylinder cavity resonator

A cylinder cavity resonator is a well studied subject, and serves as a both good example but also as an easy starting point before advancing to more difficult cavities, such as the fluid bed dryer. The cylinder cavity have known field solutions, and can serve as both as a reference point, but also as a quick testing and development object in early development.

C.1 Setup and equations

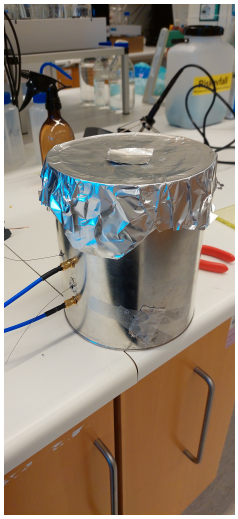

(a) Cylinder cavity with H-probes.

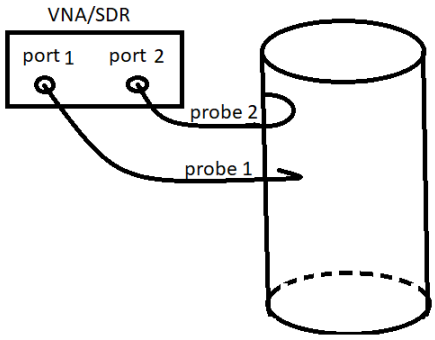

(b) Cylinder cavity connected to VNA, skiss.

Figure C.1: Cylinder cavity, skiss (a) and real (b).

The equations for a cylinder cavity is well known, and the derivation is straightforward. The boundaries of the cylinder can be assumed to be PEC boundaries, while the inner part is assumed to be lossless air with permittivity ϵ_0. As such in the inner part of the cavity, we can make an isotropic, homogeneous assumption. Variations on how the following steps here progress differs depending on the author, but generally assuming $\hat{z}$ propagation of the waves and solving either one of equations 2.7 in cylindrical coordinates, to gain either E or H, and using the 'other' equation A.7 to solve for the other H or E. For instance, solve eq. 2.7 for E, then use the

first equation of eq. A.7 to solve for H. Here a important result arise; if E is solved for Helmholtz, then $H_z = \hat{z}H = 0$, and vice versa if solving Helmholtz for H. This holds, since H curls around E, and E curls around H (Maxwell's equations) which hence enforces either one to be zero, if the other is not. When $E_z = 0$, we say that the solutions belongs TE modes, and if $H_z = 0$ we say that the solutions belongs to TM modes.

The solutions for the cylinder cavity can be found in e.g. (10), and is,

TM modes:

$$(E_z)_{mnp} = E_0 J_m(\frac{x_{mn}}{a}r) \begin{Bmatrix} sin(m\phi) \\ cos(m\phi) \end{Bmatrix} cos(\frac{p\pi}{d}z) \tag{C.1}$$

$$(E_r)_{mnp} = \frac{-E_0}{x_{mn}/a}\frac{p\pi}{d} J'_m(\frac{x_{mn}}{a}r) \begin{Bmatrix} sin(m\phi) \\ cos(m\phi) \end{Bmatrix} sin(\frac{p\pi}{d}z) \tag{C.2}$$

$$(E_\phi)_{mnp} = \frac{-E_0}{(x_{mn}/a)^2}\frac{1}{r} m\frac{p\pi}{d} J_m(\frac{x_{mn}}{a}r) \begin{Bmatrix} cos(m\phi) \\ -sin(m\phi) \end{Bmatrix} sin(\frac{p\pi}{d}z) \tag{C.3}$$

$$(H_z)_{mnp} = 0 \tag{C.4}$$

$$(H_r)_{mnp} = \frac{-jw\epsilon E_0}{(x_{mn}/a)^2}\frac{m}{r} J_m(\frac{x_{mn}}{a}r) \begin{Bmatrix} cos(m\phi) \\ -sin(m\phi) \end{Bmatrix} cos(\frac{p\pi}{d}z) \tag{C.5}$$

$$(H_\phi)_{mnp} = \frac{-jw\epsilon E_0}{x_{mn}/a} J'_m(\frac{x_{mn}}{a}r) \begin{Bmatrix} sin(m\phi) \\ cos(m\phi) \end{Bmatrix} cos(\frac{p\pi}{d}z) \tag{C.6}$$

with resonant frequencies

$$(f)_{mnp} = \frac{c}{2\pi\sqrt{\mu_r\epsilon_r}}\sqrt{\left(\frac{x_{mn}}{a}\right)^2 + \left(\frac{p\pi}{d}\right)^2}. \tag{C.7}$$

TE modes:

$$(E_z)_{mnp} = 0 \tag{C.8}$$

$$(E_r)_{mnp} = \frac{iw\mu H_0}{(x'_{mn}/a)^2}\frac{m}{r} J_m(\frac{x'_{mn}}{a}r) \begin{Bmatrix} cos(m\phi) \\ -sin(m\phi) \end{Bmatrix} sin(\frac{p\pi}{d}z) \tag{C.9}$$

$$(E_\phi)_{mnp} = \frac{-iw\mu H_0}{x_{mn}/a} J'_m(\frac{x'_{mn}}{a}r) \begin{Bmatrix} sin(m\phi) \\ cos(m\phi) \end{Bmatrix} sin(\frac{p\pi}{d}z) \tag{C.10}$$

$$(H_z)_{mnp} = H_0 J_m(\frac{x'_{mn}}{a}r) \begin{Bmatrix} sin(m\phi) \\ cos(m\phi) \end{Bmatrix} sin(\frac{p\pi}{d}z) \tag{C.11}$$

$$(H_r)_{mnp} = \frac{H_0}{x_{mn}/a}\frac{p\pi}{d} J'_m(\frac{x'_{mn}}{a}r) \begin{Bmatrix} sin(m\phi) \\ cos(m\phi) \end{Bmatrix} cos(\frac{p\pi}{d}z) \tag{C.12}$$

$$(H_\phi)_{mnp} = \frac{H_0}{(x_{mn}/a)^2}\frac{p\pi}{d}\frac{m}{r} J_m(\frac{x'_{mn}}{a}r) \begin{Bmatrix} cos(m\phi) \\ -sin(m\phi) \end{Bmatrix} cos(\frac{p\pi}{d}z) \tag{C.13}$$

with resonant frequencies

$$(f)_{mnp} = \frac{c}{2\pi\sqrt{\mu_r \epsilon_r}} \sqrt{\left(\frac{x'_{mn}}{a}\right)^2 + \left(\frac{p\pi}{d}\right)^2}. \tag{C.14}$$

J_m, J'_m, x_{mn}, and x'_{mn} are the Bessel function of first kind for integer m, it's derivative, it's n'th root and the derivatives n'th root, respectively. The functions and the roots are well known and studied, and most programming languages such as Matlab, R and Python contains both functions and roots as packages.

For TE modes, it is trivial to note that all fields are zero if $p = 0$. If instead $m = 0$, then only E_ϕ, H_z and, H_r is non-zero if $cos(m\phi)$ is chosen instead of $sin(m\phi)$.

The different modes exist due to the boundary conditions having a endless number of solutions. Each different mode, given by the integers $m = 0, 1, 2, ...,\ \ n = 1, 2, 3, ...$ and, $p = 0, 1, 2, ...$, have a corresponding resonant frequency, and it's field distribution is unique. The different modes will lay the base for how measurement will be conducted and what information the data will provide. Some field distribution can be found in the next chapter.

C.1.1 Field distributions and coupling loop

Using Python's packages *numpy, plotly, scikit*, the following plots can be made:

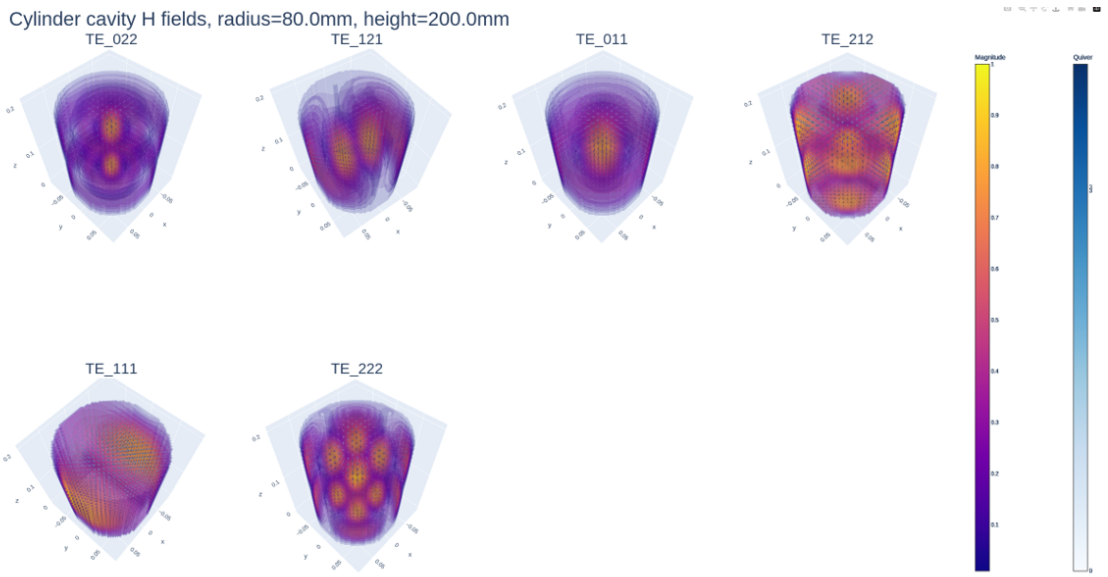

Figure C.2: TE modes 022, 121, 011, 212, 111, 222. Here normalised H fields are shown.

Since a coupling loop, or H-probe will be used (see chapter about Fluid bed dryer) it is the H-fields that provides an Eddy current in the loop, which then can be measured. Hence the loops should be located at the peaks of the magnetic field, where the area of the loop's normal should be tangential to the field direction.

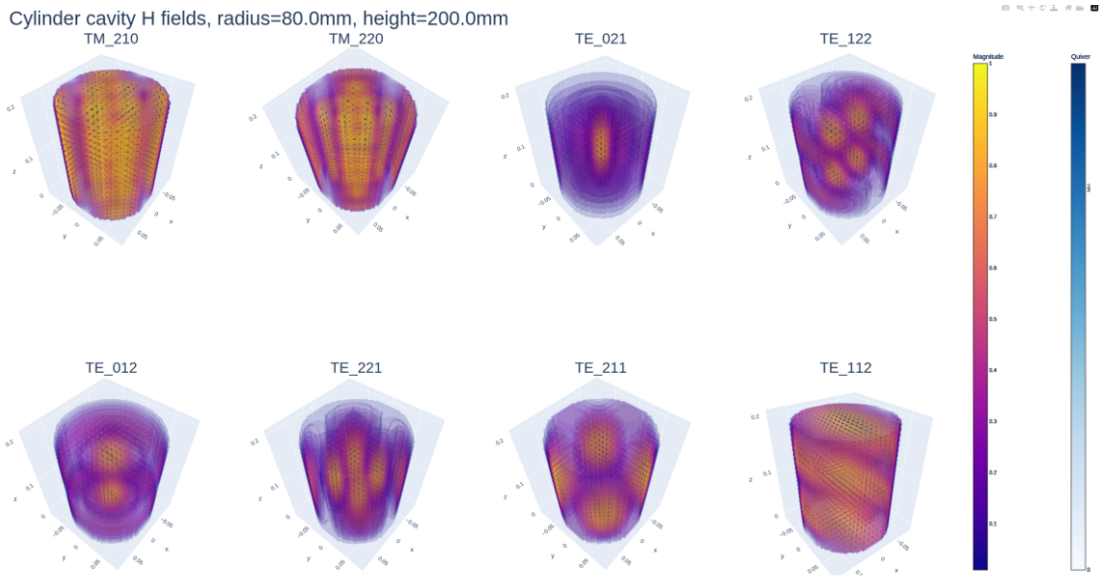

Figure C.3: TM 210, 220 and TE 021, 122, 012, 221, 211, 112. Here normalised H fields are shown.

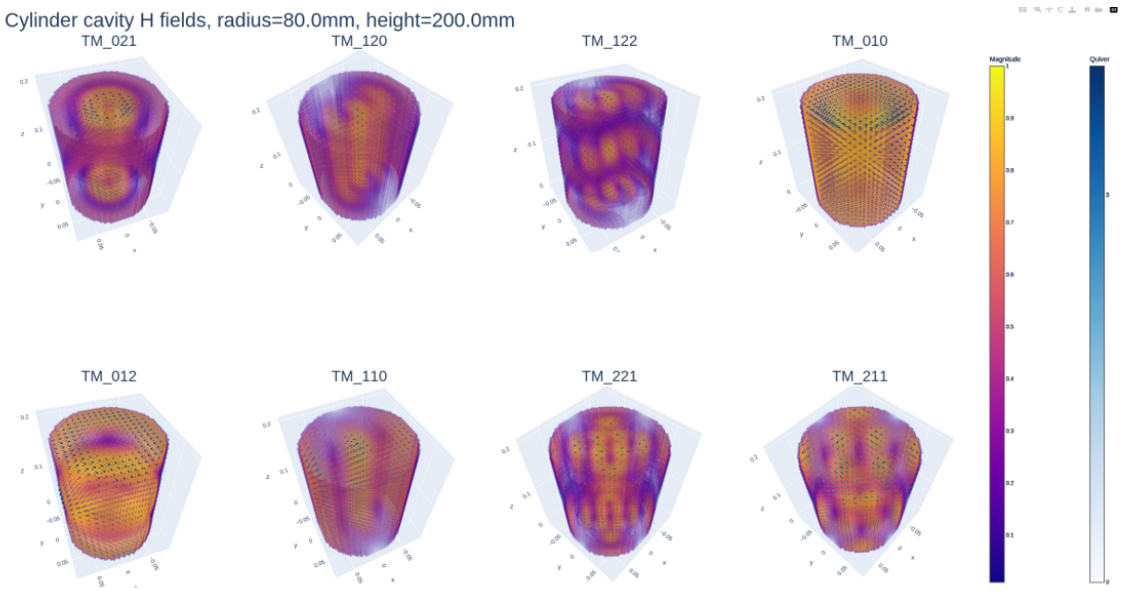

Figure C.4: TM modes 021, 120, 122, 010, 012, 110, 221, 211. Here normalised H fields are shown.

Additionally, the loops should be located at the cavity's wall for practical reasons. Following this reasoning as well as inspecting the field distributions (figure C.2, C.3, C.4, C.5), we can determine that for TE modes, $TE_{212}, TE_{111}, TE_{222}, TE_{221}, TE_{211}$ and TE_{112} are potential candidates providing strong fields close to the wall. For TM modes we have $TM_{210}, TM_{220}, TM_{010}, TM_{012}, TM_{110}, TM_{211}, TM_{011}, TM_{212}$ and, TM_{111}. The peaks are though located at different z and ϕ positions, implying that we cannot measure all of them. The modes that will provide the strongest Eddy current will depend on the location and size of the loops.

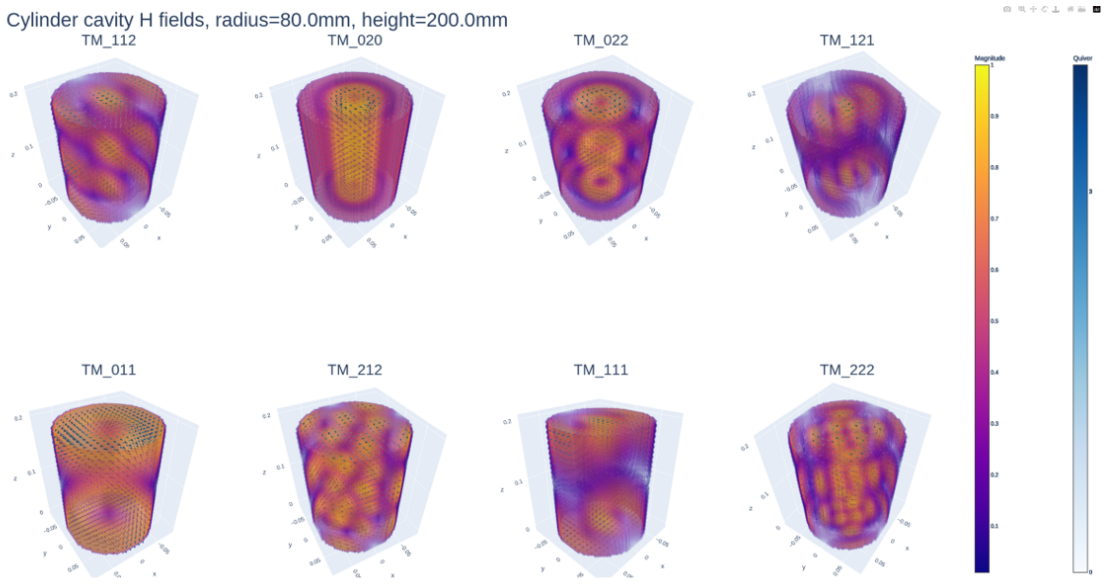

Figure C.5: TM modes 112, 020, 022, 121, 011, 212, 111, 222. Here normalised H fields are shown.

D

Implementation details

D.1 Devices

Devices used in the thesis (not all presented in the text) includes

- Keysight P5005A, Vector Network Analyser, frequency range between 0.1 - 26.5 GHz.
- National Instruments USRP N320, Software defined radio, frequency range between 3 MHz to 6 GHz, bandwidth up to 200 MHz.
- Thorlab motion controllers, LTS150, LTS300, and MLJ150.
- Fluid bed dryer, relative small sized.

For the VNA and Thorlab motion controllers two python wrappers/API was programmed using the python libraries pyVISA (VNA) and serial (Thorlab). Code will be/is published on github.

For the VNA a monitor GUI was developed for continuous, live, fast sampling, saving and viewing of said electronic system. This GUI is described further in D.3 and was used in case I and II.

D.2 Antennas and hardware

The current section will provide details of the antenna construction for the two cases. Justification for the antenna placements is provided in the simulation section, as well as size of antenna.

The antenna will be coupled to a VNA through SMA-contacts. To add stability the antennas are either soldered or welded onto the cavity walls. In the case of the of the fluid bed the antennas were placed at the top of the cavity to avoid as much direct contact to the particles as possible. Additionally, the antennas for the fluid bed were welded into the walls prior to the project, and for simplicity kept as is - except for straightening them as they were bent and damaged. In contrast, the cylinder for

the particle in flow project and its antennas were constructed and soldered during the project.

Case I:
The top antenna in the metal cylinder is placed 45 mm from the top, is oriented with its plane normal vertically (orthogonal to the z-axis), and have a size of ~ 25 mm. The lower antenna is located at around half the cylinder height, i.e. 97,5 mm with its plane normal oriented horizontally (tangent to the z-axis) and has a length of 60 mm.

Case II:
The top antenna in the metal cylinder is placed 20 mm from the top, is oriented with its plane normal vertically (orthogonal to the z-axis), and have a size of ~ 90 mm. The lower antenna is located at around half the cylinder height, i.e. 80 mm with its plane normal oriented horizontally (tangent to the z-axis) and has also a length of 90 mm.

D.3 Data Acquisition

For the purpose of understanding and later analyse the systems, a monitor software system were programmed to control the VNA hardware, as well as continuously monitor and store the acquired spectrums. The monitor programme was developed in python using the PyVISA API to communicate with the VNA, and standard python modules for visualisation and storing data. To allow continuous monitoring, the sampling, the GUI and storing of data was programmed to be parallel processes, using standard threading-queue practices. While sampling the GUI displays the L_1 norm of the current sample differentiated with a reference spectrum retrieved prior to the sampling, i.e. $L_1 = \sum |x - x_{ref}|$, which can give an initial understanding of the data. Data from the Case I process was manually added, while for the Case II process the fluid bed already have a acquisition software developed in Labview. In figure D.1 the monitor and pre-processing of the data is shown for the Case II process, while as for the Case I process the only change is in the left part.

To correlate the data from the fluid bed to the spectrums, both the monitor and the fluid bed programme stored time points when the data was acquired. The fluid bed data was then interpolated using the timestamps to match the samples from the VNA.

The sampling time for all four scatter parameters, with 40 000 sampling points/frequencies each (20 000 for amplitude and phase respectively), is 40 milliseconds. The sampling speed is optimised by using proper settings of the VNA, as well as only reading binary data and converting them as a post-processing step. As a final step before data analysis the scatter parameters are converted to its corresponding Euclidian form.

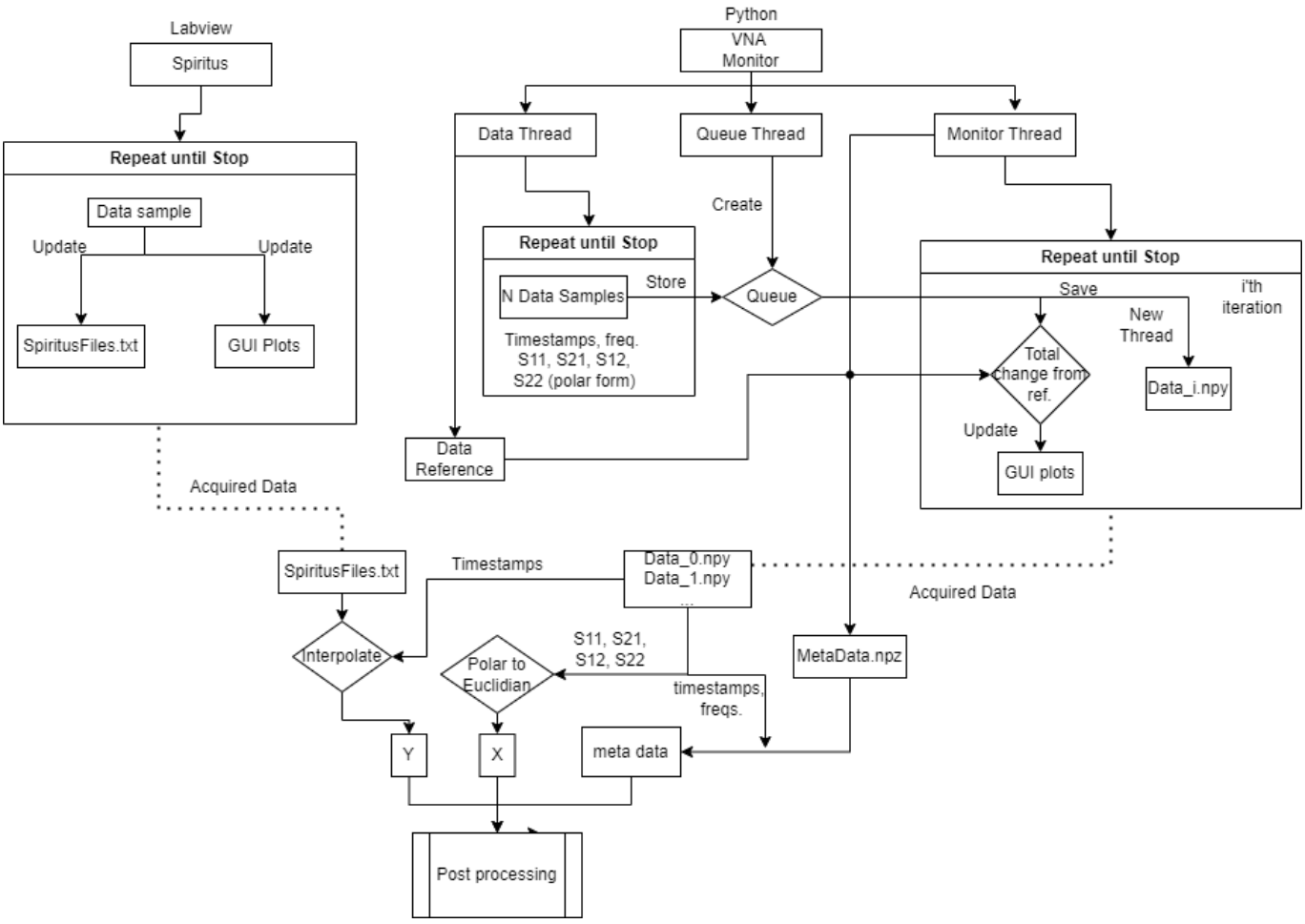

Figure D.1: The data acquiring procedure for the fluid bed project. Image created using the free online tool `https://app.diagrams.net/`.

E

Regression analysis

In both the OLS, PCR and PLS cases a covariance matrix is used. The covariance matrix, due to its properties of being square and symmetric, naturally finds eigensolutions by solving the optimising problem

$$R(M, w) = \frac{w^T M w}{w^T w} \tag{E.1}$$

$$s.t.\ ||w||^2 = w^T w = 1 \tag{E.2}$$

where M is a symmetric matrix, and w can be shown to be it's corresponding eigenvectors. The optimising problem is frequently used for establishing a theoretical basis for the PCA and PLS algorithms and variants. $R(M, w)$ is commonly called the Rayleigh quotient. As such we aim to find $w : Mw = \lambda w$ where λ is the corresponding eigenvalue, and for PCR we let $M = X^T X$ and for PLS we let $M = X^T Y Y^T X$.

E.1 Non-linear regression

While there are several different methods, we will consider two types of non-linear regressions; (a) the first is a simple extension of the linear methods discussed above, and (b) is by using neural networks. For brevity reasons, non will be extensively covered here but only briefly mentioned. In the non-linear cases we assume that the assumption of the form described in equation 2.16 doesn't hold, and we need more general solutions.

In the case of (a), we still assume the shape of X and Y and let a transformer map the matrices into a higher dimension to then perform the same algorithms as above. The most common way to describe this process is kernel regression. In such cases we let $\Phi_X = \Phi(X)$ and $\Phi_Y = \Phi(Y)$ be so-called *feature maps* of X respectively Y, and $K_{XX} = \Phi_X^T \Phi_X$, $K_{YY} = \Phi_Y^T \Phi_Y$ be their respectively kernels. In general we would consider the inner product $< ., . >$, which for vectors in L_2 is $(.)^T(.)$, but here we are satisfied with the current form and note that they are essentially the covariances if the features maps are also centred. For PCR, we can then simply exchange $X^T X$ to K_{XX}, and for PLS we note that if the goal is to find an eigendecomposition of

$$X^T Y Y^T X w = \lambda w$$

we can multiply each side with X, and note that $t = Xw$. We then have

$$XX^TYY^TXw = \lambda Xw$$
$$<=> XX^TYY^Tt = \lambda t$$

i.e. still keeping the same eigenvalues and thus we can utilise kernels as

$$K_{XX}K_{YY}t = \lambda_\Phi t. \tag{E.3}$$

A requirement is that the kernels are zero-mean (or centred), and they are positive semi-definite in the operating space (to assure symmetric properties). The downside of kernels is that they must be carefully chosen for the data to hold any value. Instead by considering (b) we use so-called neural networks instead. While the theory behind neural networks is to extensive for the scope of this project, we satisfy with saying that neural networks aim can be seen as a way to build an assumption model by updating a complex (not in the sense of imaginary) network of weights often using standard gradient descent methods. As such f can be determined, but as it consists of a complex network of weights it is in general difficult to interpret. There are to this point overflowing with research covering this topic, and the author refers to the internet for the interested.

The extension to the non-linear case is analogous to the real space, where we use a feature map to increase in dimensions, and use the kernel defined as above for both circular-symmetric and non-circular-symmetric data. The only thing to keep in mind is that the feature maps should be defined for complex spaces, and that they should satisfy positive semi-definite properties in the complex case, to assure Hermitian properties. For neural networks the *complexPytorch* library have been specially built (62).

E.2 Widely Linear Partial Least squares

We provide two versions on the widely linear PLS, where in the first the method used in (23) will be revised, and in the second we will consider the kernel version of PLS. As such, we first consider $\underline{X}^H\underline{YY}^H\underline{X}$ which can be rewritten as,

$$\begin{aligned}\underline{X}^H\underline{YY}^H\underline{X} &= (X_{Re}T_m^H)^HY_{Re}T_p^H(Y_{Re}T_p^H)^HX_{Re}T_m^H \\ &= T_mX_{Re}^TY_{Re}T_p^HT_pY_{Re}^TX_{Re}T_m^H \\ &= T_mX_{Re}^TY_{Re}Y_{Re}^TX_{Re}T_m^H. \end{aligned}\tag{E.4}$$

Thus, we first perform the EVD on $X_{Re}^TY_{Re}Y_{Re}^TX_{Re}$ to gain the weight vector W_{Re}, and transform back to the augmented form using $\underline{W} = \frac{1}{2}T_mV_{Re}T_m^H$. We note again that W is of the form

$$\underline{W} = \begin{bmatrix} W_1 & W_2^* \\ W_2 & W_1^* \end{bmatrix}.$$

We use the same widely linear transformation to retrieve T,

$$T = XW_1 + X^*W_2. \tag{E.5}$$

The approach here will be a little bit different compared to Circular-Symmetric version of PLS as noted by (23), and we seek the solutions of the widely linear form,

$$\begin{aligned} X &= TP_1^H + T^*P_2^H \\ Y &= TC_1^H + T^*C_2^H. \end{aligned} \tag{E.6}$$

We use the widely linear OLS approximation, eq. 3.12, to find $\underline{C}$ and $\underline{P}$ as

$$\begin{aligned} \underline{P} &= \begin{bmatrix} P_1 & P_2 \\ P_2^* & P_1^* \end{bmatrix} = ((\underline{T}^H\underline{T})^{-1}\underline{T}^H\underline{X})^H \\ \underline{C} &= \begin{bmatrix} C_1 & C_2 \\ C_2^* & C_1^* \end{bmatrix} = ((\underline{T}^H\underline{T})^{-1}\underline{T}^H\underline{Y})^H. \end{aligned}$$

Upon extraction of $C_1, C_2, P1$, and P_2 we truncate and estimate using E.6 to finally get

$$\begin{aligned} \tilde{X} &= \tilde{T}\tilde{P}_1^H + \tilde{T}^*\tilde{P}_2^H \\ \tilde{Y} &= \tilde{T}\tilde{C}_1^H + \tilde{T}^*\tilde{C}_2^H. \end{aligned} \tag{E.7}$$

To retrieve B_1 and B_2, we use the widely linear OLS estimation, eq. 3.12, on the approximations $\tilde{X}$ and $\tilde{Y}$. We quickly note here that the approximation in (23) looks inherently different. The reason for this lies in the nature of the approximations, where they use the minimum mean square error (MMSE) estimation, while of course we use the OLS approximation. Per definition, for large enough samples the OLS approximation tends towards the MMSE estimation in which the solutions converges. The OLS approximation is thought much easier implementable, which is the reason for choosing it over the MMSE.

F

Numerical Results

In this chapter we present both the approach, but also the results of simulating the different cases. Simulation can provide a foundation on how the system theoretically behaves in practice, and support subsequent theoretical methodology derivations. In our case we wish to simulation tools to describe electromagnetic models systems, especially microwave cavities. In some scenarios, just simulating how the EM waves and fields propagates would not be enough, if for instance we would also like to simulate how the EM waves effects the environment, or how a changing environment effects the fields. In these cases, multiphysics tools can be utilised to simulate both the EM fields but also other properties such particle movement or heating due to energy loss.

Typically used tools for EM simulations are for commercial; Ansys HFSS and Comsol multiphysics and for open-source; Elmer FEM multiphysics and FEniCS Multiphysics. Commercial softwares have been used extensively in literature, and are in general considered reliable simulation tools, but are costly and could possible limit research and collaboration in regards to software acquisition and redistributabilty. Open-source softwares could instead be used as they can be download to any computer at anytime, but the simulations may instead need to be validated against the commercial solutions as they have not been fully developed yet, with several functionalities being implemented and actively developed. Open-source softwares could also possibly be more difficult to use and require several softwares for modelling, meshing and post-processing additional to the simulation, and be coupled to other softwares for additional functionalities.

In the current thesis we will use the Open-source multiphysics software Elmer FEM (abbreviated as simply Elmer), which stands out since it both provides an interface both for command line and GUI and also provides parallel simulation extensions interfaces. Additionally, Elmer can also be coupled with other open-source tools such as openFOAM to add flow simulations(63). In practice, while Elmer offers meshing and post-processing to some extent, the typically workflow is to model, mesh and post-process outside of Elmer, and let Elmer handle the EM simulation. More specific, we use FreeCAD(64) to make the model, Salome(65) for meshing, Elmer(66) to simulate the EM waves and finally Paraview(67) for post-processing and viewing the results.

F.1 Elmer EM solvers

Elmer offers several electromagnetic modules, and can be used for different scenarios and formulations depending on the specific case. Especially four modules could be of interest in our case, the *VectorHelmholtz*, *MagnetoDynamics*, *StatCurrentSolve* and *EMWaveSolver* (68). Additionally, Elmer offers eigenvalue extensions for solving eigenvalue problems (69) for both the MagnetoDynamics and EMWaveSolver modules. Of the four modules, the VectorHelmholtz, MagnetoDynamics and EMWaveSOlver modules can be used to calculate EM fields, while the StatCurrentSolver can be used to simulate current inside a curcuit, coil or PCB. The StatCurrentSolve can then be utilised to calculate the current in the H-probe, and then use the solution (body force or initial condition fo H-probe) for excitation of waves from the probe into the cavity. A similar procedure was done in (70), but the excitation was used to calculate self- and mutual inductance of a PCB instead of excitation of waves into a cavity.

In the current report only two modules will be used, MagnetoDynamics (in combination of the eigenvalue extension) to calculate eigensolutions for the cavity, and VectorHelmholtz to calculate fields excited by a H-probe. The H-probe will be assumed to be a half-torus located at the wall for simplicity, with a pre-defined boundary condition (or body force). Attempts have been made to utilise the StatCurrentSolve, but either the simulation became extremely slow, or the fields strength as compared to the probes field strength visually disappeared. Below, a deeper explanation of the eigenvalue simulations and the probe excitation set-up is provided, with a slight discussion of pros and cons of the different solutions.

F.1.1 Eigensolutions to microwave cavities simulations

As discussed in section 2.2, Helmholtz's and thus Maxwell's equations (provided certain assumptions) can be viewed as an eigenproblem, with eigenvectors (H_m, E_m) and eigenvalues ω_m. The pros of solving the eigenvalue problem instead of excitation of the probe, is that we retrieve the resonant frequencies and the respective resonant fields inside the cavity, which we now will be the most sensitive to perturbations cause by the introduced material (e.g. particles). Thus we gain discrete values for the resonant frequencies and resonant fields, which we can use to develop our analysis methods later, including placement of probes but also how we expect the fields to change when the material is present. Eigenvalue solutions are also time efficient, and typically takes around 3-5 minutes, while solving using the probe takes sometimes up to half a day. The disadvantage of using the eigenvalue solver is that it is more of a theoretical solution, rather than realistic. Additionally it also not continuous, meaning that the simulation frequency can not be specified, and thus worse at simulating changes in changing environments.

Elmer provides an extension to normal modules to solve eigenvalue problems, and we aim to utilise the extension together with the *WhitneyAVHarmonicSolver* procedure of the MagnetoDynamics module. As such, while setting relevant boundaries (walss etc.) to zero, and adding the following lines to the solver section

```
Solver 1
  ...
  Procedure = "MagnetoDynamics" "WhitneyAVHArmonicSolver"
  ...
  Eigen Analysis = True
  Eigen System Values = 10 ! find 10 eigenvalues per simualtions
  Eigen System Shift = Real 30 ! The value 30 is changed to find the eigenvalues
  ...
End
```

An example of result for a cylinder is shown in figure F.1, next to the real solution found by analytically solving the equations. The results show good correlation between the Elmer simulated and the analytical solution, suggesting the Elmer's solution provides reliable fields. Several more fields for the cylinder have been simulated using the same code, except for altering the shift value, but is left out of the report.

F.1.2 Probe excitation's simulations

The other option, as briefly mentioned above, is to let a probe excite energy/waves into the system for a given frequency, and solve the EM waves using standard linear and non-linear FEM solver methods. In this case we use Elmers *VectorHelmholtz* procedure from the VectorHelmholtz module so find solutions of the fields. We approximate the H-probe with a torus shaped model, with its centre at the edge of the wall and all parts outside the cavity cut-off (using FreeCAD's boolean subtraction/-cut method) and with a slice diameter 2 mm, and ring radius of 25 mm. Henceforth the cut-off torus will be refered to as either half-torus, or H-probe. For simplicity, we will also let the torus by oriented in the x-y axis.

The advantage of using the H-probe model is the sligthly more realistic simulations for any chosen frequency, and also better integration with models that may not have eigensolutions, or other type of simulations when coupled with e.g. openFOAM. The sole disadvantage in the opinion of the author is the simulation time, which could take up to half a day, while the eigensolver for the same model takes minutes.

In order for the probe to excite energy into the cavity, the boundary of the half-torus cannot be set to zero, and should ultimately follow some kind of physical explanation. Using the assumption of the half-torus being in the x-y axis the following equations can be used to describe the current density (71; 72),

$$J_x = |J| \frac{y - y_0}{\sqrt{(y - y_0)^2 + (x - x_0)^2}}$$
$$J_y = |J| \frac{x - x_0}{\sqrt{(y - y_0)^2 + (x - x_0)^2}}$$
$$J_z = 0$$

where J is the magnitude of the current, x and y is the coordinates, and x_0 and y_0 is

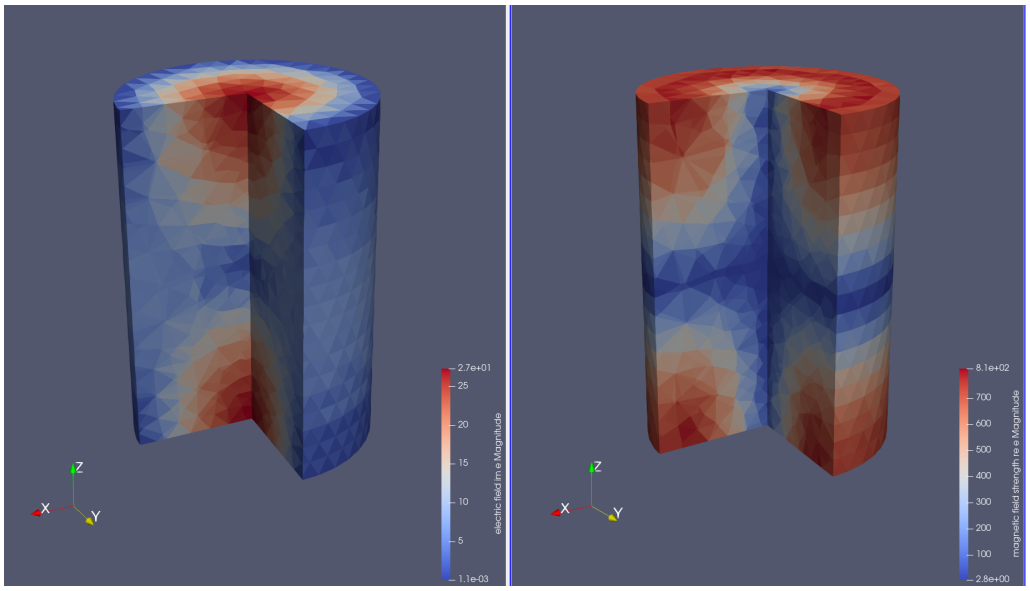

(a) Elmer's eigenvalues solution found using the eigenvalue solver in combination with WhitneyAVHarmonicSolver. To the left, the electic field (magnitude), to the right, the magnetic field. In this case TM_{011} was found, with $w_m \approx 2.1GHz$. Solution is visualised with the software Paraview.

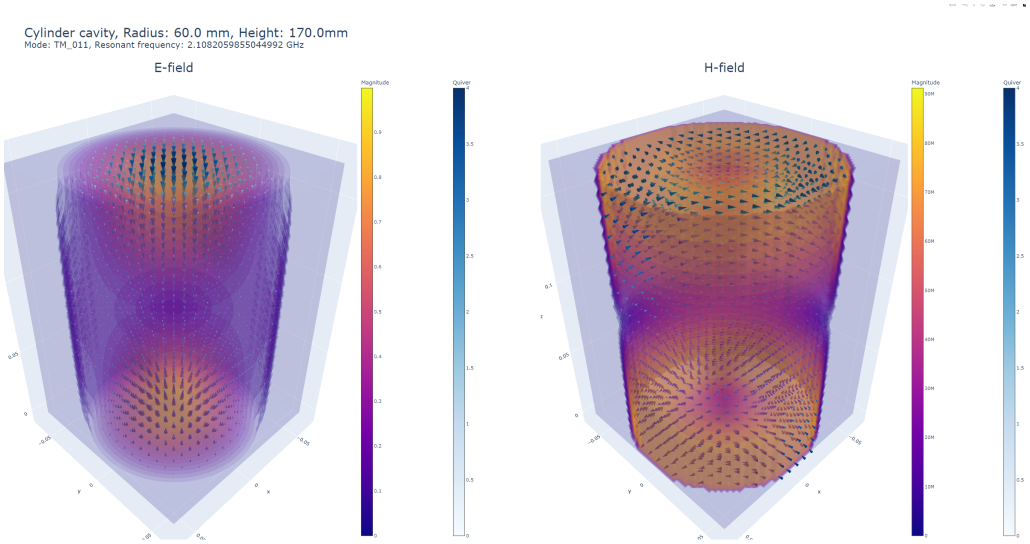

(b) Analytically derived fields for the TM_{011} mode.

Figure F.1: Microwave simulated cavity with a radius of 60 mm, height of 170 mm, (a) Elmer simulation results and (b) analytical results.

the center of the torus in the x-y axis. The devition of $1/r = 1/\sqrt{(y-y_0)^2 + (x-x_0)^2}$ is to keep 1 V for the whole half-torus. These can then be used in the VectorHelmholtz procedure either as *body force*, or *boundary conditions*. In subsequent simulations we will use the latter, and implementation in Elmer is in the form,

```
Boundary Condition 3
  Target Boundaries(1) = 7
```

```
  Name = "Boundary Port Dirichlet"
  ! no imaginary contribution
  E im {f} = Real 0
  E im {e} = Real 0
  ! J_z = 0
  E re {e} 3 = Real 0
  E re {f} 3 = Real 0

  E re {f} 1 = Variable Coordinate
Real MATC "(tx(1) - CableAxisY) /
    ((tx(0) - CableAxisX)^2+(tx(1) - CableAxisY)^2)/(2*pi)"
  E re {f} 2 = Variable Coordinate
Real MATC "-(tx(0) - CableAxisX) /
    ((tx(0) - CableAxisX)^2+(tx(1) - CableAxisY)^2)/(2*pi)"

  E re {e} 1 = Variable Coordinate
Real MATC "(tx(1) - CableAxisY) /
    ((tx(0) - CableAxisX)^2+(tx(1) - CableAxisY)^2)/(2*pi)"
  E re {e} 2 = Variable Coordinate
Real MATC "-(tx(0) - CableAxisX) /
    ((tx(0) - CableAxisX)^2+(tx(1) - CableAxisY)^2)/(2*pi)"
End
```

Note here that for shortening of the report, some simplification was done here as compared to the actual used code. A full example code can found in the appendix F.3.2. In addition to the boundary condition, we set

```
$ fs = f0 f1 ... f9
Simulation
...
  Simulation Type = Scanning
  Timestep intervals = 9
...
End
```

and

```
Equation 1
...
Angular Frequency = Variable time; Real MATC "2 * pi * fs(tx - 1)"
End
```

to sweep over the specified frequencies $f0, f1, ..., f9$. Using the sweeping technique, an initial guess what the resonant frequency is, then sweeping over a range of values to find it more specifically can be done.

In figure F.2 an example of a simulation is shown, where the Elmer results deviates

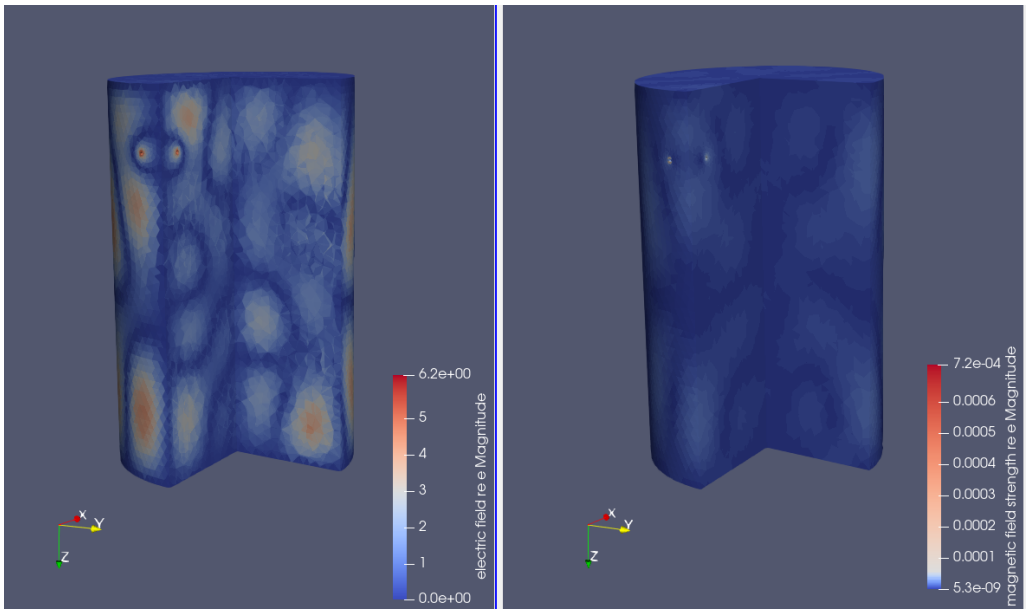

(a) Excitation from a H-probe (half-torus) into a cavity at 2.45GHz. The probe can be seen in the top left of the cylinder, and is cut into one half.

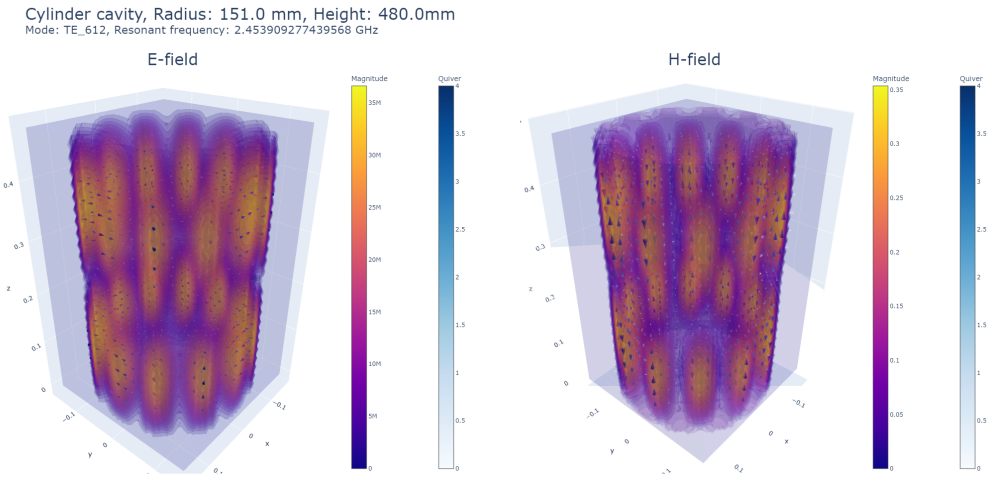

(b) Analytical solution of cylinder fields for the TM_{612} mode.

Figure F.2: Microwave simulated cavity with a radius of 141 mm, height of 480 mm, (a) Elmer simulation results with probe and (b) analytical results without probe.

from the analytical solution (with no probe). The deviations are intentional for illustration purposes, and results which resembles the corresponding eigensolution will be displayed in the result section. The deviations are mainly caused by three factors; 1) the frequency was not set close enough to the actual eigenvalue frequency, 2) the probe in this case was too thick and had a too large radius, and 3) the due to the mode being rather high, several eigensolutions can be found within the close region which results in several solutions are displayed simultaneously (to some degree). The shift in frequency produced the largest deviation, and adding up

to three decimals produces a better simulation. Although, due to the addition of the probe in the cavity the fields is subjected to a perturbation, as explained in the perturbation section 2.2.1, and found the eigensolution with frequency set to 2.448GHz.

Figure F.2a) additionally depicts another issue using the probe simulation, which is more of a technical issue than a simulation issue, that due to fields close by or on the boundary of the probe is much higher than the rest of the cavity. This is particularly evident in the magnetic fields plot (right figure), where the fields are barely visible without changing the color gradient scaling (see colour bar next to cylinder).

F.2 Results: Fluid bed dryer

In this section we will display simulation results for the fluid bed dryer. The dimensions of the model is based on Johan Nohlert's dissertation (5) (publicly available online), as Nohlert conducted simulations using Comsol with a fluid bed of the same dimensions as the one used in the current project was made, although Nohlert only simulated eigensolutions. A comparison between the simulation results will be made in the discussion section below. In contrast to Nohlert, the magnetic fields will additionally be displayed as they will provide important information as to where the probes should be located.

F.2.1 Eigensolutions

In the following section we will present simulations results using the eigenvalue approach discussed in section F.1.1. As presented previously, there are infinitely many eigensolutions, and thus only a handfull (a total of eight) will be shown here. The first four solutions found, displayed in figure F.3, is the same first four found by Nohlert. In figure F.4 four additional solutions which were not presented in Nohlerts dissertation are presented. The corresponding eigen mode (with numbers), are there as a reference as how they visually look in comparison to the eigen kodes of a cylinder, and in practice doesn't mean anything.

F.2.2 Probe simulations

In this section only two solutions will be presented, which can be seen in figure F.5. To find the resonant modes, the frequency was swept around an initial guess of the assumed resonant frequency. For figure F.5a), the initial guess was retrieved form the eigensolution above, and for figure F.5b) the guess was made based on the resonant frequency Nohlert simulated in his dissertation. For the electric fields, the solutions clearly resembles the corresponding eigensolution, similar for the magnetic field of figure F.5b), but less so for the magnetic field of figure F.5a).

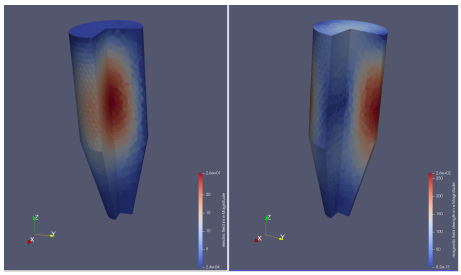

(a) Mode TE111 with eigenfrequency ∼0.71GHz, found using shift 20.

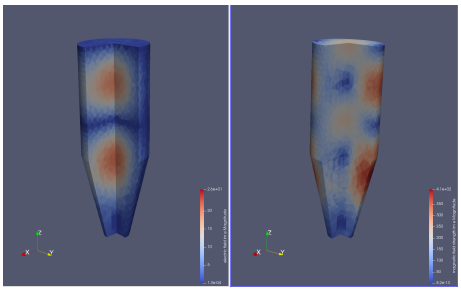

(b) Mode TE112 with eigenfrequency ∼0.90GHz, found using shift 30.

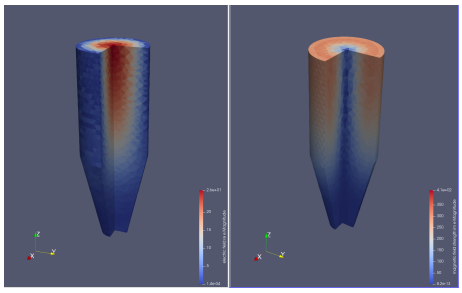

(c) Mode TM010 with eigenfrequency ∼0.93GHz, found using shift 50.

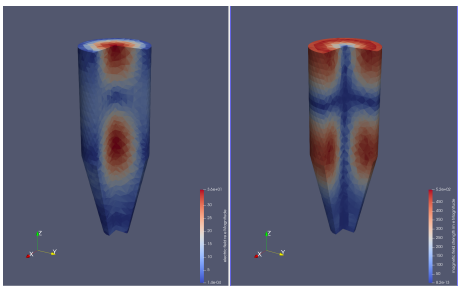

(d) Mode TM011 with eigenfrequency ∼1.1GHz, found using shift 90.

Figure F.3: First four eigensolutions for the fluid bed dryer found by Elmer. Also the corresponding first four in Nohlert's dissertation(5).

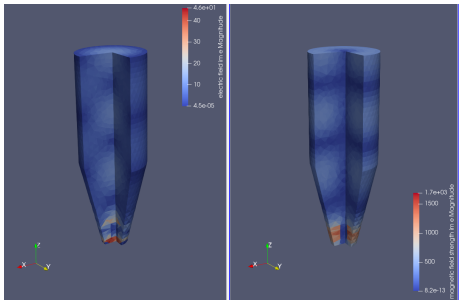

(a) Shift 300.

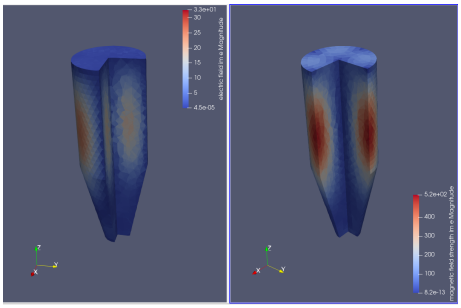

(b) Shift 500.

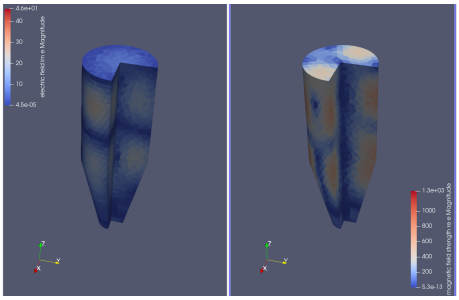

(c) Shift 700.

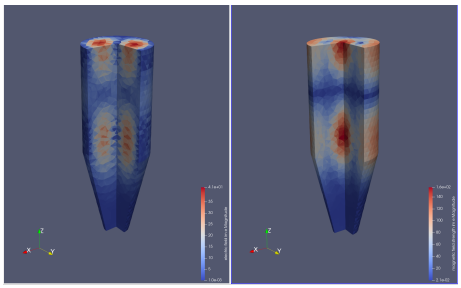

(d) Shift 1000.

Figure F.4: Additional eigensolutions.

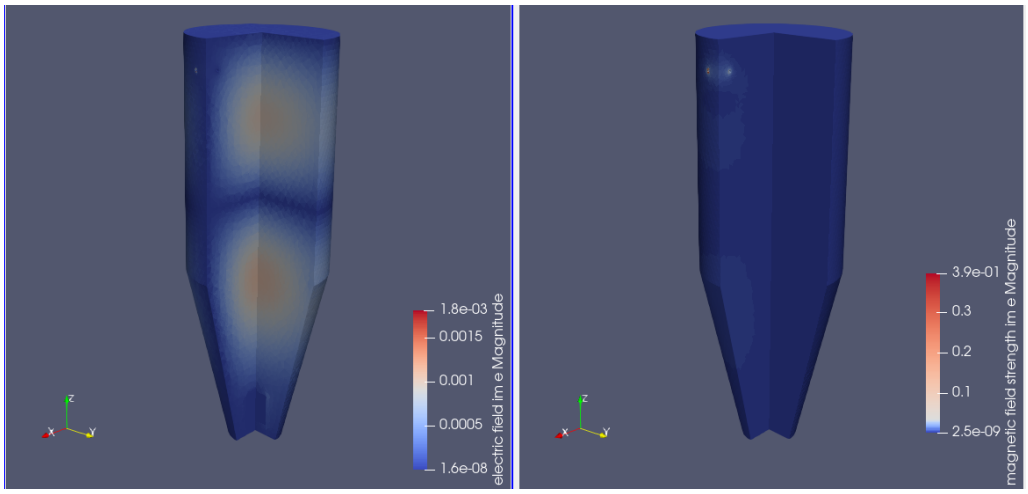

(a) $f \approx$0.9GHz.

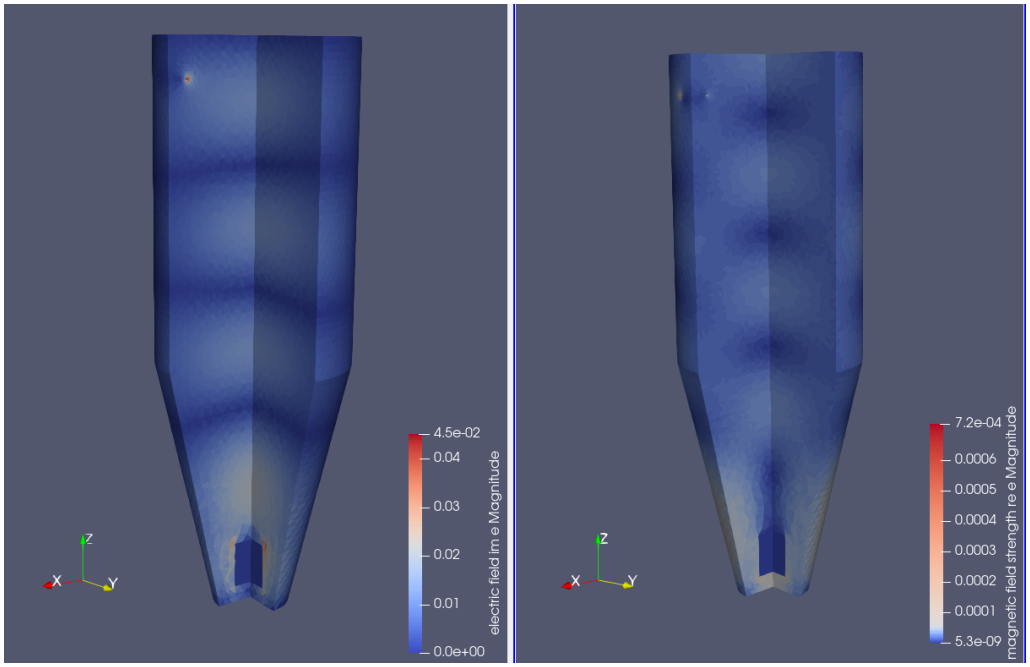

(b) $f \approx$1.2GHz.

Figure F.5: Excitation from a H-probe (half-torus) into the fluid bed cavity. The probe can be seen in the top left of the cylinder, and is cut into one half.

F.3 Elmer sif code

In this section example Elmer sif code is provided, for the two cases mentioned in the report, eigensolver and H-probe.

F.3.1 Eigensolver sif code

F.3.2 H-probe sif code

```
! Model definition params

! General params
$ mu0=4*pi*1e-7
$ epsilon0 = 8.854e-12
$ c0 = 1/sqrt(epsilon0*mu0)

! Simulation specific
! one frequency
$ fres = 1.2e9
$ omega = 2*pi*fres
! sweep frequency
$ fs = 1.0e9 1.05e9 1.1e9 1.15e9 1.2e9 1.25e9 1.3e9 1.35e9 1.4e9


! H-probe
$ FeedingCoilRi = 0.002
$ FeedingWireR = 0.03
$ CableAxisX = 0 ! center of the H-probe
$ CableAxisY = 0 ! center of the H-probe

! Walls
! Constant for Leontovich boundary condition
$ l=767340


Header
  CHECK KEYWORDS Warn
  Mesh DB "." "."
  Include Path ""
  Results Directory "Freq1.2GHzSweep"
End

Simulation
  Max Output Level = 5

  Coordinate System = Cartesian
  Coordinate Mapping(3) = 1 2 3
  Coordinate Scaling(3) = 0.001 0.001 0.001

  ! Simulation Type = Steady state
  Simulation Type = Scanning
  Timestep intervals = 9

  Steady State Max Iterations = 1
```

```
  Output Intervals = 1

  Timestepping Method = BDF
  BDF Order = 1

  Solver Input File = case.sif
  Post File = case.vtu
  Output File = "caseres.result"

! Save only the internal E field in Hcurl space
  Output Variable 1 = E re
  Output Variable 2 = E im
  Output Global Variables = True
  Binary Output = False

End

Constants
  Gravity(4) = 0 -1 0 9.82
  Stefan Boltzmann = 5.67e-08
  Permittivity of Vacuum = 8.8542e-12
  Boltzmann Constant = 1.3807e-23
  Unit Charge = 1.602e-19
End

Body 1
  Target Bodies(1) = 1
  Name = "Body Property 1"
  Equation = 1
  Material = 1
End


Solver 3
  Equation = Result Output
  Procedure = "ResultOutputSolve" "ResultOutputSolver"
  Output File Name = case
  Binary Output = False
  Output Format = Vtu
  ! Exec Solver = Always ! sibngle freq
  Exec Solver = After Timestep ! Sweep freq
End

Solver 1
  Equation = Vector Helmholtz Equation
! This is to store the E field in Hcurl space, required for restart.
```

```
  Variable Output = Logical True
  Variable = E[E re:1 E im:1]
  Use Piola Transform = True
  Linear System Preconditioning Damp Coefficient im = 1.0
  Procedure = "VectorHelmholtz" "VectorHelmholtzSolver"
  Exec Solver = Always

  Stabilize = True
  Bubbles = False
  Lumped Mass Matrix = False
  Optimize Bandwidth = True
  Steady State Convergence Tolerance = 1.0e-9

  Nonlinear System Convergence Tolerance = 1.0e-9
  Nonlinear System Max Iterations = 20
  Nonlinear System Newton After Iterations = 3
  Nonlinear System Newton After Tolerance = 1.0e-3
  Nonlinear System Relaxation Factor = 1.0
  Nonlinear System Convergence Measure = Solution

  Linear System Solver = Iterative
  Linear System Iterative Method = BiCGStabl
  Linear System Max Iterations = 5000
  Linear System Convergence Tolerance = 1.0e-9
  BiCGstabl polynomial degree = 10
  Linear System Preconditioning = vanka
  Linear System ILUT Tolerance = 1.0e-3
  Linear System Abort Not Converged = False
  Linear System Residual Output = 10
  Linear System Precondition Recompute = 1
End

Solver 2
  Equation = Vector Helmholtz Post Process
  Procedure = "VectorHelmholtz" "VectorHelmholtzCalcFields"

  Calculate Energy Functional = True
  Field Variable = E
  Calculate Magnetic Flux Density = True
  Calculate Electric Field = True
  Calculate Poynting Vector = True
  Calculate Div of Poynting Vector = True
  Calculate Magnetic Field Strength = True

  Exec Solver = Always
  Stabilize = True
```

```
  Bubbles = False
  Lumped Mass Matrix = False
  Optimize Bandwidth = True
  Steady State Convergence Tolerance = 1.0e-8

  Nonlinear System Convergence Tolerance = 1.0e-8
  Nonlinear System Max Iterations = 50
  Nonlinear System Newton After Iterations = 3
  Nonlinear System Newton After Tolerance = 1.0e-3
  Nonlinear System Relaxation Factor = 1

  Linear System Solver = Iterative
  Linear System Iterative Method = BiCGStabl
  Linear System Max Iterations = 500
  Linear System Convergence Tolerance = 1.0e-10
  BiCGstabl polynomial degree = 8
  Linear System Preconditioning = vanka
  Linear System ILUT Tolerance = 1.0e-3
  Linear System Abort Not Converged = False
  Linear System Residual Output = 10
  Linear System Precondition Recompute = 1
End

Equation 1
  Name = "Equation 1"
  ! Angular Frequency = $ omega
  Angular Frequency = Variable time; Real MATC "2 * pi * fs(tx - 1)"
  Active Solvers(3) = 3 1 2
End


Material 1
  Name = "Air"
  Relative Permittivity = Real 1
End


Boundary Condition 2
  Target Boundaries(7) = 1 2 3 4 5 6 8
  Name = "Walls"
  ! Leontovich impedance boundary
  Electric Robin Coefficient = Real $ -l
  Electric Robin Coefficient im = Real $ l
End

Boundary Condition 3
```

```
  Target Boundaries(1) = 7
  Name = "Boundary Port Dirichlet"
  E im {f} = Real 0
  E im {e} = Real 0
  E re {e} 3 = Real 0
  E re {f} 3 = Real 0

  E re {f} 1 = Variable Coordinate
Real MATC "(tx(1) - CableAxisY)/
((tx(0) - CableAxisX)^2+(tx(1) - CableAxisY)^2)/(2*pi)"
  E re {f} 2 = Variable Coordinate
Real MATC "-(tx(0) - CableAxisX)/
((tx(0) - CableAxisX)^2+(tx(1) - CableAxisY)^2)/(2*pi)"

  E re {e} 1 = Variable Coordinate
Real MATC "(tx(1) - CableAxisY)/
((tx(0) - CableAxisX)^2+(tx(1) - CableAxisY)^2)/(2*pi)"
  E re {e} 2 = Variable Coordinate
Real MATC "-(tx(0) - CableAxisX)/
((tx(0) - CableAxisX)^2+(tx(1) - CableAxisY)^2)/(2*pi)"

End
```

DEPARTMENT OF SOME SUBJECT OR TECHNOLOGY
CHALMERS UNIVERSITY OF TECHNOLOGY
Gothenburg, Sweden
www.chalmers.se

CHALMERS
UNIVERSITY OF TECHNOLOGY